Estimation of Planetary Surface Ages Using Image Based Automatic Crater Detection Algorithms

Von der Fakultät

Elektrotechnik und Informationstechnik

der Technischen Universität Dortmund

genehmigte

Dissertation

zur Erlangung des akademischen Grades
Doktor der Ingenieurwissenschaften

eingereicht von

Atheer Luay Salih Al-Tameemi

Dortmund, 2018

Tag der mündlichen Prüfung:	27.09.2018
Hauptreferent:	Prof. Dr. rer. nat. habil. Christian Wöhler
Korreferent:	Prof. Dr.-Ing. Franz Kummert

Arbeitsgebiet Bildsignalverarbeitung Technische Universität Dortmund

ABSTRACT

A fully automatic system of crater detection, fusion and age estimation is built and constructed to result in reliable results in comparison with manually long time manually process from experts and professionals. A new idea of an extension of crater detection algorithms (CDA) is the Age Estimation that relied basically on Crater frequency-size distribution (CSFD). The age estimation process for surfaces depends basically on the numbers of the craters detected on the Moon surface and the total area of that surface.

It is examined how well a template matching method is suitable for determining the age of different lunar areas. Six artificially lit crater models are used to count the craters in the investigated areas using cross-correlation. A threshold value for the automatic crater detection algorithm has been calculated for each dataset in order to obtain the best reliable results followed by a fusion automatic process for duplicated detections. A new implementation of this approach is provided for estimating the surface age with the possibility of flexible threshold values needed for calibration and evaluation process. With these two above-mentioned automatic steps, this will result in a time reduction and reasonable crater detection and so far precise age values. An automatic age mapping process has been applied to use the optimal threshold value in larger homogenous areas for more efficiency and behavior study.

For the purpose of testing accuracy and efficiency, a dataset from lunar nearside regions has been examined to find out if there is an ideal threshold value for the crater detection process so that the smallest possible errors in the surface ages - derived from manually detected craters – are found in comparison to values from the literature. For this purpose, the optimal threshold value is calculated in five areas of Mare Cognitum on the Moon and then use to determine the age of five other areas in Oceanus Procellarum. By subsequently comparing the calculated ages with those from the literature, the accuracy of the method is examined.

An image-based CDA has been implemented on a different dataset of craters, the first group of the dataset is the LU60645GT catalogue that includes a large number of crater candidates with diameters between 0.7 km and 2.5 km and located in the large craters

Alphonsus and Ptolemaeus. The second dataset is a different region on the Moon near the crater Hell Q that includes a limited number of small craters with very small diameters between 3 m and 70 m, while the third group of data contains a list of medium-sized craters (128 m-1000 m) on the morphologically homogeneous floor of the lunar crater Tsiolkovsky.

In an advanced step, an automatic method of detection for secondary crater candidates on the lunar surface has been proposed. To assess the accuracy of the developed method, automatic crater counts were performed for the flat floor of the lunar farside crater Tsiolkovsky by applying the Voronoi tesselation based Secondary Candidate Detection (SCD) to the results of the template matching based crater detector. For a small are on the crater floor, the obtained age of 3.21 Ga is consistent with the age of 3.19 Ga determined by Pasckert et al. (2015). In the next step, the age estimation was expanded to the complete crater floor, resulting in a map of the surface age which is at least partially corrected for the influence of secondary craters.

Acknowledgments

I'm sincerely grateful to my supervisor, Prof. Dr. Christian Wöhler for his unlimited positive support. I would like to convey my deepest gratitude and appreciation for all his valuable advice, guidance, learning opportunities, and trust that he provided me during this dissertation. His extremely understanding and support has made the project progress smoothly and made me be more precise in my work.

I would like also to express my great thanks to Prof. Dr. Harald Hiesinger from the University of Münster for his valuable support and his scientific comments. He was always following my work and a very good source of trusted data for analysis and comparison. I would like to give my best regards and acknowledgments to my colleague Dr. Arne Grumpe who helped me with his invaluable knowledge in this study. I would like to express my great thanks, for Andrii Lompart, Philipp Schulte, and Maximilian Mühlbauer and all my other colleagues, who I enjoyed working with them and with their discussions. I am fortunate to have such a friendly group who make my life here so excellent. I would like to thank the technical university of Dortmund for providing me with a chance of working there which helped me a lot to fund my studying period.

Finally, I would like to express my thanks and gratitude to my parents and my family, especially my wife and son, for their love, understanding and strong support and encouragement along the way. Great thanks to my baby Hamza, my source of inspiration.

To my family

To my wife, son

To my friends

List of Related Publications

This thesis is based on some of the following publications of the author. The publications are listed in descending chronological order.

Peer-reviewed journal articles and book chapters

(Salih et al., 2016b) Salih L. Atheer, A. Grumpe, C. Wöhler, and H. Hiesinger. ‘Construction of an Age Map of the Region Around the Young Lunar Crater Hell Q’, International Journal of Simulation Systems, Science, and Technology, vol. 17, no. 33, 2016. (Proc. 8th IEEE International Conference on Computational Intelligence, Communication Systems, and Networks, Kuala Lumpur, Malaysia, 25 - 27 July 2016).

(Salih et al., 2018) Salih L. Atheer, A. Lompart, P. Schulte, M. Mühlbauer, A. Grumpe, C. Wöhler, and H. Hiesinger. ‘Automatic Mapping of Planetary Surface Age’. In: B. Wu, K. Di, J. Oberst, I. Karachevtseva (eds.), Planetary Remote Sensing and Mapping, CRC Press, 2018.

Peer-reviewed conference contributions

(Salih et al., 2017b) Salih, Atheer L., P. Schulte, A. Grumpe, C. Wöhler, and H. Hiesinger. "Automatic crater detection and age estimation for mare regions on the lunar surface." In Signal Processing Conference (EUSIPCO), IEEE 25th European, pp. 518-522. ISBN 2076-1465. Doi: 10.23919/EUSIPCO.2017.8081261. 2017.

(Salih et al., 2017a) Salih, Atheer L., A. Lompart, A. Grumpe, C. Wöhler, and H. Hiesinger. "Automatic Detection Of Secondary Craters And Mapping Of Planetary Surface Age Based On Lunar Orbital Images." ISPRS International Archives of the Photogrammetry, Remote Sensing & Spatial Information Sciences 42 (2017), Volume XLII-3/W1, pp. 125-132. ISBN 2194-9034. Doi: 10.5194/isprs-archives-XLII-3-W1-125-2017.

(Salih et al., 2016a) Salih, Atheer L., M. Mühlbauer, A. Grumpe, J. H. Pasckert, C. Wöhler, and H. Hiesinger. "Mapping of Planetary Surface Age Based on Crater Statistics Obtained by an Automatic Detection Algorithm." ISPRS International Archives of the Photogrammetry, Remote Sensing and Spatial Information Sciences (2016): Volume XLI-B4, pp. 479-486. ISBN 2194-9034. Doi: 10.5194/isprs-archives-XLI-B4-479-2016.

Conference abstracts

Salih L. Atheer, P. Schulte, A. Grumpe, C. Wöhler and H. Hiesinger "Automatic Determination Of Lunar Surface Ages In Mare Cognitum And Oceanus Procellarum". The Fifth European Lunar Symposium, Münster, Germany, May 2-3, 2017.

Salih, A. L., M. Mühlbauer, A. Grumpe, J. H. Pasckert, C. Wöhler, and H. Hiesinger. "Automatic Age Map Construction for the Floor of Lunar Crater Tsiolkovsky." In Lunar and Planetary Science Conference, vol. 47, p. 1526. Id: 2016LPI....47.1526S. 2016.

(Salih et al., 2014) Salih, Atheer L., A. Boukercha, A. Grumpe, C. Wöhler, and H. Hiesinger. "Automatic Crater Detection and Implications for Surface Age Estimation." In European Planetary Science Congress 2014, EPSC Abstracts, Vol. 9, id. EPSC2014-602. 2014.

(Boukercha et al., 2014) Boukercha, A., A. Al-Tameemi, A. Grumpe, and C. Wöhler. "Automatic Crater Recognition Using Machine Learning with Different Features and Their Combination." In Lunar and Planetary Science Conference, vol. 45, p. 2842. Id: 2014LPI....45.2842B. 2014.

Table of Contents

Contents

Chapter 1

Introduction

1.1 Overview

Regularly, the lunar acquired data volume is increasing extensively with every new space mission for lunar or any other planetary object by adding new datasets of images with different degrees of resolution or different angles of illumination. Consequently, the manual extraction for all important information manually is sometimes not any more reliable and logical process due to the high difference in among the experts and professionals in craters analysis community (Robbins et al., 2014). Impact craters considered as the most common repeated feature on relatively all the planetary surfaces and the basic element in the geological history. Therefore, it is really a competitive challenge among many research groups to create reliable and precise crater detection algorithm (CDA). In addition to the challenge achievement difficulties, it is very important to know how to satisfy the scientific community with the (CDA) robustness and the recognition precision.

Choosing the experimental dataset from this huge pile of sets affects the building process and architecture for the CDAs (Salamunićcar and Loncaric, 2012). In general, the CDAs are basically classified according to the type of data they utilize in their analysis work. They use optical images data, topographic data or any other radar images. Most of the available current CDAs use optical images as mostly all the available data from this type. At the same time, there are a lot of CDAs using topography data due to the easier detection process and the possibility of extraction more craters' features automatically is higher than the other types.

One of the most important challenges to the CDAs is to process mostly all the global datasets with the highest percentage of efficiency and precision with respect to faster runtime and less memory consumption. Actually, many CDAs confirmed the capability of processing global topographic or optical image. There will be more analyzed data obtained with more detailed information with this type of CDAs.

1.2 Motivation

Lunar images and other planetary objects images data require a huge effort and time to extend the useful knowledge in studying area. The experts used to extract the information embedded in images and classifying them manually only through visual inspection. The image dataset interpretation process is usually a high time-consuming. And for the high-cost reasons, it is not possible to apply classification and systematic processing on large datasets volumes. From this point of view, the need to establish new techniques and methods to recognize the craters features automatically and classify them with an automated pattern recognition process instead of the manual interpretation activity. This urgent need for the automatic recognition and classification systems will become more important for the soon future with the evolution of new satellites (Di Stadio et al., 2002).

The analysis and recovery processes of the data are still up today depending on some special parameters like time, location, and sensor type despite the high number of computational parameters. The current and new automated systems need to develop a set of automated pattern recognition algorithms and techniques that extract the required features from remote sensing images data. The most important and simple feature that exists on Earth, Moon and some other planetary objects is the “crater”. The recognition and classification of impact craters can lead to more deep knowledge of the earth and other planetary objects geology (Di Stadio et al., 2002). The main application that based on the number of craters extracted from detailed images helps in a direct way in recording the history of the solar system by applying age estimation algorithms. Another application is to use the detected craters as landmarks for autonomous landing on asteroids. One of the most valuable cases of automatic recognition procedures is the detection of impact craters on Earth (i.e. in the uncovered regions) or any other planetary surface due to the high simplicity of the detection and recognition form which make the development of an automatic process easier.

In this study, an automatic crater detection algorithm is applied to various areas of the lunar surface, relying on images across a broad range of spatial resolution. The inferred crater count data are used for estimating the age of the surface based on the crater size-fequency distribution (CSFD). The basic approach is to calibrate the detection

sensitivity of the automatic algorithm with respect to manual crater count from the literature, and then to expand the age estimation to large areas for which manual crater counts are not feasible or would require tremendous efforts. Another important aspect of this work is the introduction of a method for the automatic distinction between primary and secondary craters, since the latter may affect the crater statistics used for estimating the surface age.

1.3 Impact Craters

The impact craters are geologic objects founded as a result of a large meteoroid, asteroid or comet collision to the surface of a planetary solid object (Di Stadio et al., 2002). The process that records the surfaces of the planetary bodies and registers their features for over (4.5 Ga) of the solar system is called Impact craterization. By this period of time, the Earth has been collided numerous times by comets, asteroids, and meteorites. There are some several studies applied by planetary missions presented several planetary objects contain less amount of impact craters densities such as the case for Venus and icy satellites, i.e. satellite of Saturn (Enceladus) or satellite of Uranus (Miranda) (Di Stadio et al., 2002). It is very clear now that impact craters and their effective role were the dominant geological factor in the growth process of the planetary bodies of the Solar System as all planetary surfaces are cratered from the impact of interplanetary objects.

The most studied features on Moon and Mars are the impact craters that provide a very effective wealth of information, which helps in a more detailed analysis of craters distribution per certain area. Building the basis for geological stratigraphy of the Moon and Mars depends on the statistics of crater sizes, which give us a great example of how the impact craters are a very important feature. The deep knowledge of craters morphologies encourages extended studies of a number of new approaches in Martian geomorphologies such as the geologic material regional variation, the nature of degradation processes and the subsurface volatiles distribution.

During the last five decades, the search space programs have extended the view of planetary objects studied from “astronomical” to very important “geological purposes (Di Stadio et al., 2002). This new approach of knowledge produced new ideas and

approaches on the space nature and, the effect of impact craters. The impacts happened on the planets have morphological effects and are spread worldwide but they are not clearly visible as it there on the Moon. The Moon surface, where there are no oceans to cover the original impact areas or there are no erosion and volcanism movements, is an excellent example of impact craters recording and their valuable effect. The Moon surface provides a great evidence for the importance of the terrestrial impact craters record, which shows that these craters are simple, represent a small portion of large carter population.

1.4 Craters

Craters exist in different shapes on the Lunar, mars or any other planetary objects. It is possible to recognize the craters due to their interior morphologies as they (central peaks, peak rings, central pits or wall terraces) and their ejecta structure (Salamunićcar et al., 2011). Logically, different planetary bodies have a different geological history.

The manual detection process time consumption of all craters is proportionally increasing with each new planetary mission that formed a huge volume of data. The spiritual key of motivation to work on CDAs is the craters, which considered as the main important feature for planetary surfaces in general. From this point, the necessity to built an automatic system for crater detection become a very challenging task that can provide robust results and analysis for data. But, still, scientists from several groups all over the world are trying to find the right procedure to for building the automatic crater detection system in a way that is acceptable and reliable for the majority of the scientific community (Salamunićcar and Lončarić, 2012).

Designing an algorithm for the purpose of crater detection became main valuable goal due to the previous critical study of different techniques and the analysis of their effectiveness purpose of calibration (Di Stadio et al., 2002), extended to calculate the age estimation for different areas in the lunar map with a different angle of illumination and image resolution value.

1.5 Objectives of Research

- Create and apply a template-matching automatic crater detection algorithm on different images of Lunar Data with varies rates of image resolution value.
- Compare and analyze the obtained results with the manually detected referenced data (Hiesinger et al., 2003; Fisher, 2014).
- Calculate the estimated age for the areas of interest automatically and construct the clear aged map.
- Apply an algorithm for distinguishing the secondary craters and studying their effect on the age-estimated calculation.

1.6 Methodology

To achieve the above objectives, craters formation and many of their detection algorithms had been studied to choose the most reliable and precise one according to the results obtained. A template matching CDA that has been created using MATLAB software and applied. An extended approach of the estimated age calculation had been also constructed automatically by MATLAB.

From six generic 3D-crater-models, gray-value images of craters are created and subsequently compared to parts of the original image by means of cross-correlation. The sensitivity, i.e., detection threshold, of the automatic algorithm is determined by adjusting the CDA-inferred age estimate to a manually obtained age estimate for a small reference area. The algorithms proceeds gradually on parts of the full image data in some cases for the purpose of calibration, followed by an evaluation process to be applied to other parts of the image data or to the whole image data.

Extending the automatic crater counting to large areas, using the previously determined detection threshold, results in an age map of the large area. A comparison of such an age map to geological or spectral maps of the same area is insightful from the geological point of view. Finally, applying an algorithm to distinguish the secondary craters from the total candidates is to provide more robust and trust to the established CDA.

1.7 The Recognition Problem

In an automatic decision where there is no man intervention, the recognition problem is the main important part to be studied and discussed in computer vision. There are many algorithms developed to detect a certain shape of the object in 2D images. For more complex data, it can be using the more interesting application to generate 3D data, while it also possible to apply 1D non-banal application as it in time signal analysis.

The recognition means the identification of certain shape object due to a given set of features to describe that object. The recognition concept is commonly applied in many different fields of study and research, but the methodologies implemented in each field can be different. Choosing the right practical technique applied for recognition based on the characteristics of the data and the knowledge type of the object required to recognize (Di Stadio et al., 2002). In remote sensing applications, there are different types of noise or distortions that corrupt the images, but the features of the object given to the system will help a lot to define the object with a large approximation.

The main basic element in the detection process is how to define the required object for detection. Consequently, an ideal model that contains the most related features from the required object to detect is applied to the image data as a reference template for detection. There are different types of object recognition techniques that can be distributed into two families; the matching algorithms and the voting techniques families. The matching algorithms group is basically using a simplified template that includes the more relevant features of the required object to detect, but the voting techniques family are using a schematic shape model as an input reference model based on majority voting for classification and detection (Di Stadio et al., 2002).

The main part of this study is to classify the craters' candidates into craters or not, and using the chosen ones in the age estimation process and, consequently, the age maps creation. As a clustering problem, finding the clusters of craters is a main element in secondary craters detection algorithm to evaluate the effect with respect to age estimate and craters dense in age maps.

1.8 Thesis Structure

The contents of this Thesis are divided into ten chapters. Each chapter consists of several main topics and sub-topics. The first chapter is a general introduction to the whole project. This chapter gives a very short introduction about the craters and the problems related. Besides, the main objectives of this project were stated and an overview of the project was presented. The project methodology was explained and the gathering of information was outlined.

The second chapter is about the literature review of craters and the image based crater detection previous algorithms. Here, the background of mage based CDAs was discussed. Research and investigation of the previous studies were carried out and a brief discussion was done on some of CDAs and their techniques.

The third chapter provides detailed explanations of the project methodology. The third chapter is about the template matching, the applied image-based CDA, and its related supporting tools such as the cross-correlation and the k-means algorithm. Chapter three explains also the applied secondary crater detection SCD method, which includes discussion regarding clustering analysis and the Voronoi diagram.

In chapter four, an accuracy evaluation for the automatic CDA is discussed in view of the surface age of different lunar regions in Mare Cognitum and Oceanus Procellarum. The resulted ages have been compared with referenced absolute model ages (AMAs) given by Hiesinger et al. (2003).

Chapter five talks about two extracted large parts of craters (Ptolemaeus and Alphonsus) surfaces from the LU78287GT catalog (Salamuniccar et al., 2014). These manually detected regions were under the created MATLAB functions in order of investigation and comparison. Different crater detectors have been applied for better comparison performance. Surface ages have been calculated under different applied crater detectors with the deep discussion.

In chapter six, the third region of a test of the small size Hell Q crater provided in NAC image was under investigation and testing processes. Analysis of the impact (CSFD) has been done to this high-resolution image and the AMA of the surface has been derived

after a calibration process based on reference manual crater counts (Fisher, 2014). A spatially resolved map of the AMA has been created by applying the supplied image-based CDA.

Chapter seven contains a full discussion of the forth area of test lunar farside crater (Tsiolkovsky). The chapter starts with applying the image-based CDA and the automatic age estimation to the mare homogeneous part of (Tsiolkovsky). Age maps have been created before and after applying the secondary crater detection SCD method in comparison with referenced manual crater counts (Pasckert et al, 2015).

Methods and ideas for improvements of the image-based CDA were suggested in the last chapter, chapter eight. Besides, ideas and recommendations for age mapping and SCD future enhancement were proposed.

Chapter 2

Literature Review

2.1 Historical Review

In this chapter, there will be some short identification to the most important crater detection projects in the world. Then some main techniques applied for automatic detection of shapes and features in images were mentioned and considered. Some discussion and analysis will be presented for the problem of carters' localization and impact craters recognition. There are a brief study and analysis of different applied algorithms and their effectiveness.

This chapter is a presentation of previous works, ideas, and implementations that have been gathered for the project about the history of craters types, CDAs and age estimations for planetary surfaces. Scientists have been started with impact craters identification in the second half of the nineteenth century, an impact crater Meteor was first identified in Arizona by Daniel Barringer (1860-1929). Craters are approximately circular in shape existed on the surface of the Moon, a planet or any other solid object in the solar system (Liu et al., 2011). Craters are the main tool as historic identification points that are used for flow movement estimation in landing control planetary tests. There have been many studies regarding craters as it contains the crucial heritage of information about the geologic formation and age estimation of planetary bodies. Craters exist in many different types; they are an impact, volcanic, subsidence, maar, pit, explosion, Machtesh and Crater Lake (Ravikumar and Sreedharan, 2016).

The circular shape feature is actually a very good candidate to define a crater model for identification. The impact crater can be defined as a surface circular depression in the moon surface or any other planetary object in the solar system (Vijayan et al., 2013). The Impact craters usually exist in different shapes ranged from very small, bowl-shaped to very large, complex and multi-ringed shaped while the volcanic crater can be considered as a circular ground depression occurred by volcanic activities (Christoff et al., 2017).

Craters considered as the main source of topographic features on planetary image surfaces, which sometimes provide sometimes large dimensions and valuable depth. The craters are founded on all hard–surfaces bodies in the solar system as on Moon or Mars (Marchuk and Simonov, 2005). In addition, the craters are also considered as the most important landmarks for rover navigation and missionary spacecrafts, which provide a very high precise landing process, and accurate identifications for the autonomous spacecrafts. (Mert and Ashyralyyev, 2010). A number of experts and scientists usually create craters datasets where they have to examine and analyze the satellite source images and gathering the information for craters features. Barlow catalog is one of the most comprehensive craters datasets that includes about 40,000 craters on Mars with their characteristic information.

Craters are the clearest and obvious landform existed on a planetary surface that could carry the important signs and secrets to the planetary science as it considers as the basic elements in surface age estimation or as landing masks and other applications. Due to the high varieties in the landscape forms, brightening and lighting scale, there are a lot of previous and current trails to distinguish craters types by using remote detecting pictures with the aid of an extraction method that relies on effective crater feature. By applying the gist features that can give reliable depictions on craters' nearby edges and crater detection structure, the results constructed are more precise and trusted.

Studying and Classifying the craters existed on different planetary objects of the solar system is an essential work for planetary scientists as the craters are the perfect tool used as route historic points that give some advance benefits for exact movement estimation for landing control process in aerospace planetary tests. However, with the available vast volumes of images information obtained for Moon, Mars and other planetary objects, the manual recognition and investigation have turned into a very time consuming and tedious process (Yin et al, 2013). Consequently, the idea to build different automatic algorithms for detection and investigation became a high requested goal.

2.2 General Aspects of Crater Detection

Impact cratering is a very common geological process that occurs on all planets of the solar system, and craters are commonly analyzed to estimate the relative ages of surfaces that have not been sampled before (e.g., Michael and Neukum, 2010). A technique of manual counting of craters that based on crater size-frequency distributions was developed in the 1960s and its relation to the surface age (Hartmann, 1964). Manual crater counting has been used for decades to estimate ages of the surfaces of various planetary bodies (e.g., Hartmann, 1964; Michael and Neukum, 2010). Currently, manual counting still dominates the field of age estimation of planetary surfaces. However, a single standardized approach for the assessment of impact craters and measurement of their sizes has not been developed for use in the process of absolute age determination of planetary surfaces.

There have been a number of tools developed to support the scientists in manual CSFD measurements. Examples are the CraterTools software developed by Kneissl et al. (2011) and the CraterStats software package developed by Michael et al. (2010) that helps to estimate the AMA. Most of these tools simplify the process of working with crater information, but the crater counting still has to be performed manually. "Crater counting," means the detection of craters, marking the center positions and measuring the crater diameter.

Availability of high-resolution images of the Moon provided by the Kaguya mission (Ohtake et al., 2008; Haruyama et al., 2012) and Lunar Prospector (e.g., Chin et al., 2007) provide an opportunity to analyze and extract more geological information than before. The resolution of those images is up to a few meters per pixel, which allows for the identification of craters as small as about a dozen of meters in diameter. That could provide unprecedented precision for age estimation of the surfaces on the Moon.

This also increases the time required to identify these geological features and urges the development of an automated counting system. Many automated CDAs have been instructed and developed to give various sizes of impact craters with respect to some basic conditions such as the angle of view and illumination and geological complexity. The automatic CDAs can be classified into two main classes, the first one is the image-based algorithms and the other one is the elevation-based.

The scientists are usually implementing the threshold-based technique in their CDAs in order to distinguish craters types and craters parts. In the image-based approach, it is classically using some techniques such as Haar transform, pattern recognition or gradient using for the purpose of crater detection.

There are many challenges involved in the (CDAs) that have been presented last decades (Kim et al, 2005). Nowadays, valuable crater detection in planetary image datasets remains an important and challenging task according to the following reasons:

1- The lack of real effective common features for distinguishing craters from other landform formation shapes is the first challenge. The craters are different by their size in the order of magnitude. They have different levels of erosion due to the previous millions of years resulted in shapes that significantly far from circles shape. There are a lot of overlapping areas that give more complication in background research and separation.
2- The second obstacle is the non-homogeneous morphology of surfaces in image dataset where most of the surface morphology existed are non-uniform. The planetary images are also obtained from different angles of illumination with different values of resolution that affect the image quality, which reflects unclear morphological crater features than what other images given.
3- The rare amount of large craters, which can be easily identified, and the vast amount of small craters that gives a very high difficulty for detection accuracy are representing the third challenging point. These two unbalanced directions affect the size distribution of craters in planetary images.

The key procedure and one of the main factors that affect the craters recognition results is the highlight extraction for craters image data. The highlight extraction is considered as the helpful efficient element must be applied in brightening points, diverse scales and landscape recognition.

To identify an appropriate value for the sensitivity of the detection algorithm, i.e., the detection sensitivity which governs the fraction of missed and false positive craters, manual crater counts of a small reference area are used. Using the correspondingly determined threshold value, the CSFD can be determined automatically for large regions surrounding the reference area.

In general, the field of crater detection is an interesting and important topic in planetary science, which traditionally relies on the manual inspection of orbital images (Michael and Neukum, 2010). In the domain of remote sensing, automatic CDAs are an attractive approach for researchers that reduce the time required to analyze large amounts of planetary image data and provide the locations and sizes of craters in images automatically (Salamuniccar and Loncaric, 2008; 2010; Honda et al., 2002).

2.3 Related Work for Crater Detection Algorithms

In this section, a short representation of the previous related works and the most active scientists in Crater's detection algorithms is given here. Many applications in Lunar and planetary science require robust crater detection algorithm (CDA) with a high confidence level. Hartmann (1964) used at that time what was considered a new catalog of lunar craters diameters for the size distribution analysis. And by the next year, Hartmann (1965) used the newly discovered impact craters for the lunar crater production rate estimation on the Canadian shield that led him to expect the (3 Ga) to be the average lunar mare age. The age assessment of the craters used to depend on the accumulated number of impact craters (Hartmann and Neukum, 2001). According to Neukum et al. (2001), the CSFD is known for the bodies of the inner solar system. The "production function" describes the dependence of the cumulative frequency of craters larger than a certain diameter on the age of the corresponding surface (Hartmann and Neukum, 2001).

Impact craters are the basic elements of the planetary record, which carry the information, and changes that might happen all over the past years. They represent the main features of any planetary body including the Moon (Vijayan et al., 2013). Through the CSFD measurements, these basic characters-impact craters information carriers used by Baldwin (1964) for the purpose of age estimation. Manual crater recognizing is not a simple task even for professional human experts due to the smaller size of craters and their condense presence. According to Vijayan et al. (2013), impact craters are commonly subdivided into either simple craters (Pike, 1976; Ravine and Grieve, 1986) or complex craters (Allen, 1986).

There were some studies and analyses by Hartmann (1973), Soderblom et al. (1974), Neukum and Wise (1976) that resulted in wide range of chronologic systems, but without a firmed common assent for the estimated absolute ages. Different stratigraphic units were studied and mapped on Mars by Tanaka (1986) and Scott et al. (1987). Relative ages of such units can be determined based on the principle of superposition (Hartmann and Neukum, 2001). However, the impact crater densities lead to the absolute age estimation. All of these studies and research were based on manual CDAs.

Fitting a cumulative production function in polynomial form to a partial CSFD is a very efficient technique for estimating ages of surfaces that have already processed with partial resurfacing events (Michael, 2013). Due to resurfacing, the crater diameters in some units only span a limited range. This technique is used for obtaining the time of formation of the surface and the time of the resurfacing event (Michael and Neukum, 2010).

Michael et al. (2012) used techniques, which depend upon the idea that impact crater formation is a random process, and its cumulative effect on a given finite area should be a main characteristic of the surface age. Michael's purpose was to implement a new routine use of a spatial randomness analysis, in addition to the more common crater density counts. This technique was implemented under two important assumptions:

1. The studied surface has a uniform age. The lava flow is a good example of such surfaces that sometimes can be easily identified.
2. The crater population should not contain members, which cannot be considered to be of independent origin. As a conclusion for this assumption, the fragmented impacted primaries and secondary clusters, which pollute the craters population, need to be excluded.

Much information about the geologic history of a surface can be inferred from identified impact craters. Most studies have extracted statistics and size information based on human experts. The crater counts are varying usually between experts and volunteers and even among the experts themselves once the technique changed (Robbins et al., 2014). Robbins et al. (2014) activated a study of eight professional researchers, analyzing impact structures, comprising small craters with diameters of 10-500 m and larger craters with diameters between a few hundreds of meters and several kilometers.

The results, which depend on crater diameter, number of craters per diameter bin, and terrain type are sometimes varying to reach a percentage of ~± 45% (Robbins et al., 2014). The caution must be considered especially when interpreting small variations in CSFDs. This gives an indication that the variety in the number of the obtained detected craters and the crater density are naturally affect the automatically estimated age.

The availability of high-resolution images of the Moon provided by the Kaguya Terrain Camera (TC) by Ohtake et al. (2008) and Haruyama et al. (2012) or the Lunar Reconnaissance Orbiter Narrow Angle Camera (NAC) by Robinson et al. (2010) provides an opportunity to analyze and extract more geological information than ever before. The resolution of those images may reach up to < 1 m per pixel or better, which allows for the identification of craters down to ~10 m or less in diameter. That might provide unprecedented accuracy for age estimation of the lunar surface. However, the high resolution and huge amount of data also increase the time required to identify these geological features and suggests the development of an automated counting system.

Hence, it has become an important research topic in remote sensing to develop (CDAs), which automatically determine the locations and sizes of craters in images (e.g., Salamanićcar and Lončarić, 2008; 2010). Numerous CDAs have been developed because of the high importance of knowledge about the impact crater distribution for remote geologic studies of planetary surfaces (Stepinski et al., 2012). However, many works about CDAs are limited to the demonstration of the accuracy of a particular algorithm on a small set of test images displaying quite simple and clearly pronounced craters, while meaningful studies in the field of planetary science require CDAs achieving a high performance also for less obvious, e.g., degraded, impact craters (Stepinski et al., 2012).

According to the fact that most of the craters found are considered small size, and these small craters are not easily visible on the global image (Vijayan et al., 2013). Consequently, automatic CDAs have been created and developed as one of the most important applications that deal with crater detection on any planetary surface (Honda et al., 2002). There are two common types of automatic CDAs due to the data source of the image, either image-based or elevation (DEM)-based. The image-based algorithms implement gradient approach and pattern recognition techniques for the purpose of craters extraction (Sawabe et al., 2006; Urbach and Stepinski, 2009), while the machine

learning technique is used for craters identifications by depression in the DEM-based approach (Kim et al., 2005; Stepinski et al., 2009).

Small craters are much more frequent than large craters, but these small craters are often not easily visible in global image data sets. A variety of different CDAs have been constructed and developed by researchers who recognized the importance of the impact craters distribution and its strong effect on remote geologic studies of planetary surfaces (e.g. (Stepinski et al., 2012)). An issue of special importance has been to increase the level of detection performance for planetary images with the reduced clarity of impact craters by creating new CDAs or by refining existing techniques (Stepinski et al., 2012).

Since more than a decade ago, a multitude of new approaches for automatic crater detection has been developed - See (Salamuniccar and Loncaric, 2010) - for a detailed overview. The developed CDAs are usually divided into two classes, where one group of algorithms detects craters in images while another group relies on digital elevation models (DEM)s for crater detection (Salamuniccar and Loncaric, 2010; Di et al., 2014).

Current automatic CDAs typically rely on geometric or morphometric properties of the craters and use a single-stage classification scheme (Salamuniccar and Loncaric, 2010). In machine learning, however, it has been shown beneficial to use a two-stage classification. While the first stage detects many candidates and produces a lot of false positives, a second classification stage is trained to remove the false detections from the candidates which can be called as craters fusion (Enzweiler and Gavrila, 2009). For several decades, studies of impact crater populations have been used to create model ages of planetary surfaces in spite of the assumption that the crater counts are definitely invariant (Shoemaker and Hackman, 1962). There are many studies had been done before that focused on the analysis variation between expert crater counts scientists or even within the same scientist from day-to-day.

According to Stepinski et al. (2012), some image-based CDAs consist of techniques which process the image to detect the characteristic circular or elliptical shapes of crater rims, followed by a matching stage such as the Hough transform (Hart, 2009), while other CDAs employ machine learning approaches for crater detection. These systems are trained using image data sets labeled by human experts, and the detector performance is tested on new image data not used during the training stage (Stepinski et

al., 2012; Chung et al., 2014). Examples for classifier architectures are boosting techniques allowing for a combination of various feature detectors (Wetzler et al., 2005; Salamunićcar and Lončarić, 2010; Di et al., 2014; Stepinski et al., 2012) and support vector machines (Wetzler et al., 2005; Chung et al., 2014).

In general, most of the previous CDAs are limited to crater detection and counting with a lack of any other information (Bue and Stepinski, 2007; Salamunicaar et al., 2011). A new craters identification methodology presented by (Bue and Stepinski, 2007) that utilized more advanced geological information in addition to the previous extracted images information. They have created thresholding-based maps by translating the topographic information into a parallel image. From these maps, they can recognize the craters through a mixture of division and identification calculations. Their technique calculation resulted in numerous small craters that are not detected manually before; in contrast, they neglected them to distinguish craters in high-density areas. They presented a quality evaluation of the technique calculation.

Automated CDAs can be split further into several groups, one group based on edges and Hough Transform as in Sawabe et al. (2006), who propose a multistage approach on edge detection and fuzzy Hough Transform. It uses multiple heuristics methods to detect impact craters. A crater detection rate of 80% compared to manual detection was obtained by Sawabe et al. (2006). Another group is the neural network-based approach as by Cohen et al. (2016), who propose a CNN (Convolutional Neural Network) technique. In contrast to other approaches, CNNs do not have to use handcrafted features; instead, they learn optimal filters and features from training examples (for an overview see, e.g., Simard et al., 2003). A drawback of the CNN approach is the need for a large number of examples to be used for training, which needs to be extracted and labeled, as well as long training times. Recently, methods not based on images but on topographic maps have been developed to address CSFD measurements (e.g., Salamunićcar and Lončarić, 2010; Yin et al., 2013). In contrast to image-based methods, they are not affected by illumination, visual surface properties, and atmospheric conditions (Troglio et al., 2010).

2.3.1 Image-Based Automatic Crater Detection

In general, the image–based crater detection approaches can be divided into two main groups, the first which based on machine learning (supervised) and the other implements the machine learning techniques (unsupervised-fully autonomous).

The machine learning-based detection algorithms depend on pattern recognition to define the craters candidates' boundaries to have circular or elliptical features in an image followed by a reprocessing for the image to enhance the edges for the craters candidates' boundaries (Stepinski et al., 2012). The last step of this process is applying a technique for the final crater detection such as Hough Transform variants. The final decision distinguishes the craters widely rely on the mechanism of the supervised machine learning and the implemented decision tree algorithms The image-based CDAs are basically dependent on the illumination and the viewing angle

The second group of the image-based CDAs is applying the machine learning to facilitate the detection process. In such group algorithms, there are two processing phases. The first phase is the learning phase while the second one is the detection phase. Creating training sets of images to feed the algorithm is the main duty in the learning phase. The training set consists of the labeled craters that have been detected by the domain experts. But in the detection phase, the algorithm implemented previously to the training set is then used to an unlabeled new dataset of images using a template-model technique., which is a continuously scalable technique.

Sawabe et al. (2006) proposed a multistage approach to edge detection and fuzzy Hough Transform. The author reports a crater detection rate of 80% compared to manual detection. Complete and incomplete crater rims appear in the image as arc-like structures of edge pixels, which are assigned to circles using the fuzzy Hough transform approach (Sawabe et al., 2006). Crater detection is favorably performed for low-sun images, in which the bright rims and cast shadows associated with craters are well visible and form circular edges (Sawabe et al., 2006).

Kim et al. (2005) had proposed that the automated calculation in crater recognition is presented with more additional image information. Besides that, the calculation is practically quicker to be imaged and showed more deep details for a new assortment of

distinctive Martian geomorphologic regions by implementing the sensors Mars Orbiter Camera (MOC), Mars Orbiter Laser Altimeter (MOLA), Viking Orbiter Camera and High-Resolution Stereo Camera (HRSC)). They have made an evaluation and comparison of the results obtained from both the automated cavity areas and the physically inferred Mars Crater Consortium (MCC) including the physically secondary holes. Their evaluation study results achieved in craters identification a precision percentage between (70% - 90%) and in a quality component (60% to 80%) percentage depending on the sensor applied and the geomorphology. They presented also the craters candidates positions in the HRSC images relying on a correlation process between the manually (CSFD)s and the mechanized inferred craters.

Oliva and Torralba (2001) suggested a computational model that relies on a low dimensional representation of the image data prospect to analyze the spatial surface to identify the craters candidates. They constructed a method that chose special features calculations (toughness, harshness, openness, expectation, and development) to analyze the current spatial structure of the image. From that point, they found that their calculations and measurements are very trusted especially when they use coarsely restricted data. A multidimensional space that shares various surface semantic classifications such as (avenues, roadways, and coasts) will be the obtained model.

Vinogradova et al. (2002) are considered as one of the first who implements feature recognition systems for impact crater detection on Mars. Another study by Leroy et al. (2001) which appears to be quite a successful one is the automatic detection and 3D modeling of small craters on an asteroid.

Another study by Honda (2002) has proposed a CDA for a large-scale image dataset. The original images of interest are separated into groups due to their (CSFD) patterns. Honda (2002) used a noise reduction technique and optimized parameter sets to identify the craters candidates. Moreover, by applying the self-organizing map (SOM) approach, the false craters candidates are neglected. The final results gave the impression of high accuracy in classification using this approach, but the detection process of this system needs some more developing steps.

Cheng et al. (2003) have presented developing and applying a CDA to an automated navigation over extra-terrestrial small bodies. Magee et al. (2003) presented results

extracted from automated impact crater detection by using template matching and edge processing. Kim and Muller (2003) had applied a similar method of crater detection but implementing texture analysis and ellipse fitting on DEM and optical image. Generally, there are much more techniques have been developed for automatic crater detection but without a unique consensus on the obtained quantitative information and their accuracy, completeness, and reliability.

Optical landmark navigation is another application that uses the craters of the surfaces as landmark positions for aircraft landing or taking off. This is first implemented by the Near Earth Asteroid Rendezvous (NEAR) mission (Cheng et al., 2003). The obtained data are considered to be of high importance for planning of the orbital parameters (Shang et al., 2011). Many landmarks tracking navigation algorithms based have been developed to meet the requirement of long communication delay and complex gravitational field around asteroids (Shuang and Pingyuan, 2008).

Grigorescu et al. (2002) utilized the obtained data from a bank of Gabor filters to be under analysis. They have proved that the power range obtained from Gabor filters affects the surface elements. Their comparison based on a quantitative method that relied on Fisher's criterion. They have shown in general conditions, the favoritism efficiency of the related features increase with corresponding to the post-Gabor processing. They applied two analyzing methods to experiment with the ability to compare administrators to deliver exacting feature for individual surfaces. They have applied both Fisher measure and grouping correlation. The obtained results in both cases were very reliable and steady as the grinding cell administrator gave the best division results. In addition, the grinding cell administrator did not give false reaction to non-surface highlights in a way that affect the results negatively.

Another approach for impact craters identification presented by Bandeira et al. (2007) is based on the analysis of a probability volume created by template matching implemented on the surface of Mars.

Liu et al. (2011) combine the semi-supervised learning technique with dynamic learning to produce a new semi-supervised dynamic crater class determination method that results in craters location extracted from panchromatic planetary images data. They applied the semi-regulated active class selection method to prepare a group of the

dataset that identifies the holes and craters shapes in a large volume of images, without any type of human marking interference. They have applied two methodologies to improve the craters' locations precision by relying on the investigation of unlabeled candidates. First, they have applied to apply the Majority Vote strategy to obtain new class marks with the aid of the unlabeled candidates in the image. Then they have utilized the Active Stability strategy method to get the better fitting class to the dataset to identify the unreliable resulted classes. The resulted calculations are practically evaluated on another Martian image that presented an active cratered landscape analyzed by heterogeneous surface morphology. Finally, the results give the proposed approach a very high degree of precision and exactness than any other method applied in the same conditions.

Ding et al. (2011) have presented an auto-detection system of sub-kilometer craters. The proposed work consists of three main steps. The starting step was to apply numerical morphology to distinguish in a skillful way the areas in the image data that contains the craters cavities (candidates). Then as a second stage, they start to characterize the candidates precisely into craters or non-craters according to certain regulated boosting outfit learning calculations in the highlighted compositions. Finally, they improve location execution in the surface morphology through coordinating move learning into boosting with a comparison to the preparation set. This structure was implemented on Mars image data of 37,500 × 56,250 m^2, which strongly filled with carters candidates by non-homogeneous surface morphology.

Lui et al. (2012) have proposed a new investigation process on the unlabeled candidates. The process relied on three procedures to improve the precision of craters identification through mixing the characteristics. They first applied the majority vote technique procedure to get the best results from the unlabeled candidates. Then they implemented the De-Mixed procedure on separated samples to acquire dependable candidates. Finally, they also utilized the Active Strength Strategy to select the best circulation class in the detection process to obtain more secured datasets. Consequently, these three previous methods choose effectively testing cases from the images data to prepare complete data while the classifier running continually. They have made an assessment of a huge Martian data image, which gave actively description of the non-homogeneous surface morphology.

The developing step after such CDAs is the automatic classification and extraction of further contextual information in addition to the crater detection itself (Vijayan et al., 2013). The CDA implemented by Vijayan et al. (2013) depends on classifying the craters into those with rounded and with flat floors. This CDA was used to detect simple lunar craters larger than about 50 m and exclude smaller ones. The CDA implemented in Vijayan et al. (2013) divides the craters into groups with different floor shapes. It was used to distinguish between different crater degradation states and for the detection of simple lunar craters of small diameter (Vijayan et al., 2013). Vijayan et al, (2013) made a checking process for each detected crater and then evaluate its state of degradation by determining the intensity variation across the crater edge.

Cohen et al. (2016) proposed a CNN (Convolutional Neural Networks) approach. In contrast to other approaches, CNN does not have to use handcrafted features, instead, they learn optimal filters and features from training examples. Firstly, there is an interface between the input image and the network to be considered as the first convolutional layer. There is a sliding window moving across the input image at each position, and each pixel is multiplied by its corresponding filter and summed together with the previous one to result in a single value. A new picture will be formed based on the obtained new results of these convolutions. This process will maintain spatial information to be used later in the second step (Cohen et al., 2016).

The CNN of Cohen et al. (2016) receives input images rescaled to a size of 15 by 15 pixels. It has two convolutional layers consisting of feature detectors of 4 by 4 pixels size, and one fully connected layer. Using softmax regression, the output layer denotes the probability of the input pattern to represent a crater or not. The CNN is trained based on the technique of stochastic gradient descent.

It is well known that training an CNN requires a very large number of training samples which have to be annotated by a human expert, which is a limiting factor for the application of similar supervised machine learning methods to the problem of crater detection.

2.3.2 DTM-Based Automatic Crater Detection

Craters can be detected based on Digital Terrain Model (DTM) due to their elevation value. A DTM represents a height profile, which is usually generated by means of laser scanning or by stereo image analysis methods. In laser scanning, a satellite equipped with a laser altimeter scans the surface with laser pulses and determines the distance to the surface based on their time of flight, while in stereo image analysis an algorithm generates a DEM based on two or more images of the surface (Schowengertdt, 2007).

In a DTM, the elevated rim of the crater appears as a bright region and the depression appears as the dark part of the crater. The planetary surfaces are usually filled with craters and their features; they contain some small crater depressions due to previous impacts. Consequently, in order to eliminate these depressions, a smoothening process is applied in some cases to DTM images data.

When the depression areas are founded and filled, a threshold-based technique is applied to the data to construct a binary image (Taud and Parrot, 1992). It is possible to use one flooding algorithm to fill these detected depressions. Moreover, by implementing some morphological narrowing and thinning operations to get the craters in clearer shape. Commonly, the spatial resolution of DTMs is worse than images.

On the Moon, Mars, etc., there is no difference between DTM and DEM. One example approach had been developed is the combination of the detection algorithm for automatic crater detection and segmentation applied to a digital topography DTM image of Mars (Bue and Stepinski, 2007). The method applied was a threshold-based detection algorithm that based on the delineation of craters by topographic curvature as it considered as the most important parameter to obtain topographic rims of the craters. This algorithm provided a good tool to identify a wide range of size and fresh impact craters but was not very efficient for the heavily degraded craters.

Another approach in DTM-based detection algorithms is the Watershed transform technique, it is possible to implement the watershed transform image segmentation technique, and it is preferred to apply it to the optical DTM data (Ravikumar and Sreedharan, 2016). The Watershed technique will find the gradient of the image only after the pre-processing of DTM image data and apply the marker computation to avoid

the over-segmentation. This marker computation is related to an image by Foreground and Background markers. The morphological operators are used to generate foreground markers while background markers are produced to segment the background side of the image data (Ravikumar and Sreedharan, 2016).

2.4 Standard Algorithms Commonly Used in Automated CDAs

This section provides a short description of standard techniques that are used in many CDAs described in the literature (Hough Transform) or are employed later on in this thesis (Template Matching, k-means algorithm, and Voronoi Tessellation).

2.4.1 Hough Transform

An important technique used for crater detection is the Hough Transform. It is widely applied in various recognition applications that allow detecting shapes in an image by applying “voting” technique on a suitable effective parameter (Di Stadio et al., 2002). The most important and practical voting technique is the Hough transform which describes the accumulator.

Hough transform technique considered as an important member in image segmentation. Hough transform has a high rated popularity in crater detection. The Hough accumulator is a histogram counting how many "positive" points reside on a simple geometric structure. Traditionally, a gradient image is thresholded to derive a binary image. The image is then transformed into the Hough accumulator.

The Hough transform technique is originally performed to detect some simple geometric objects by Hough (1962) with known parametric forms, such as lines, circles, and ellipses (Galloway et al., 2014). The main idea is to build a prototype where the detection process becomes easier computationally. The coordinates of the model are considered as the parameters used to define the requested curve in the image data space (Di Stadio et al., 2002).

In Hough transform technique, it is very important to know how to detect the points of intersections between the image data and the parameters model computationally. The main idea is to construct an array of accumulators over the parameter space model. The

image data and the parameter model are both discretized and divided into accumulators or cells to be presented as a matrix (Di Stadio et al., 2002). Each point or cell in the parameter model gets one single vote for each corresponding image point that included in the curve passing through the cell. The summations of the votes will present in accumulators that identify the image points laid along the line according to the coordinates of the cell. As the number of parameters decides the dimension of the parametric space model, the Hough transform can be also implemented for generic curve recognition relied on analytical representation (Di Stadio et al., 2002).

A simple example of the Hough transform application is the line recognition. There is existed one image data and another parameter model. The points appeared with high values in the parameter model are representing the recognized curves in the image data. The number of the intersections of the plotted curves in the parameters model will result in the values of corresponding image points (Di Stadio et al., 2002).

2.4.2 Template Matching

Another detection technique that is useful for extracting craters from images is template matching. Template matching is a practical application of cross-correlation to find even the small similarity parts between the original image and the applied template. This template must be moved cross the original image from the first position and a similarity percentage must be checked each step. It is, therefore, a simple and effective method to examine two images for their similarity or to detect craters on the moon in this work. The template of a crater is "moved" over the image of the surface to be examined, and for each pixel the similarity of the crater image is compared with the image section of the examined surface. The more similarity between the two images is, the greater the value generated by the function of cross-correlation. A very simple and general example of template matching is shown in Figure 2.1, where the marked window corresponds to the template.

(a) Test image with marked template; image credit: Wong et al. [2008]

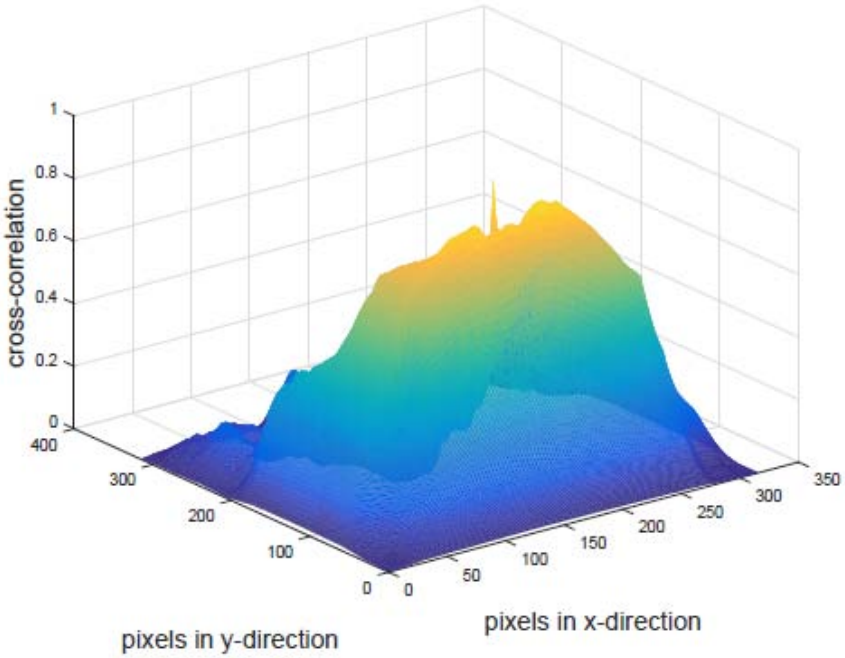

(b) Cross-correlation between image and template (Mühlbauer, 2015)

Figure 2.1: Example of template matching

In the case of craters matching, the cross-correlation technique is applied. The cross-correlation between two functions *f(t)* and *g(t)* is defined as:

$$(f * g)(\tau) := \int_{-\infty}^{\infty} f^*(t)\, g(t+\tau) dt \qquad \text{Equation 2.1}$$

For discrete sequences of functions, it becomes:

$$(f * g)[n] := \sum_{i=-\infty}^{\infty} f^*[i]\, g(i+n), \qquad \text{Equation 2.2}$$

In order to compute the cross-correlation for two-dimensional images in a practical way, equation 2.2 is extended in the following way:

$$(f * g)[m,n] := \frac{1}{N} \sum_{i,j} \frac{(f^*[i,j-\bar{f}])(g[i+m,j+n]-\bar{g})}{\sigma_f \sigma_g}, \qquad \text{Equation 2.3}$$

with N as the number of template pixels f, $\bar{f}$ and $\bar{g}$ as the average pixel values, and (σ_f, σ_g) as corresponding standard deviations.

2.4.3 The K-Means Algorithm

The k-means algorithm is used in this thesis to remove multiple detections of the same crater at slightly different diameters. The k-means algorithm (k-means-clustering) is a well-known clustering method of vector explanation, which is very applicable in signal processing especially for cluster analysis (Theodoridis and Koutroumbas, 2009). It is a technique to subdivide N data points into k subsets, where generally k<<N. The optimization goal of the k-means algorithm can be expressed as

$$arg_S min \sum_{i=1}^{n} \sum_{\vec{x} \in S_i} \|\vec{x} - \vec{\mu_i}\|^2 \qquad \text{Equation 2.4}$$

The Euclidean distance is the most common practical example $\|\vec{x}\|_2 = \sqrt{x_1^2 + x_2^2 + \cdots + x_d^2}$ of d-dimensional vector $\vec{x}$. MacQueen (1967) was the first, who introduced the general concept, but the first scientist who published the k-means approach was Lloyd (1982), it sometimes called as 'Lloyd's algorithm' (Mühlbauer, 2015). Clearly, the results obtained from the k-means algorithm is relied on the order in which the vectors are considered (Theodoridis and Koutroumbas, 2009). The k-means algorithm keeps solving between two steps until it becomes very close to find the suitable partition of data that cover the given condition. As a first step, an initial set of means that basically relied on each data point which assign any cluster that holds the minimum value of the error function according to Equation 2.4. The next step consists of a re-assignment of the data points to the cluster centers (Marsland, 2009).

These steps are repeated until the assigned partition into subsets will give no changes anymore. The k-means algorithm always tends to use a local minimum due to the limited range of possibilities of partitioning the original sets into smaller subsets

(Mühlbauer, 2015), but there is a possibility of not finding the global optima in this algorithm (Marsland, 2009) .

The Lloyd algorithm can also be initialized with help of the k-means++ approach (Arthur and Vassilvitskii, 2007).

2.4.4 Voronoi Tessellation

The Voronoi diagram (Voronoi tessellation) is a method of subdivision of a plane into regions that comprise the part of the plane around each point within a distance that is shorter than the distances to the neighboring points (Aurenhammer, 1991). In this Thesis, the concept of Voronoi tessellation will be used to differentiate between uniformly and non-uniformly distributed craters.

A Voronoi edge represents the border between any two Voronoi cells (Lompart, 2017), and the Voronoi edges are included into two adjacent cells as shown in Figure 2.2 (Venkatasubramanian, 2013). Voronoi cells have commonly polygonal shape. A Voronoi vertex is an intersection point of at least three Voronoi edges. (Venkatasubramanian, 2013).

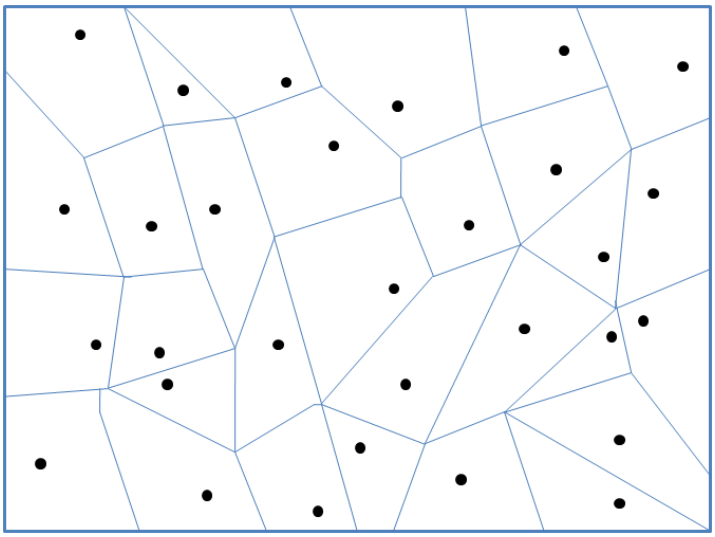

Figure 2.2: An example of Voronoi tessellation

Figure 2.3 shows the application of Fortune's algorithm, which is an algorithm to compute the Voronoi diagram efficiently. Its main idea is propagate the cell information across the plane using a so-called sweep (Austin, 2012).

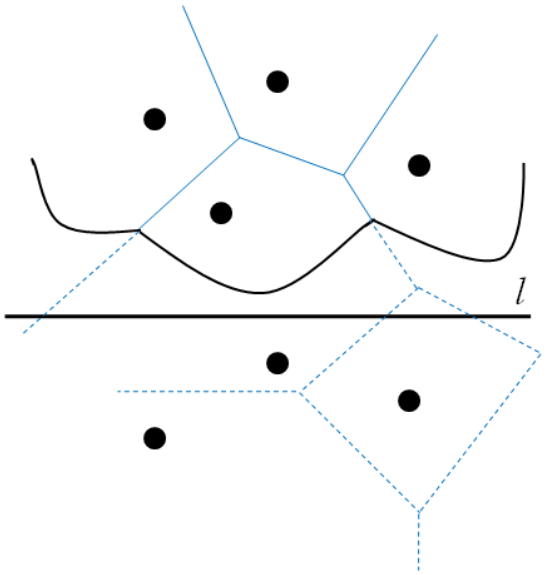

Figure 2.3: Sketch of the sweep line approach (De Berg et al., 2000)

Points on the sweep line belonging to the nearest cell and being located in two bends simultaneously forming breakpoints. The position is on a Voronoi edge, respective parabolic bends are generated when two breakpoints occur on the sweep line. A new edge is created upon disappearance of a bend. This process is repeated until the sweep line scans completely each point on the plane in order to add a new site to the list of sites with respect to the corresponding parabolic bends, and consequently, a new edge is added to the diagram (Austin, 2012).

In this thesis, the Voronoi diagram is used to detect deviation of the spatial distribution of the craters from the uniform distribution by regarding the size distribution of the Voronoi cells. The cell area distribution for a uniform spatial distribution is obtained by artificially generating a large number of uniform spatial distributions, computing their respective Voronoi diagrams and construct a histogram of the cell area. This approach corresponds to a Monte Carlo simulation. A crater in the observed spatial distribution is considered a secondary crater if its Voronoi cell area is below a threshold value, which resembles a one-tailed test of clustering.

Chapter 3

Methodology

3.1 Template Matching Based Crater Detection Algorithm

To detect craters within our testing area, the template-matching algorithm of Grumpe and Wöhler (2013) is applied. It uses six templates which represent six different 3D models of small craters. They were constructed using tracks of the Lunar Orbiter Laser Altimeter (LOLA) instrument (Smith et al., 2010) that contain cross-sections of satellite craters of the lunar crater Plato. The craters are characterized by three basic shapes: the simple bowl shape, a transient shape with a flat floor, and a complex shape with a central peak (Figure 3.1).

Each crater is split at its center point to extract two different profiles. Then these curvature models were rotated symmetrically around the crater center to generate two-dimensional surfaces in 3D space. From these surfaces, crater templates could be obtained by applying the Hapke model (Hapke, 1984, 2002) to render crater template images based on the known directions towards the sun and the viewer.

The obtained templates are grey scale images as shown in Figure 3.2, which are then re-scaled to match a given crater diameter with respect to the image. The similarity between the template and the image is computed by normalized cross-correlation. All available templates were scaled to sizes between 5 and 200 image pixels in order to allow for the detection of craters across a broad range of diameters based on the normalized cross-correlation coefficient between the templates and the image parts being analyzed (Salih et al., 2016). When the cross-correlation exceeds a given threshold, the crater is added to the list of candidates.

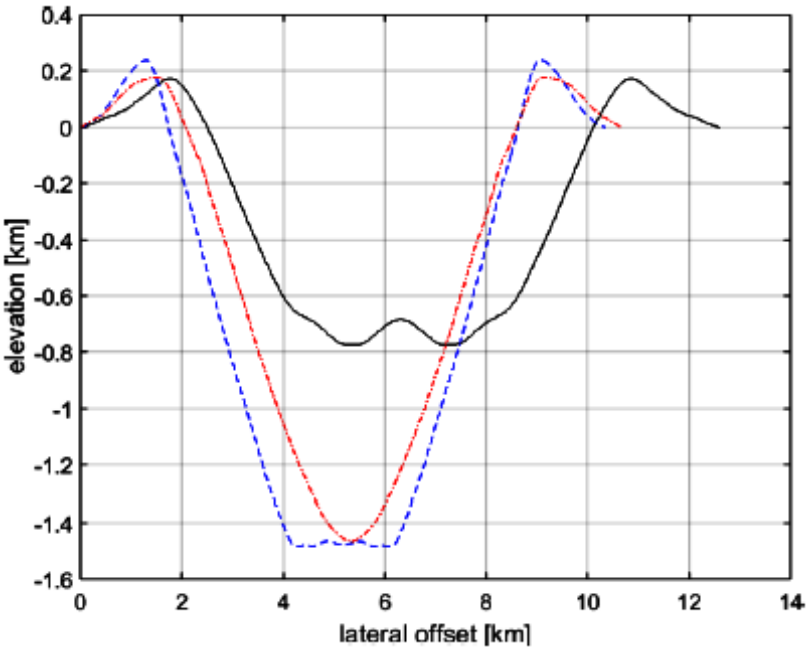

(a) Crater profiles (constructed from southern half)

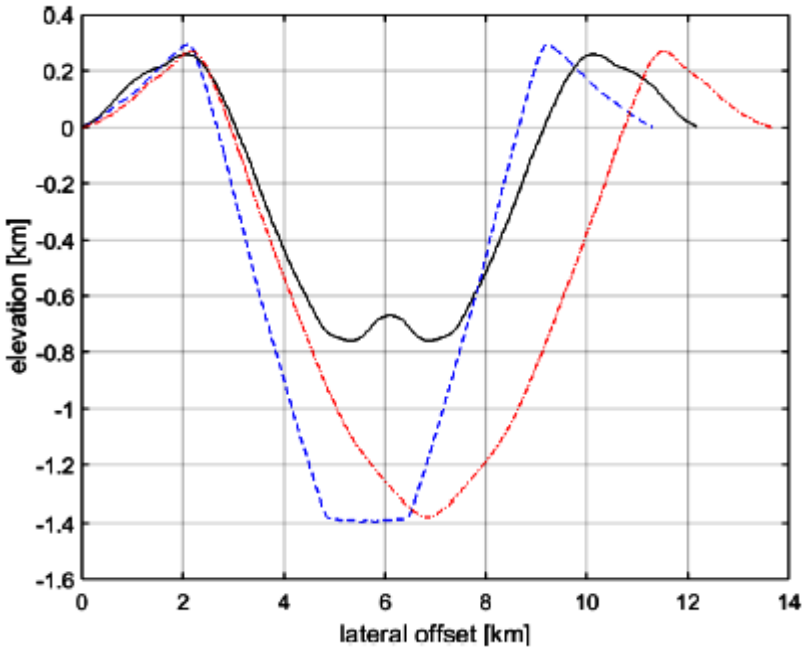

(b) Crater profiles (constructed from northern half)

Figure 3.1: Cross-sections of the crater models. The crater models were constructed from LOLA tracks that closely resemble cross-sections of approximately 8 km diameter satellite craters of the lunar crater Plato. Each track was split at the center of the cross-section, respectively, and the models were derived by rotating the resulting profiles around the center of the corresponding satellite crater, respectively. (a) Model cross-sections derived from the southern half of the LOLA track. (b) Model cross-sections derived from the northern half of the LOLA track. From Salih et al. (2016a)

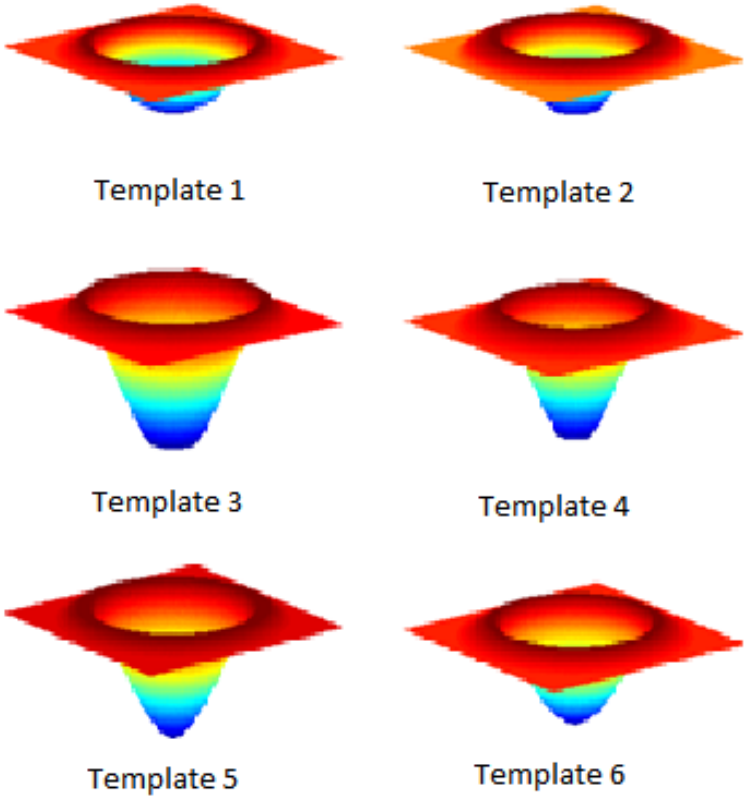

Figure 3.2: The six rendered 3D crater models used for template matching, given typical illumination conditions. Models 1 and 2 represent the small central mounded shape, flat-floored craters correspond to models 3 and 4, and models 5 and 6 represent simple bowl-shaped craters. From Salih et al. (2016b)

The template-matching algorithm examines the similarity between the original image and the set of crater templates at each pixel position. When the cross-correlation exceeds a given threshold, the crater is added to the list of candidates. It can be considered as a reliable yet simple method to automatically detect craters in orbital images of the lunar surface. Since CDAs commonly have, a parameter that defines their sensitivity, it is important to calibrate this threshold based on a small reference area provided with its manual crater counts (Salih et al., 2016a).

Figure 3.3 shows the transformation of a 3-D crated model into a grayscale image by orthographic projection and artificial illumination.

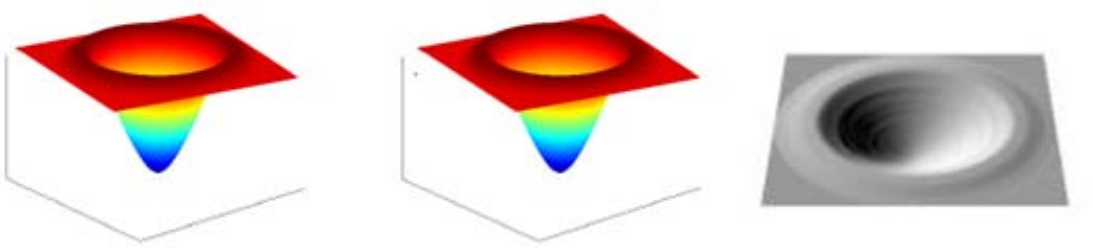

Figure 3.3: Generation of a synthetic crater model

Figure 3.4 shows an example of this procedure as a comparison of applying two different values of threshold (0.7 in case (a) and 0.75 in case (b)) with a limited range of diameter detection (20-1000 m). The area of examination belongs to the Tsiolkovsky crater (See Chapter 7).

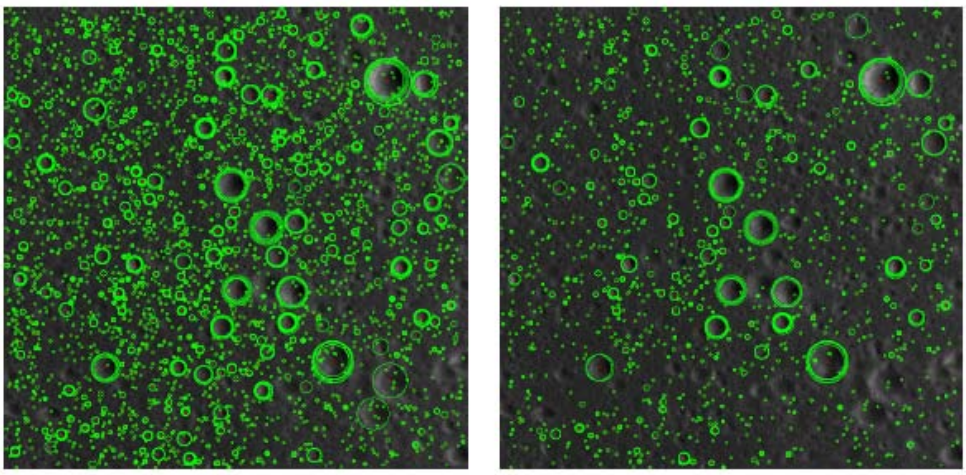

(a) Threshold 0.7 (b) Threshold 0.75

Figure 3.4: Crater detection results without clustering (Mühlbauer, 2015)

Multiple detections of the same crater at the same position with slightly different diameters (Figure 3.4) are removed using k-means clustering as shown in Figure (3.5).

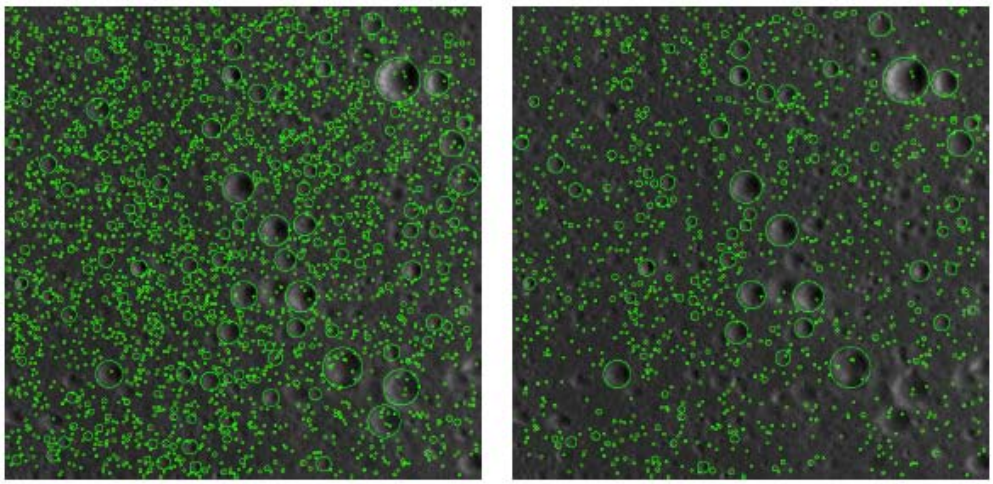

(a) Threshold 0.7 (b) Threshold 0.75

Figure 3.5: Detected craters results with clustering (Mühlbauer, 2015)

An appropriate detection threshold is determined by adjusting the estimated age of a test region to the age inferred from manual crater conting.

3.2 Automatic Surface age estimation

The age of a planetary surface can be estimated by the following steps:

- Infer the coefficients of the production function from the CSFD.
- Derive the cumulative frequency of 1 km craters.
- Find the age for which the cumulative frequency of 1 km craters is matched

According to the fact that the age of a surface can be estimated by assessing the distribution of craters. Some experts (e.g. Neukum, 1983; Hartmann and Neukum, 2001; Ivanov, 2001) believe the crater populations are consistent with the production function has remained constant over the observable history of planetary surfaces.

The most commonly accepted presentation of this approach was given by (Neukum, 1983) which is based on the cumulative crater frequencyN_{cum}, as shown by logarithmic equation:

$$log\ N_{cum} = \sum_{i=0}^{n} a_i x^i\ , \qquad x = log\ D \qquad \text{Equation 3.1}$$

Where N_{cum} represents the number of craters per unit area that exceed a given diameter *D*.

There is some slight difference in the final results of the estimate ages that based on the polynomial coefficients values suggested by the experts (Neukum, 1983; Hartmann and Neukum, 2001; Ivanov (2001) for their age calculations. Slight differences occur in the diameter range of less than 1 km, which increase with increasing crater diameter.

Table 3.1: Coefficients for the age estimation on the lunar surface

	Neukum (1983)	**Neukum et al. (2001)**
$\mathbf{a_1}$	**-3.6269**	**-3.557528**
$\mathbf{a_2}$	**0.43662**	**0.781027**
$\mathbf{a_3}$	**0.79347**	**1.021521**
$\mathbf{a_4}$	**0.086468**	**-0.156012**
$\mathbf{a_5}$	**-0.26485**	**-0.444058**
$\mathbf{a_6}$	**-0.066382**	**0.019977**
$\mathbf{a_7}$	**0.037923**	**0.086850**
$\mathbf{a_8}$	**0.010596**	**-0.005874**
$\mathbf{a_9}$	**-0.0022496**	**-0.006809**
$\mathbf{a_{10}}$	**-0.00051797**	**0.000825**
$\mathbf{a_{11}}$	**0.0000397**	**0.0000554**

In this study, Neukum (1983) production function is applied for fitting the data and describing the CSFD for each bin of age. Table 3.1 shows the first calculated 11 coefficients for each technique of Neukum (1983) and Ivanov (2001) that specialized for Moon surface area and result in reliable ages. The parameter $\mathbf{a_0}$ depends on the age of the respective surface area (Hiesinger et al., 2003).

As the production function cannot alone recognize the age of the planetary surface, the model must be extended to the chronology function in order to obtain the final age. The chronology function describes the changing crater formation rate with time. The chronology function of (Neukum, 1983) has the mathematic description of:

$$N(1) = 5.44.10^{-14}(e^{6.93T} - 1) + 8.38.10^{-4}T \qquad \text{Equation 3.2}$$

Where N(1) represent the number of craters larger than 1 km in diameter per unit area and T is the time in Ga. The formation rate for the choronlogy function is constant back to 3 Ga, then exponentially increasing (See figure 3.6).

Fitting equation 3.1 to the cumulative histogram of measured crater diameters yields the value of N(1) based on the fitted N_{cum} values. Solving equation 3.2 for the age *T*, given the fitted value of N(1), yields the absolute model age (AMA):

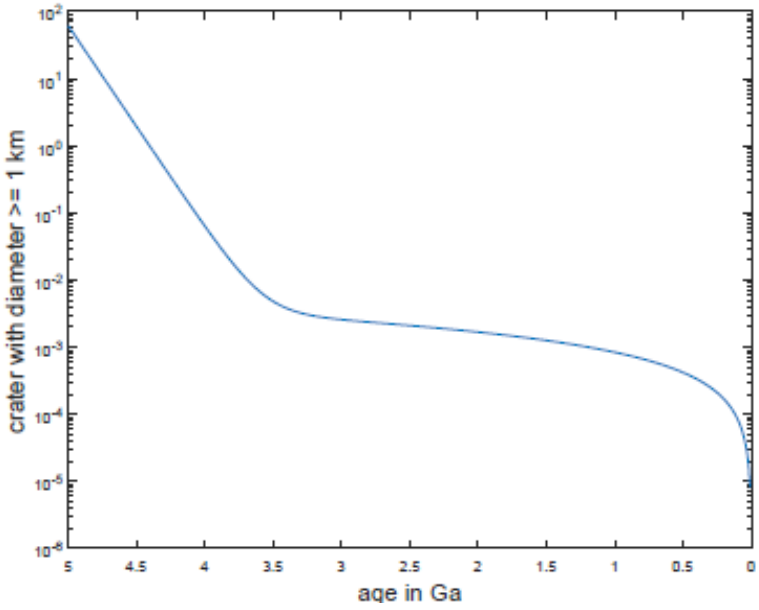

Figure 3.6: Chronology function of Neukum (1983), (from Lompart, 2017)

The age of the surface is divided into five eras: the Copernican age, the Erathosthic age, the Imbrian age, which further divides into an early and a late Imbrian period, and preceding Nectarian and the Pre-Nectarian period.

Table 3.2: Classification of the ages according to Neukum (1983)

Age	Period	Age in Ga
Copernican Age		**0.80 - 0.00**
Eratosthenian Age		**3.20 - 0.80**
Imbrian age	**Late Imbrian period**	**3.80 - 3.20**
	Early Imbrian period	**3.85 - 3.80**
Pre-Imbrian age	**Nectarian peroids**	**3.92 - 3.85**
	Pre-Nectarian period	**4.60 - 3.92**

3.3 Secondary Craters

This section is adopted from Salih et al. (2018).

By definition, secondary craters result from the impact of material which has been ejected by a primary impact (e.g., Shoemaker, 1965; McEwen and Bierhaus, 2006). Early observations of the lunar surface have shown that the density of small craters is much higher on the rays surrounding large and fresh primary craters than outside these structures (McEwen and Bierhaus, 2006). These craters have been considered as secondary craters by Shoemaker (1965), who provided an estimate that many craters with diameters smaller than ~200 m are secondary craters located at large distances from the primary impact.

Many secondary craters are formed in proximity to the primary crater. They do not have a circular outline and are commonly less deep than primary craters of the same size. They often exhibit spatial patterns such as linear chains, clusters, and herringbone patterns, whereas remote secondary craters formed by material ejected at high speed are less elongated and more evenly distributed and thus appear more similar to primary craters (e.g., McEwen and Bierhaus, 2006). Figure 3.7 shows a very good case of secondary craters in the area of Tycho crater (Dundas and McEwen, 2007). Large clusters of likely secondary craters are apparent on the floor of crater Tsiolkovsky (Figure 7.5).

Commonly, it is assumed that small craters on the terrestrial planetary bodies, except those in close proximity to primary craters, are mostly primaries so that they were used as a basis for surface dating (e.g., Basilevsky et al., 2005). However, studies on Europa by Bierhaus et al. (2005), Mars by McEwen et al. (2005), and the Moon by Dundas and McEwen (2007) argued that this assumption is incorrect for smaller craters and that it is necessary to take into account the effect of remote secondary craters for accurate age estimation, especially when relying on CSFDs of craters with diameters below several kilometers, because one primary impact may be able to form millions or even hundreds of millions of secondary craters at distances of up to 1000 km (McEwen and Bierhaus, 2006).

Many planetary studies have considered the occurrence of craters on solid planetary surfaces to be the result of direct (primary) impacts of asteroids, and comets, and based the estimation of AMAs on this assumption.

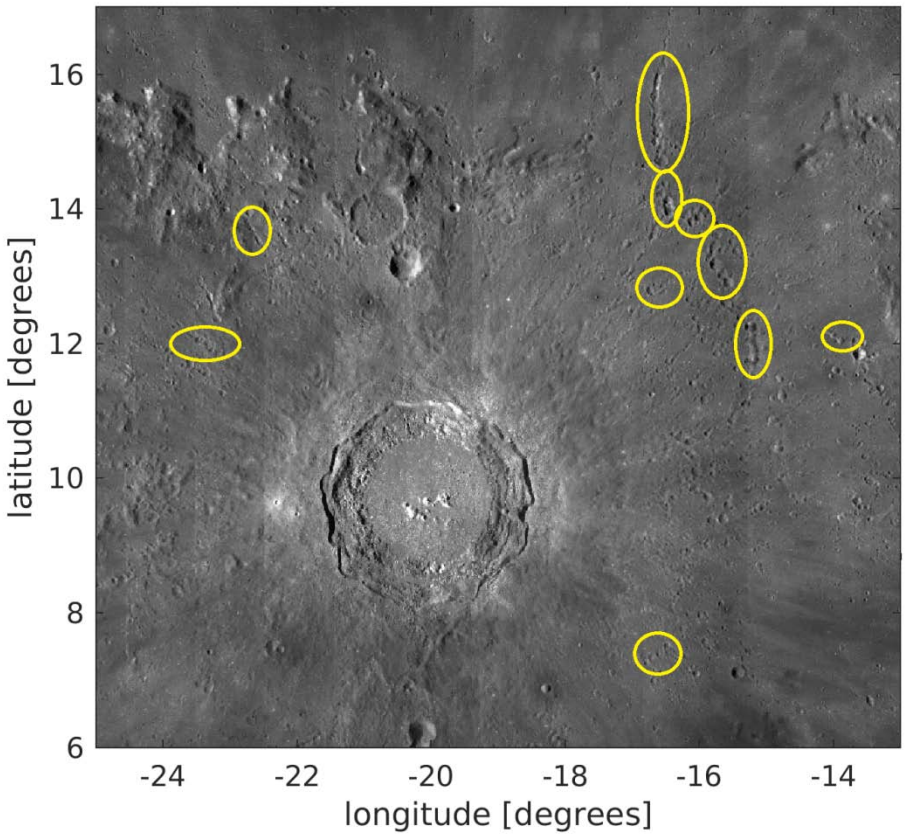

Figure 3.7: Excerpt from LROC WAC mosaic (Speyerer et al., 2011) showing the crater Copernicus. Chains and clusters of secondary craters are marked in yellow.

Most of experts assumed the small craters as a major element for age estimation with one exception of those craters where located in the neighboring areas of large primaries (Basilevsky et al., 2005). Studies on Mercury, Europa, the Earth, Moon, and Mars (Shoemaker, 1965; Bierhaus et al., 2001, 2005, 2006) suggested that the upper limit of diameters for secondary craters is less than 5% of the parent crater diameter. As a general conclusion, McEwen and Bierhaus (2006) stated that the existence of secondary craters is not an impediment against using crater statistics for estimating relative surface ages and those small craters are appropriate for estimating the AMA of young surface areas. They also suggested a technique for reducing the contamination from secondary craters by mapping the possible secondary craters of all large recent craters in a study

area. The absence of craters larger than a limiting diameter of about 1 km would allow for calculating an upper limit of the surface age.

Further refinement of the surface age is then possible based on the so-called crossover diameter, i.e., the diameter value at which the CSFDs of the primary and secondary craters in the study area intersect (Werner et al., 2009). Hence, for diameters exceeding the crossover diameter primary craters dominate the total CSFD while at smaller diameters secondary craters dominate the CSFD, where the crossover diameter decreases with decreasing surface age. Hence, combining the upper-limit age together with the mapped secondary craters would allow for an estimation of the crossover diameter and thus a refined surface age (McEwen and Bierhaus, 2006).

In contrast, more recent work of Speyerer et al. (2016) shows based on impact craters formed during the LRO mission that the 1-year isochron inferred from the production function of Neukum et al. (2001) is consistent with the directly observed crater production without the need for invoking secondary craters. However, the slope of the CSFD in the 10-20 m diameter range is steeper than predicted by Neukum et al. (2001), indicating that the steep CSFD slope at small crater diameters described, e.g., by Bierhaus et al. (2006) is not necessarily due to secondary craters. Similarly, the study by Malin et al. (2006) about recent cratering on Mars suggested that the present-day production of Martian craters cannot be described well by the assumption of most small craters being secondary craters.

Consequently, the secondary craters are easily distinguished from the surrounding primary population of similar diameter based on their distinctly non-uniform spatial distribution.

Chapter 4

The accuracy evaluation in Mare Regions of the Lunar Surface

In this chapter, there is an investigate how well an automatic CDA is suitable to determine the surface age of different lunar regions. A template-based CDA is used to analyze image data under known illumination conditions. For this purpose, artificially illuminated crater templates are used to detect and count craters and their diameters in the areas under investigation. The automatic detection results are used to obtain the (CSFD) for the examined areas, which is then used for estimating the absolute model age (AMA) of the surface. The main focus of this work is to find out whether there exists an ideal sensitivity value for automatic crater detection to obtain smallest possible errors between the automatically derived AMA and a reference AMA derived from manually detected craters. The detection sensitivity threshold of the (CDA) is calibrated based on five different regions in Mare Cognitum on the Moon such that the age inferred from the manual crater counts corresponds to the age inferred from the CDA results. The obtained best detection threshold value is used to apply the CDA algorithm to another five regions in the lunar Oceanus Procellarum region. The accuracy of the method is examined by comparing the calculated AMAs with the manually determined ones from the literature. It is shown that the automatic age estimation yields AMA values that are generally consistent with the reference values with respect to the one standard deviation errors.

This chapter has been adapted and/or adopted from: (Salih et al, 2017b).

4.1 Mare Cognitum and Oceanus Procellarum Introduction

In order to obtain information about the geologic history of a planet, e.g. to learn about its formation or about volcanic or other geologic processes, it is important to analyze its surface age. This helps to understand the transformation of the planetary surface over time. In order to estimate the age of planetary surfaces, it is possible to analyze rock samples collected by manned space missions or acquire images of the planetary surface

through unmanned spacecraft. By calculating the impact (CSFD) on such images, it is possible to deduce the absolute age of the surface by relating the CSFD to the age obtained by laboratory analyses of returned samples (Neukum et al., 2001).

The age of a planetary surface is of major importance for its subdivision into different geological units and the analysis of geological processes. There exists a well-established statistical approach for the estimation of the surface age that relies on CSFD (e.g., Neukum et al., 2001). Absolute ages of planetary surfaces can be determined by means of radiometric methods, which, however, require the acquisition and possibly also the return of surface samples. In contrast, the most practical methods for age estimation are those that do not involve sampling of the surface. They rely on the general observation that the amount of craters increases with the time that has passed since the surface has been deposited. The extracted information regarding the cratering rate per area may be directly used to derive the relative age of different planetary surface areas. The main advantage of the crater-based methods is that the required information may be extracted from images and or digital elevation models (DEM). The information is thus extracted only from remotely obtained data of the surface.

In order to derive absolute model ages (AMA) of the surface, the methods are combined, i.e., the CSFD of areas for which samples are available is determined and then calibrated with respect to the absolute age of the sample. This calibration allows for the estimation of absolute ages of individual areas on the Moon (e.g., Neukum et al., 2001). The advantage of performing this procedure by applying an automatic (CDA) is to reduce the amount of time needed to calculate the AMAs for large areas on planetary surfaces (Salamunićcar and Lončarić, 2010).

Usually, the estimation of the CSFD is done by manual CSFD measurements and size determination in the available planetary images. Since the AMA highly depends on the CSFD, it is very important to detect all craters and not include false detections into the CSFD. Although this manual process is highly demanding and time consuming for large areas, it is commonly still preferred over automatic CDA, which often misses some craters and/or falsely detects craters. The automatic detection algorithms, however, operate comparably fast and may thus be easily applied to large high-resolution global image mosaics of various planetary surfaces. Plenty of automated methods for crater

detection based on image data or topographic data have been developed recently (e.g., Salamunićcar and Lončarić, 2008, 2010; Stepinski et al., 2012).

Since the AMA is derived from the CSFD using a statistical approach, this work is focused on the analysis of the feasibility of AMA estimation based on an automatic CDA. However, the AMA to be robust with respect to small fluctuations is expected, e.g., false detections or missing detections, in the estimated CSFD. Consequently, this work aims at the estimation of the accuracy of a CDA with respect to the AMA and not with respect to the true and false detections. The latter tends to be difficult to obtain anyway due to an inherent uncertainty of the required manually determined "ground truth", because significant variations between manual crater counts of the same area by different persons, even when performed by experts, may occur (Robbins et al., 2014).

4.2 Template Matching and Automatic Crater Detection

The determination of the CSFD is the main approach to estimate the AMA for various individual geologic regions on the Moon (Neukum et al., 2001). The CSFD from a mosaic of Wide Angle Camera (WAC) images of the Lunar Reconnaissance Orbiter Camera (LROC) (Robinson et al., 2010; Wagner et al., 2016) has been derived. The spatial resolution of the mosaic is about 100 m per pixel. The assumption applied that the craters can be detected if their diameter equals or exceeds 300 m (3 pixels in the image).

In order to be able to detect craters using the template matching method, the method has been explained in the Chapter Three and created by Grumpe and Wöhler (2013) and use their six artificially generated 3D crater templates.

According to previous studies, the volcanic activity on the Moon has been high in the period of time between 1.2 to 4 billion (Ga) years ago (Hiesinger et al., 2003). These activities and eruptions formed a large variety of lunar mare basalt units in different areas. Figure 4.1 shows the primary mare areas on the lunar nearside. For the study of lunar volcanic processes, it is very important to know the temporal sequence of individual volcanic activities and how they affect the extents of the corresponding basalt areas.

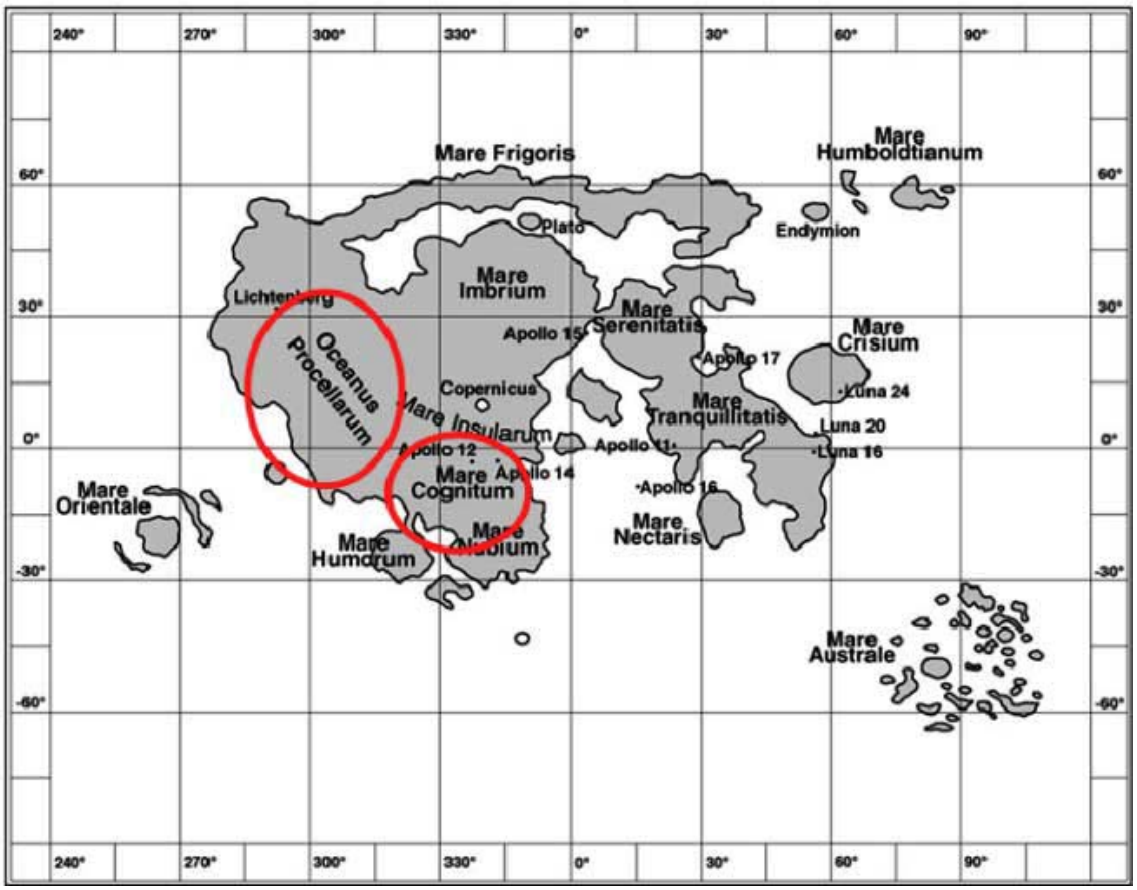

Figure 4.1: Mare regions on the lunar nearside; credit: (Hiesinger et al., 2003)

Basically, the AMA estimation process is based on the CSFD which represents the number of craters per diameter interval per unit area. The sensitivity of the applied CDA is controlled by a sensitivity threshold value. This value needs to be adjusted according to the AMA of a reference area obtained manual crater counts. The obtained AMA should be the same as the manually determined AMA. The detected craters allow for constructing the CSFD, represented by a cumulative histogram defined by diameter bins. The user-defined diameter range depends on the image resolution, the crater types and sizes and the craters density per surface area. The so-called production function as e.g. given in Neukum et al. (2001) is then fitted to the cumulative histogram. It yields the number of craters smaller than a given diameter value per unit area. Then the value $N(dr)$ of the production function for a reference diameter dr, where typically $dr = 1$ km, is determined (Neukum et al., 2001). A second important function, the chronology function, describes the number $N(1)$ of craters less than 1 km diameter per unit area independence of the AMA. Hence, the AMA can be obtained by inversion of the chronology function (Neukum et al., 2001). Details about the method of CSFD-based

AMA estimation are given e.g. in Neukum et al. (2001). Typically, determination of the CSFD is performed based on orbital imagery.

4.3 Areas of Implementation

The determined crater positions and diameters are then used to derive the CSFD for the study region. This study focuses on the five areas C1-C5 defined in Hiesinger et al. (2003) located in Mare Cognitum and another five areas P5, P41, P49, P50, and P51 defined in Hiesinger et al. (2003) located in Oceanus Procellarum. All these ten study areas are located in a latitude range between 15° S and 30° N and in a longitude range between 285° E and 345° E. Figure 4.2 (a-e) shows the obtained craters for the five study areas C1-C5 located in Mare Cognitum by applying the described template matching based CDA. The sensitivity threshold of the template matching is adapted such that the squared difference between the AMA inferred for C1-C5 and the AMA given in Hiesinger et al. (2003) is minimized.

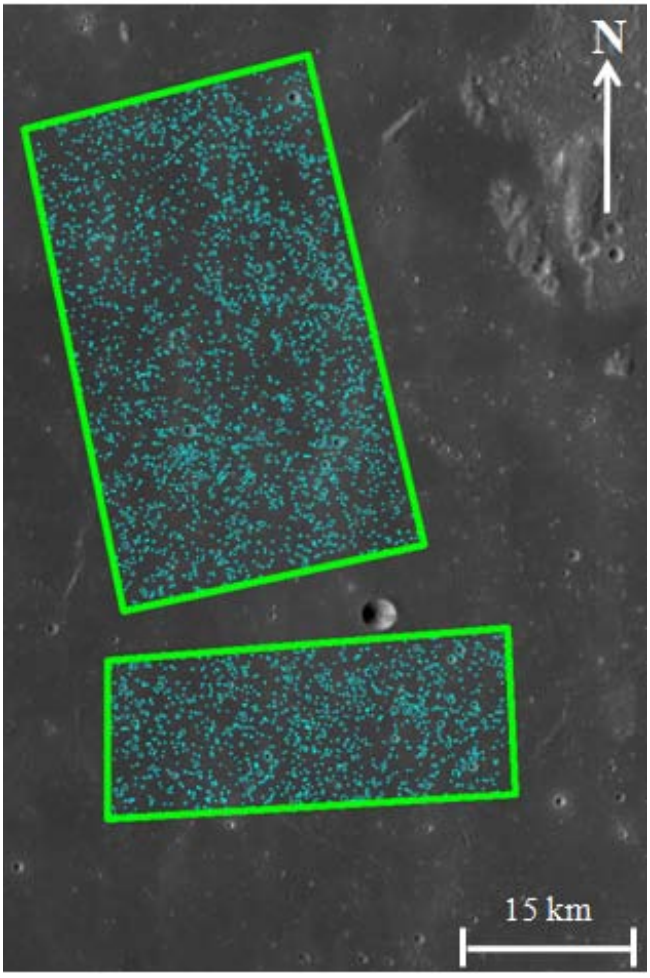

(a) Area C1

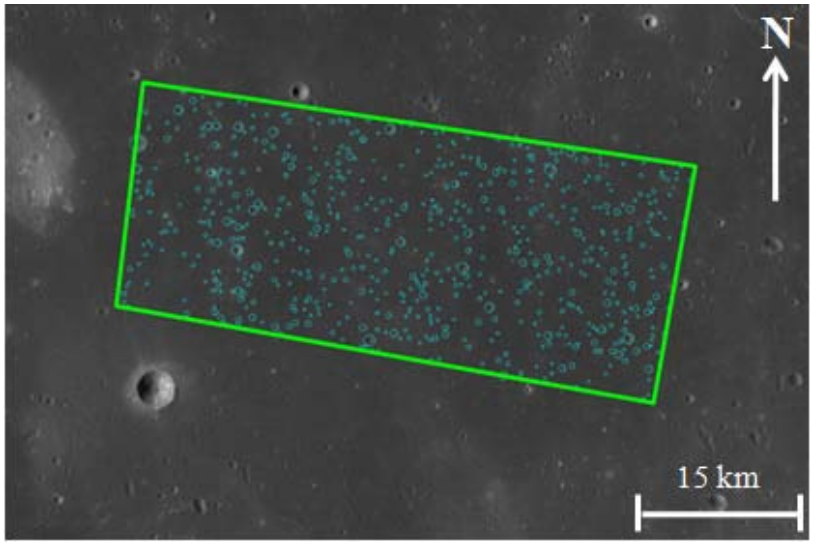

(b) Area C2

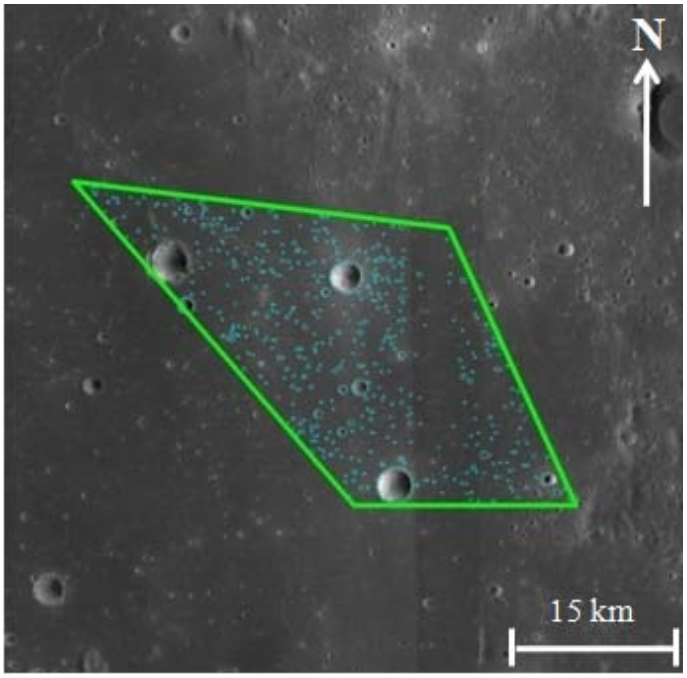

(c) Area C3

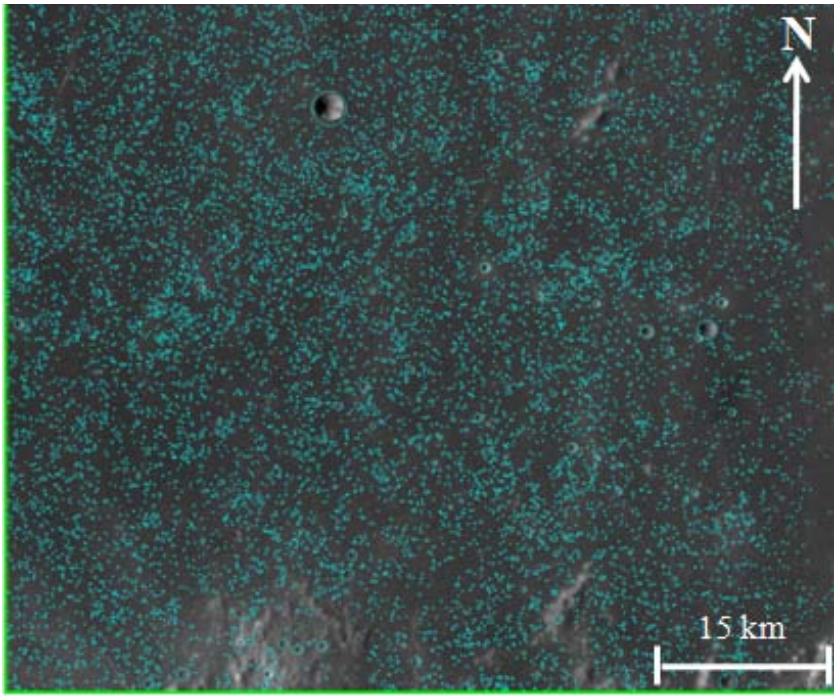

(d) Area C4

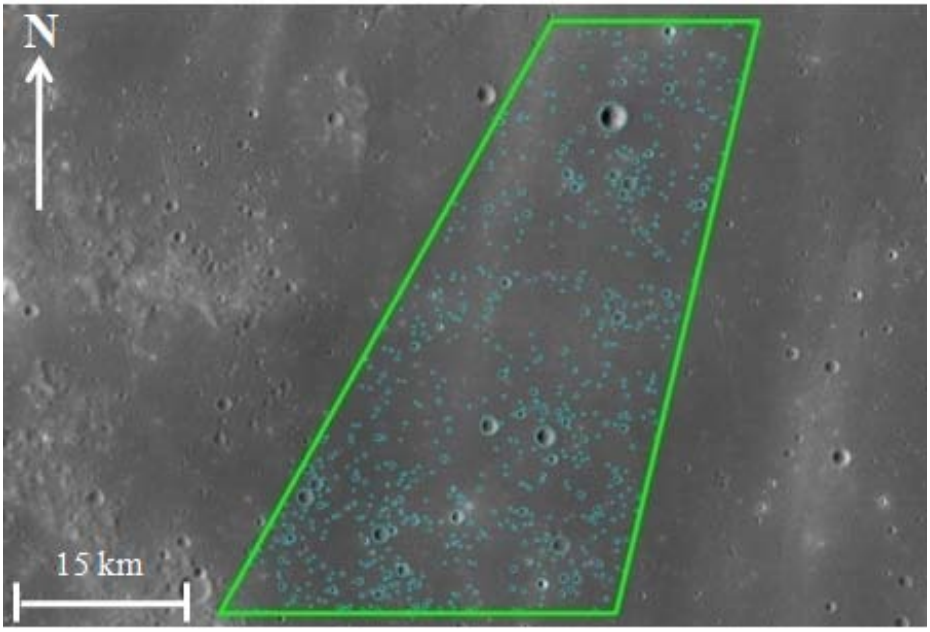

(e) Area C5

Figure 4.2: Craters detected in the counting areas by the template matching based CDA in areas C1-C5. The green polygons denote the counting areas.

Figure 4.3 (a-e) shows the detected craters for the other five study areas P4, P41, P49, P50 and P51 located in Oceanus Procellarum by applying the described template matching based CDA with respect to the optimal threshold obtained for the Mare Cognitum test areas.

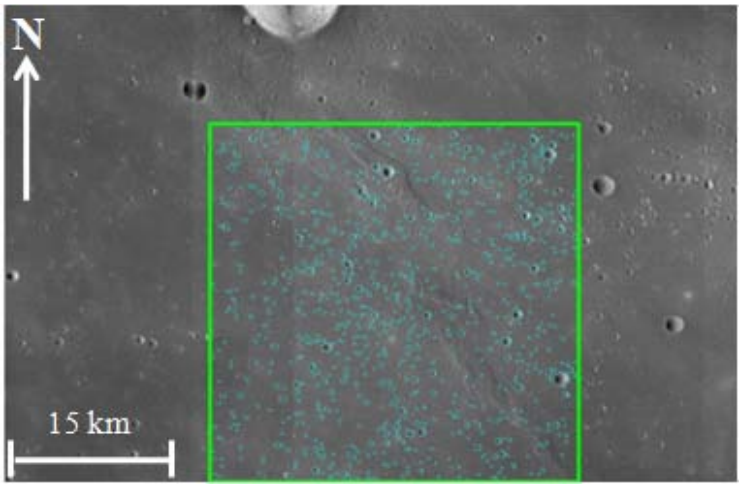

(a) Area P5

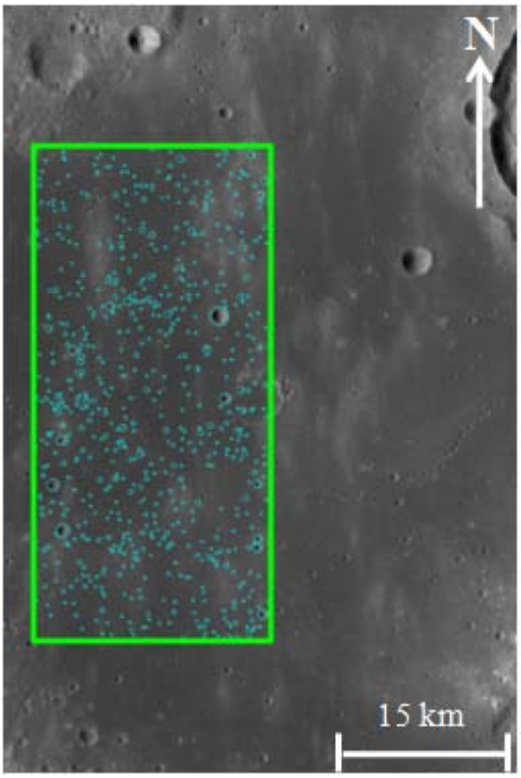

(b) Area P41

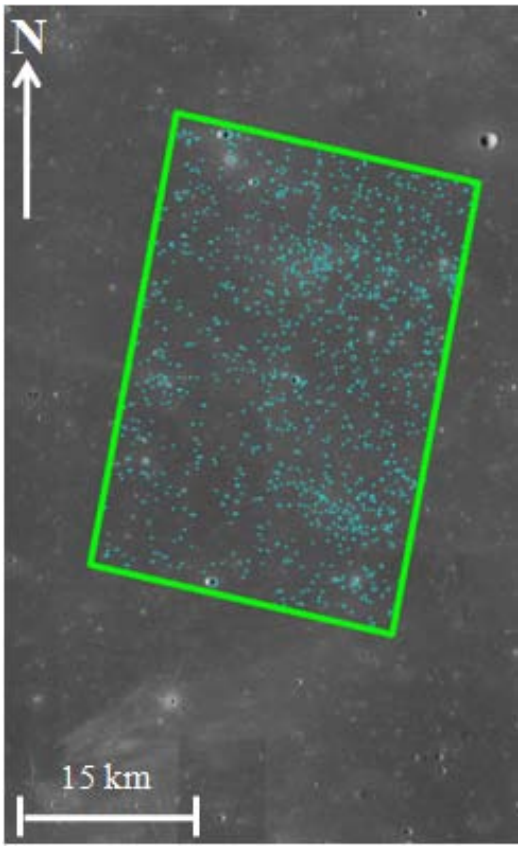

(c) Area P49

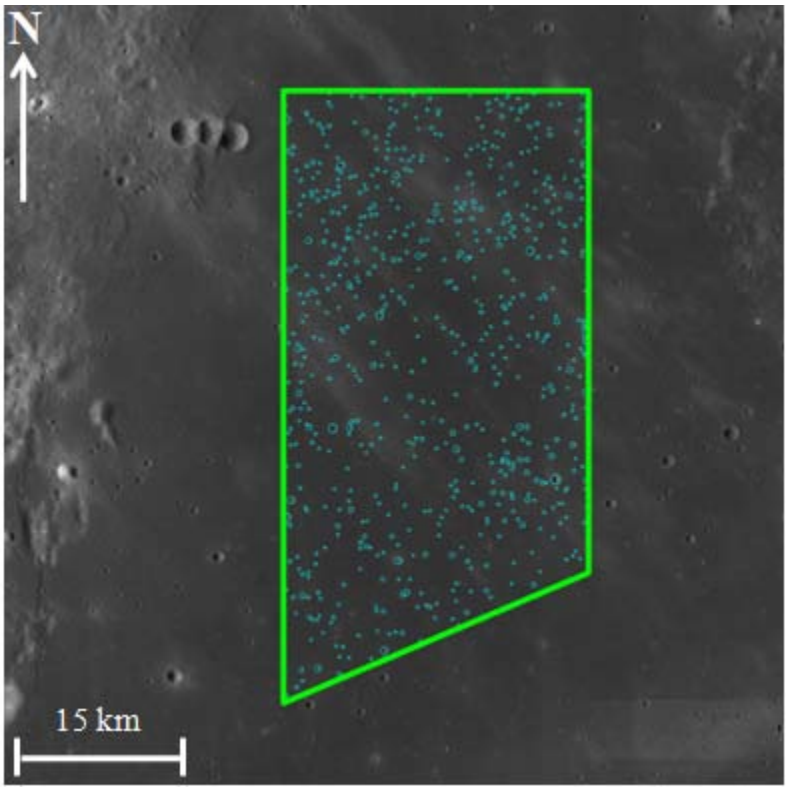

(d) Area P50

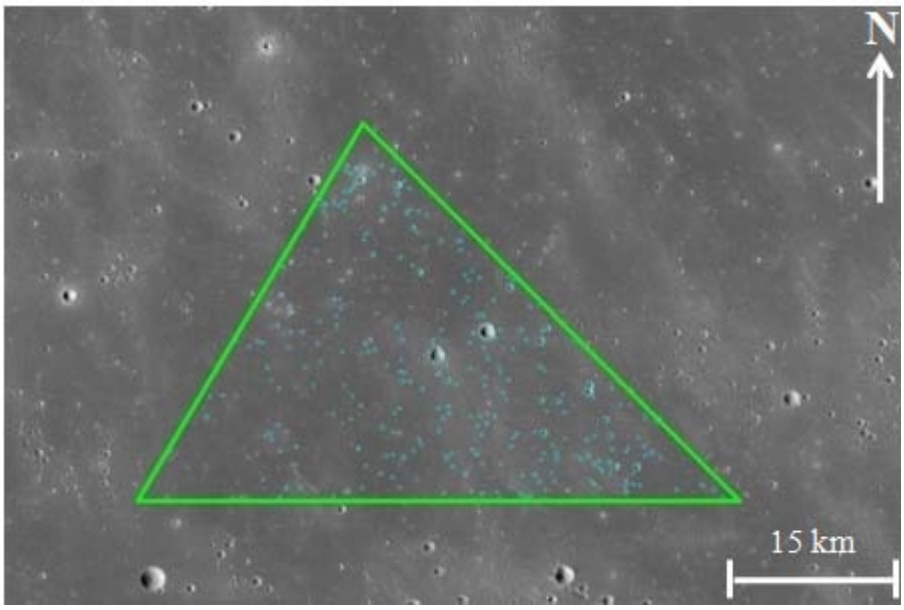

(e) Area P51

Figure 4.3: Craters detected in the counting areas by the template matching based CDA in Oceanus Procellarum areas. The green polygons denote the counting areas.

4.4 Results and Discussion

Firstly, the optimal cross-correlation thresholds for the regions C1-C5 were calculated automatically by comparing the CDA-based AMAs with the referenced AMAs from Hiesinger et al. (2003). All obtained threshold values are shown in Table 4.1.

Table 4.1: Calibrated Detection Threshold Values for the Individual Regions C1-C5 in Mare Cognitum.

Area	Calibrated Threshold
C1	**0.6637**
C2	**0.6455**
C3	**0.6541**
C4	**0.6677**
C5	**0.6648**
Average Value	**0.6592**

The arithmetic mean of the five calibrated detection thresholds amounts to 0.6592. Area C1 consists of two polygons for the CSFD measurements. The other investigated areas have always been defined by a single polygonal shape. By applying this “optimal” threshold value to the areas C1-C5 in Mare Cognitum yields the AMAs listed in Table

4.2, where they are compared to the reference AMAs from Hiesinger et al. (2003) obtained based on manual crater counts. For area C5, two reference AMAs are given, which are interpreted as the result of a resurfacing process by Hiesinger et al. (2003).

Table 4.2: CDA-Based and Reference AMAs for the Study Areas in Mare Cognitum after Applying the Optimal Detection Threshold

Area	CDA-based AMA [Ga]			Reference AMA [Ga] (Hiesinger et al., 2003)		
C1	**3.52**	**-0.008**	**+0.007**	**3.49**	**-0.10**	**+0.08**
C2	**3.46**	**-0.004**	**+0.004**	**3.45**	**-0.06**	**+0.09**
C3	**3.63**	**-0.024**	**-0.018**	**3.41**	**-0.08**	**+0.08**
C4	**3.43**	**-0.002**	**-0.002**	**3.36**	**-0.11**	**+0.10**
C5	**3.52**	**-0.006**	**-0.006**	**3.32** **3.65**	**-0.14** **-0.08**	**+0.10** **+0.08**

The CDA faces difficulties if the illumination direction is different in different image parts, as in area C3. Since the target image is a mosaic, this might occur if images acquired under different illumination conditions are combined. The western half of the image (left of the yellow dividing line) is illuminated from the east while the eastern half is illuminated from the western side as shown in Figure 4.4. This causes the illumination vector to be erroneously calculated since the applied algorithm assumes that the images are homogeneously illuminated from one direction, and therefore the illumination angle is found which provides the best match between image and shaded GLD100 on the average.

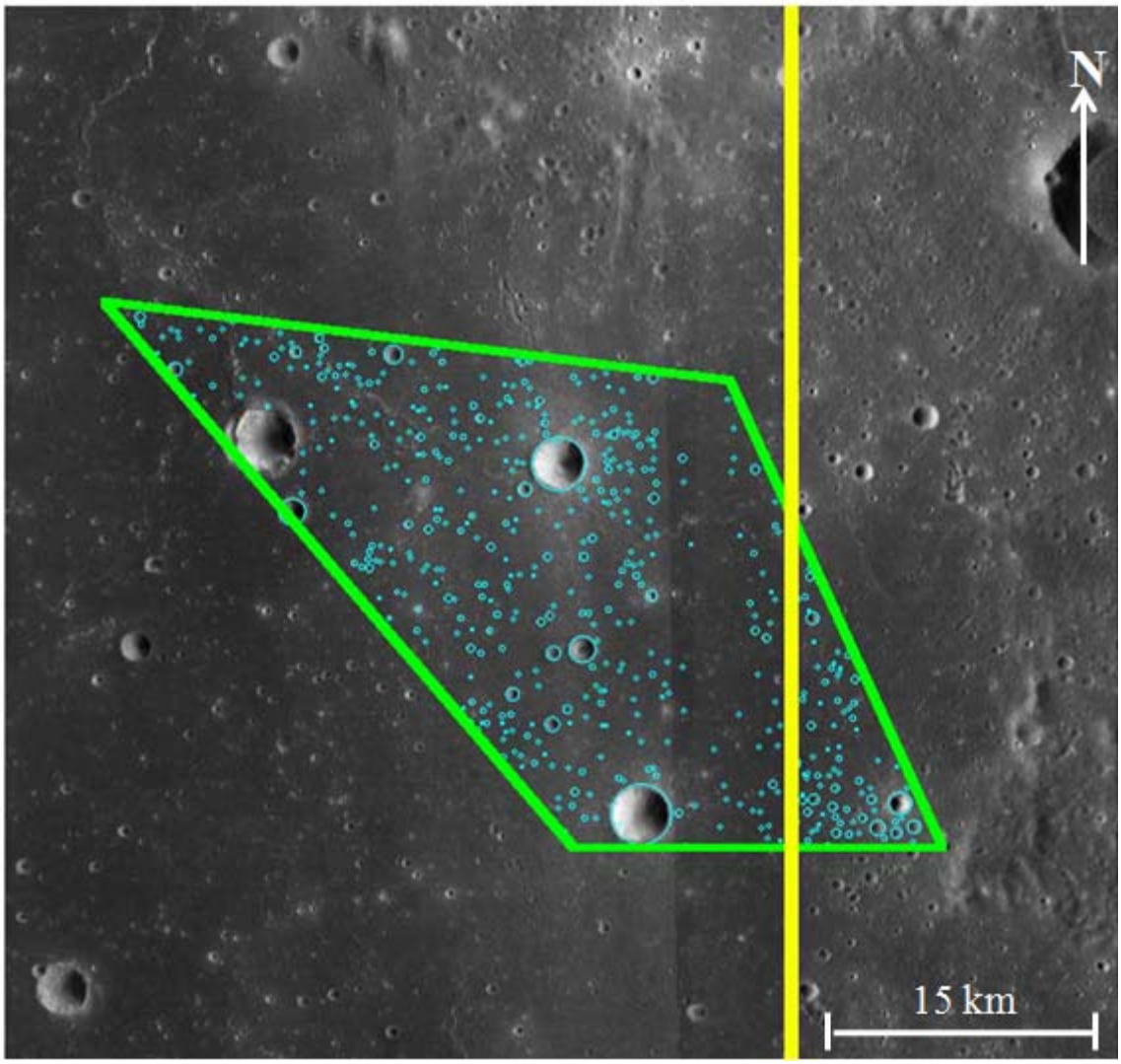

Figure 4.4: Crater detections in area C3. The green polygon denotes the study area and the yellow line separates the two different illumination directions.

When illuminating the 3D crater models accordingly, many craters in the study area were not recognized. It is thus necessary to manually check for the actual illumination and whether the estimated illumination vector is correct or, if necessary, only a part of the image is used for the calculation of the illumination direction.

In the next step, the study areas in Oceanus Procellarum are again delineated by polygons. The optimal threshold value from Table 4.1 was applied to the areas P5, P41, P49, P50, and P51 in Oceanus Procellarum as defined by Hiesinger et al. (2003), resulting in the AMAs listed in Table 4.3. It can be seen that all except one (P41) of the CDA-derived AMAs are very close to the manually based reference AMAs from Hiesinger et al. (2003).

Table 4.3: CDA-Based and Reference AMAs for the Study Areas in Oceanus Procellarum, Obtained Using the Optimal Detection Threshold Inferred From Areas C1-C5

Area	CDA-based AMA [Ga]			Reference AMA [Ga] (Hiesinger et al., 2003)		
P49	**1.71**	**-0.140**	**+0.110**	**2.01**	**-0.43**	**+0.37**
P5	**3.45**	**-0.019**	**+0.015**	**3.48**	**-0.06**	**+0.08**
P41	**3.33**	**-0.009**	**-0.009**	**2.13**	**-0.85**	**+0.75**
P50	**1.90**	**-0.166**	**-0.128**	**1.87**	**-0.25**	**+0.56**
P51	**2.01**	**-0.205**	**-0.166**	**1.85**	**-0.34**	**+0.37**

It can be seen that all CDA-derived AMAs are very close to the manually manual crater count based reference AMAs from Hiesinger et al. (2003). Similar to the region C3, an illumination change occurs in region P5 as shown in Figure 4.5. This was because the area is also not homogeneously illuminated. It is clear that at the left side of the image, there is a strip of craters (between the completely black crater and the big one in the picture above) was illuminated from the right when shooting, but the remaining areas were illuminated from the left side. In this case, a lighting vector was calculated that illuminated the craters from the north. As a result, very few craters cannot be detected in this area. The estimated AMA, however, does not differ much from the AMA given in Hiesinger et al. (2003).

The largest deviations between CDA-based and reference AMAs occurs for region P41 with a reference AMAs of 2.13 Ga of about 1.2 Ga, due to the nearly horizontal chronology function for AMAs between about 2 and 3 Ga (Neukum et al., 2001), ages in this range are particularly sensitive to changes in the *N(1)*, and a small number of falsely detected or missed craters can make a large difference in AMA. Hence, this area P41 has relatively large errors of the reference AMA value in Table 4.3. Despite the similarly large AMA estimation errors, the inferred AMAs of the regions P50 and P51 are in good agreement with the AMAs given by Hiesinger et al. (2003). This implies that the AMA estimation is less sensitive to small errors for younger surfaces.

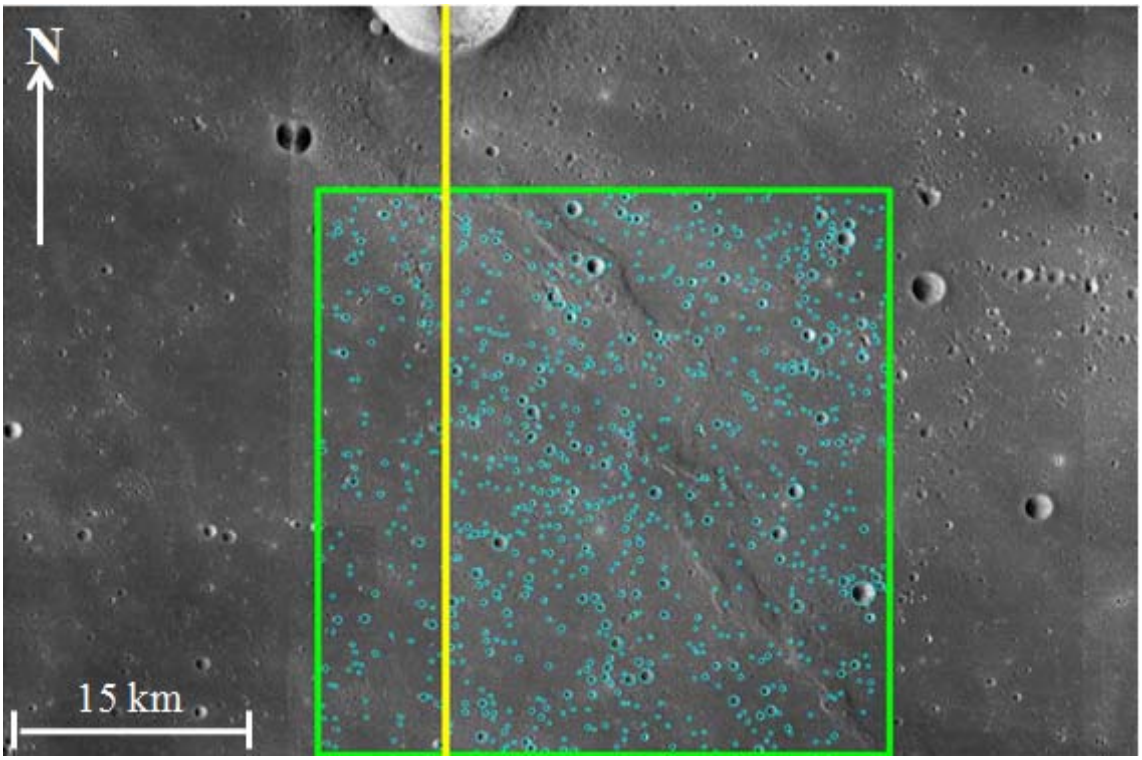

Figure 4.5: Crater detections in area P5. The green polygon denotes the study area.

For all study regions except area P41, the deviations of the CDA-based AMA and the manual count based AMA are within the statistical error intervals. For AMAs between (2 and 3 Ga), the production function is almost horizontal (Neukum et al., 2001), such that a small number of falsely detected or missed craters can make a large difference in AMA, hence ages in this range need to be interpreted with care.

Chapter 5

Validation with Large Craters: Catalogue LU78287GT

CSFDs are an important tool for the assessment of the ages of surface regions (Neukum, 1983; Michael and Neukum, 2010). The freely available software Craterstats2 by Michael (2014) allows for the determination of the absolute model ages (AMA) of the surface if the number and diameters of the craters within the count area of a certain size are known. In this context, manual counting and measuring of craters is a time-consuming process while automatic crater detection may lead to increased false positive detections, missed craters and possibly inaccurate diameter determination. However, the influence of such recognition errors of automated crater detection systems on the estimated model age has not yet been fully investigated. Current automatic CDAs depend on either optical images or digital elevation models (DEM) (Salamuniccar and Lončaric, 2010). In this chapter, a comparison of different crater detectors and their behavior in the context of surface age determination will be presented.

This chapter has been adapted and/or adopted from: (Salih et al., 2014; Boukercha et al., 2014).

5.1 Steps of Implementation

The lunar crater catalogue LU78287GT presented by Salamuniccar et al. (2014) contains a list of manually verified craters detected with the algorithm described in Salamunićcar and Lončarić (2010) and Salamuniccar et al. (2014). The photometric surface refinement method in Grumpe et al. (2014) and the DEM-based detector described in Salamunićcar and Lončarić (2010) and extended in Salamuniccar et al. (2014) to detect possible craters have been applied respectively. Additionally, the intensity image based detector constructed in Grumpe and Wöhler (2013) and described in details (See Chapter 3) is applied to the image to derive a different set of automatically detected craters. The generated crater templates are then scaled to a given diameter range of 0.3-20 km and the normalized cross-correlation with the image is computed, respectively, where local maxima of the normalized cross-correlation are set to be crater candidates. Based on a specified threshold value, the determined cross-

correlation value indicates whether the detected candidate is a crater or not. Finally, the two-stage method by Boukercha et al. (2014) is applied to obtain a third set of craters.

Based on the LU78287GT catalogue, a reference model age is determined for a calibration region, and the detection thresholds of the automatic methods are adapted such that their estimated model ages are as similar as possible to that of the reference model age for all three methods. Afterward, all crater detection methods are applied to a different region of interest, and the corresponding surface ages are derived and compared.

The LU78287GT catalogue contains the craters visible in a part of Moon Mineralogy Mapper (M^3) image M3G20090205T193313. From this large area, parts of the floors of the large impact craters Ptolemaeus and Alphonsus were extracted, where the floor of Ptolemaeus serves as the calibration region and the floor of Alphonsus as the region of interest, whose model age is estimated using the different automatic crater detection approaches. In these two regions, the surface is illuminated at incidence angles between about 52° and 53°.

The main goal of this work is to present and apply the newly created MATLAB function for surface age estimation and its flexibility with different groups of craters datasets. These craters datasets are possibly different in the total distance, a number of craters, the craters diameters sizes, and the angle of illumination. The group tested is the LU78287GT dataset from the Moon Mineralogy Mapper (M^3) image M3G20090205T193313 which can be considered as being equivalent to a wide-angle camera (WAC) result.

Two large craters (Ptolemaeus and Alphonsus) which they carry quite a suitable number of craters candidates that have been chosen for the calibration and evaluation stages. CDAs are implemented for the datasets with a DEM-based detector as a first step and followed by a second detector of the Image-based detection process. The range of craters candidates diameters in this first part of implementation is between (0.7-2.5 Km) with apparently large distance. An Age value has been calculated for each of Ptolemaeus and Alphonsus craters that can be used for comparison, calibration, and evaluation.

For a high confidence for the age estimation system, an optimization process for the results is processed to provide re-fine threshold values that resulted in a more precise estimated age.

5.2 The LU78287GT

Building age estimation system for surfaces is quite a challenging task and at the same time is a great goal from the engineering view that can give different comparable results with the geologist data. An age estimation program for surfaces has been built based on the available craterstat software information and translating this information into mathematic code that produces quite very encouraging results.

Salamuniccar et al. (2014) introduced a hybrid CDA that follows several steps:

- Image-based reconstruction of topographic data using a shape from shading technique.
- Application of the DEM-based CDA
- Contrast normalization of the images used in order to extract crater rims more precisely.

Due to the topographic data, which were refined in comparison to previous works, in Salamuniccar et al (2014), the number of craters increased considerably from the previous LU60645GT catalogue to the new LU78287GT catalogue Salamuniccar et al. (2014). The LU78287GT produced by Salamuniccar et al. (2014) is considered to be the ground-truth reference catalogue in this work as a first step of applying the newly developed age estimation procedure.

However, we apply the CDA explained in Salamuniccar et al. (2014) as a first detection step. For a given data image, a photoclinometry-based DEM reconstruction refines the existing DEM and an edge-detection process applied, and then a fuzzy radon-hough based detector produces our own candidates (Salamuniccar and Loncaric, 2010), which resulted in the detection of new un-cataloged impact craters. Probability estimation from these resulted in candidates created to distinguish whether these candidates are craters or non-craters. It is possible to use any of the practical classifier types ranged from support vector machines to complex classifiers (Schürmann, 1996, Bishop, 2006).

Consequently, a generative template-based approach has been applied to certain regions in spacecraft images (the LU78287GT catalogue) that include different sizes of craters (most of them less than 10 km). This generative template-based approach consists of six generated templates based on the directions towards the Sun and the viewer (See Chapter 3).

Then, this crater detection algorithm has been applied as a detection stage on the craters appearing in the Moon Mineralogy Mapper (M^3) image M3G20090205T193313 (Pieters et al., 2009). And according to LU78287GT, a crater candidate is labeled as a crater under the condition of fewer than three pixels away from the center value given in the catalogue. Figure 5.1 shows all the resulting candidates mapped onto the images. The candidate set is separated into craters and non-craters forms, and a disjoint process into subsets and a10-fold cross-validation for the error checking purpose is implemented for sufficient training (Marsland, 2009).

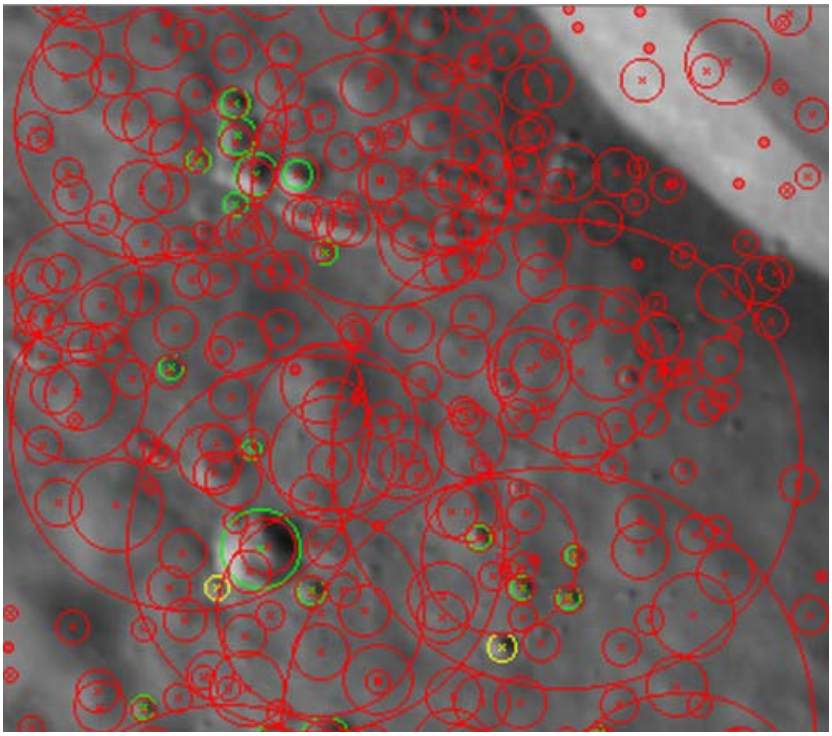

Figure 5.1: Crater candidates obtained by Salamuniccar's detector in (Salamunićcar et al., 2014). False positives are given in red color; the color green represents the candidates that are closer than 3 pixels to the LU78287GT catalogue craters and the color yellow represents candidates that exactly correspond to craters from the LU78287GT.

5.3 Study Regions Alphonsus and Ptolemaeus

The referenced lunar crater catalogue LU78287GT contains a list of craters detected manually with the described algorithm in Salamuniccar and Loncaric (2010); and Salamuniccar et al. (2013). The photometric surface refinement method explained in Salamuniccar et al. (2013), and the DEM-based detector described in Salamuniccar and Loncaric (2010) with extended steps in order to detect more reliable precise craters have been all implemented. In addition to that, and as an important further step, an intensity image-based detector described in Grumpe and Wöhler (2013) is also applied to the image to create a new different set of automatically detected craters.

According to the LU78287GT catalogue, two reference models for age estimation have been generated for a full calibration process for the whole image region. There is a mutual process of calibration between these two regions Alphonsus and Ptolemaeus as considering one region for calibration and the other as a region of interest and vise verse (Figure 5.2). A new MATLAB code has been created for the age estimation purpose that is based on the available literature (Michael, 2013; Michael, 2014).

Parts of the floors (colored rectangles shown in Figure 5.2) of the large impact craters Ptolemaeus and Alphonsus were extracted, where the floor of Ptolemaeus serves as the calibration region and the floor of Alphonsus as the region of interest (Salih et al., 2014).

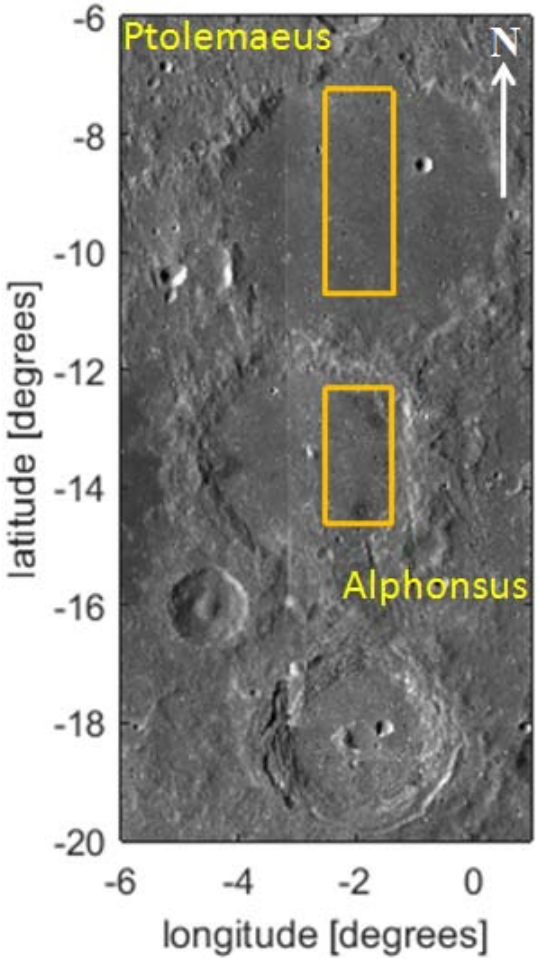

Figure 5.2: Ptolemaeus and Alphonsus craters excerpt from LROC WAC mosaic (Speyerer et al., 2011)

This first surface area consists of a floor of large impact crater called Ptolemaeus. The Ptolemaeus calibration region contains visible craters in a part of Moon Mineralogy Mapper (M^3) image M3G20090205T193313 with a covered distance of about 2437 km^2. During each processing step, detection thresholds values of the automatic methods are adapted so that the same estimated model ages values as for the reference (LU78287GT catalogue) model age for all of three explained steps are obtained.

Afterward, all the above crater detection methods are applied to the second region of interest, which is another large impact crater called Alphonsus with a covered area of 1566 km^2 as a comparison step process. The corresponding surface ages are derived by implementing the suitable optimized detection thresholds values extracted from the Ptolemaeus calibration region through the new MATLAB code for age estimation. The

craters detected with the different methods are shown in Figures (5.3 and 5.4) (Salih et al., 2014).

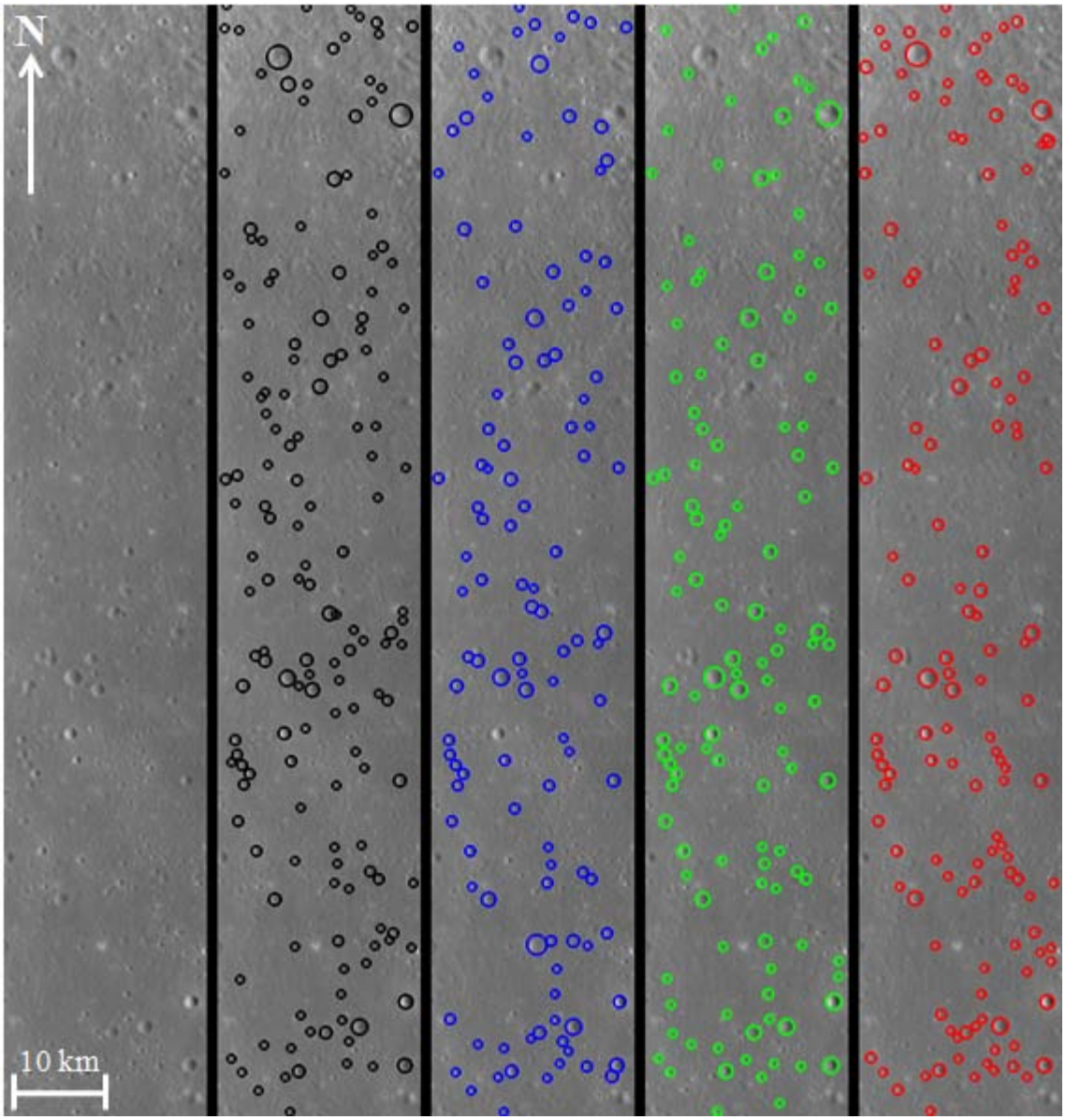

Figure 5.3: Detected craters within Ptolemaeus Crater. Black: LU78287GT (Salamuniccar et al., 2014). Blue: DEM-based detector (Salamunićcar and Lončarić, 2010; Salamuniccar et al., 2014). Green: image-based detector (Grumpe and Wöhler; 2013). Red: two-stage method (Boukercha et al., 2014).

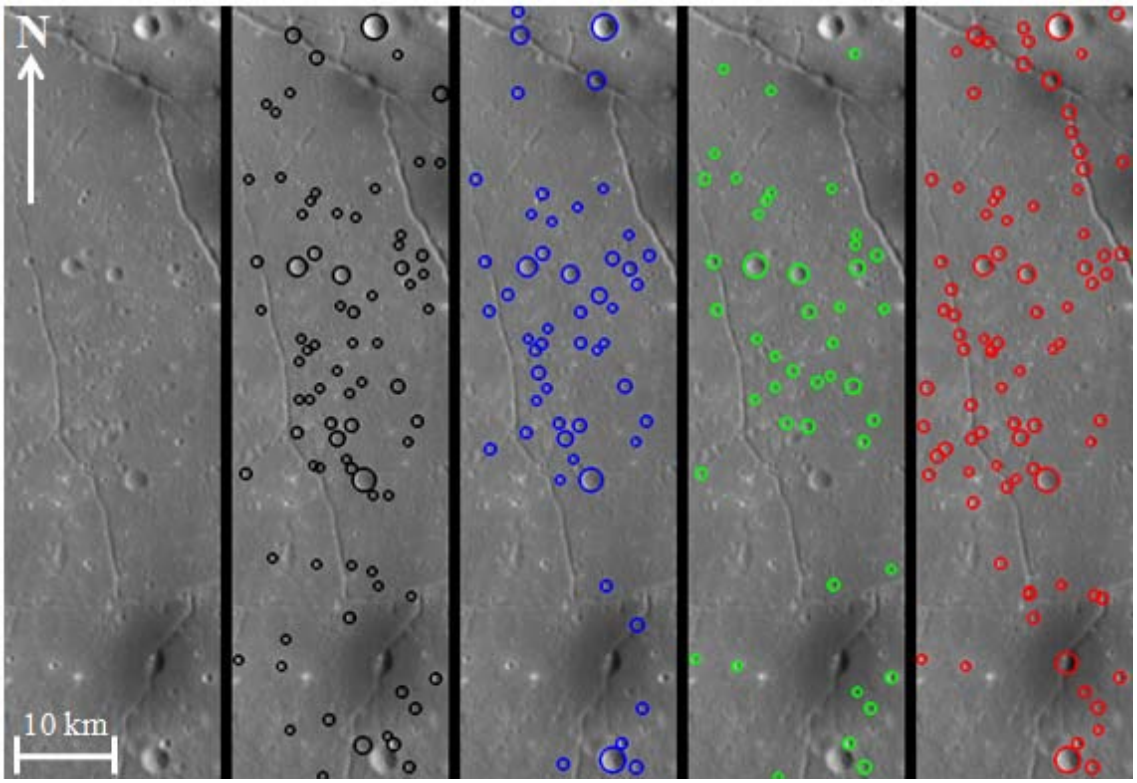

Figure 5.4: Detected craters within Alphonsus crater. Black: LU78287GT (Salamuniccar et al., 2014). Blue: DEM-based detector (Salamunićcar and Lončarić, 2010; Salamuniccar et al., 2014). Green: image-based detector (Grumpe and Wöhler; 2013). Red: two-stage method (Boukercha et al., 2014).

The age estimates of the three automatic crater detection approaches adjusted to those obtained for the ground truth catalogue are shown for the calibration area on the floor of Ptolemaeus crater in Figure 5.5. As intended for calibration, all four model ages are identical. The isochrons were fitted to the crater diameter interval 0.7–2.5 km.

The detection thresholds obtained by the calibration procedure were retained when applying the automatic detection methods to the region on the floor of Alphonsus crater (Figure 5.4). The estimated model ages inferred from the automatic detection results are between 3.69 and 3.82 Ga, which compares well with the model age of 3.76 Ga obtained based on the LU78287GT catalogue (Figure 5.6).

The results show that the estimation of surface ages based on automatic crater detection may yield realistic results when an appropriate calibration procedure is applied (Salih et al., 2014).

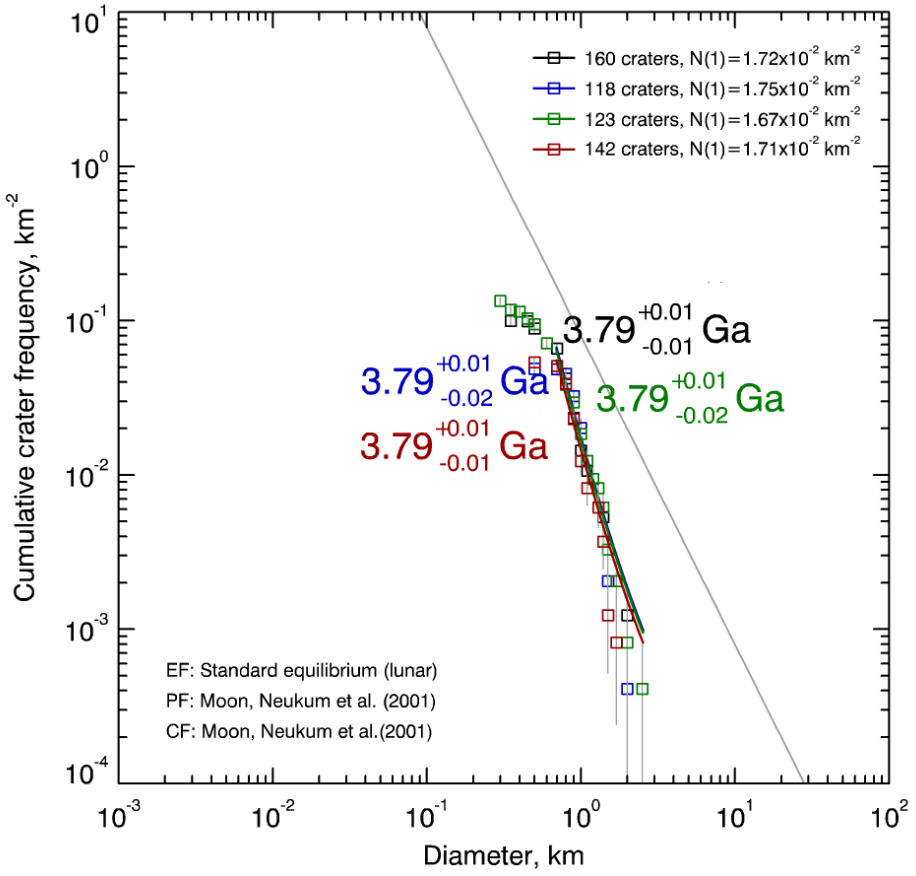

Figure 5.5: Derived model ages for the region of interest on the floor of Ptolemaeus Crater. Black: LU78287GT (Salamuniccar et al., 2014). Blue: a DEM-based detector (Salamunićcar and Lončarić, 2010; Salamuniccar et al., 2014). Green: an image-based detector (Grumpe and Wöhler; 2013). Red: two-stage method (Boukercha et al., 2014).

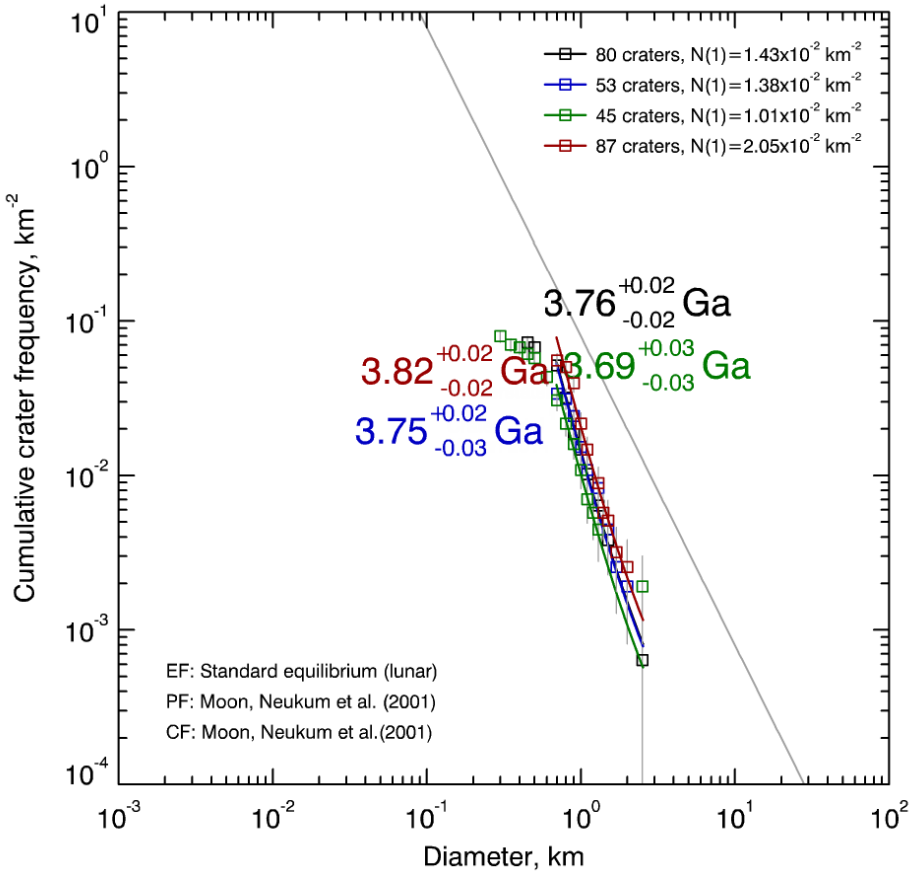

Figure 5.6: Derived model ages for the region of interest on the floor of Alphonsus crater. Black: LU78287GT (Salamuniccar et al., 2014). Blue: a DEM-based detector (Salamunićcar and Lončarić, 2010; Salamuniccar et al., 2014). Green: an image-based detector (Grumpe and Wöhler; 2013). Red: two-stage method (Boukercha et al., 2014).

5.4 Results and Discussion of Alphonsus and Ptolemaeus

The results as shown down in Table 5.1 are reasonable and reliable where all the resulted values within a good range of trust and confidence. There is a small deviation in the age values of the calibration region due to the mathematic absolute calculation of the false positives effect. The best threshold value that controls the calibration process is (0.245) for the DEM-based detector, and (0.765) for the template matching detector.

This process has been implemented again in the opposite way as considering the Alphonsus crater as a Calibration crater area while the Ptolemaeus crater as an area of interest. This is done by extracting the optimized threshold values from the calibration region to implement them on the area of interest. The corresponding surface age values are shown down in Table 5.2. The age value deviation in occurred here only in the image-based detector stage due to the high number of the false positives candidates and

the mathematic absolute calculation. The best threshold value that controls the calibration process is (0.260) for the Dem-based detector, and (0.610) for the template matching detector.

Table 5.1: Ptolemaeus Crater as a Calibration Area and Alphonsus as an Area of Interest

Area / Algorithm	Ptolemaeus (Number of Craters)	Alphonsus (Number of Craters)
LU78287GT catalogue (Reference value)	3.75 +0.015 -0.022 Ga (160)	3.78 +0.011 -0.013 Ga (81)
DEM-based detector	3.76 +0.015 -0.022 Ga (146)	3.79 +0.010 -0.012 Ga (70)
Image-based detector	3.76 +0.015 -0.021 Ga (149)	3.68 +0.040 -0.040 Ga (62)

Table 5.2: Alphonsus Crater as a Calibration Area and Ptolemaeus as an Area of Interest

Area / Algorithm	Alphonsus (Number of Craters)	Ptolemaeus (Number of Craters)
LU78287GT catalogue (Reference value)	3.78 +0.011 -0.013 Ga (81)	3.75 +0.015 -0.022 Ga (160)
DEM-based detector	3.78 +0.010 -0.012 Ga (63)	3.71+0.035 -0.035 Ga (135)
Image-based detector	3.82 +0.011 -0.016 Ga (218)	3.86 +0.004 -0.005 Ga (366)

For a refine age estimation process for each of the above regions (Alphonsus and Ptolemaeus), the polynomial fitting process of the fifth degree has been applied to the resulted data. A new close estimated age obtained according to the appropriate input threshold values to the MATLAB function as shown in Figures (5.7-5.8) for Ptolemaeus Crater. The Age obtained for the Ptolemaeus craters dataset after the DEM-based detector process is (3.756 Ga), and after the Image-Based detector, the stage is also (3.756 Ga).

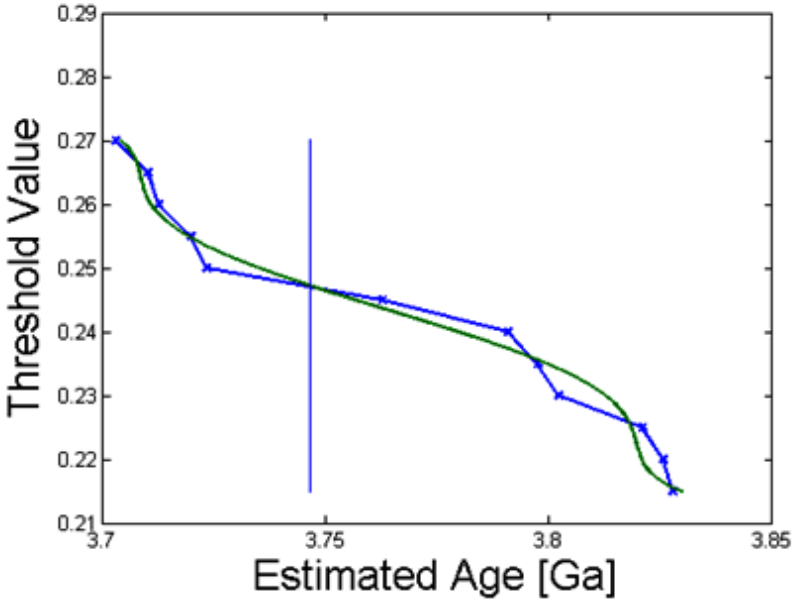

Figure 5.7: The Polynomial Fitting process for Ptolemaeus Crater using the DEM-based detector

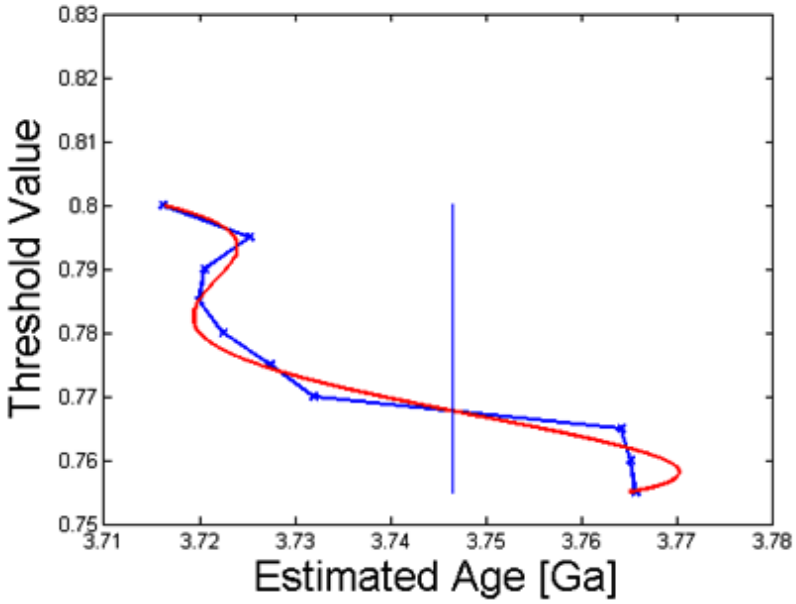

Figure 5.8: The Polynomial Fitting process for Ptolemaeus Crater using the image-based detector

Figures (5.9-5.10) shows the reaction of the Alphonsus crater dataset via the polynomial fitting process, the newly estimated ages values are as (3.778 Ga) after the DEM-based detector process the and (3.802Ga) with the Image-based detector.

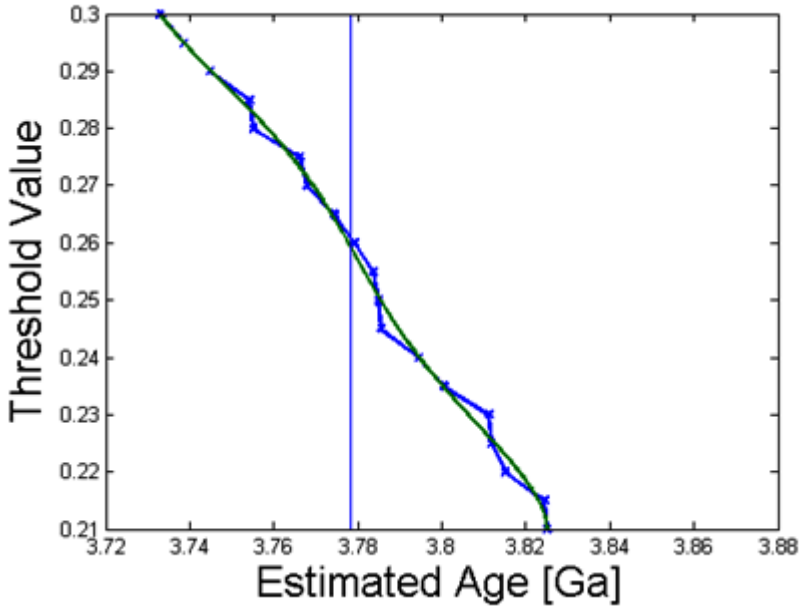

Figure 5.9: The Polynomial Fitting process for Alphonsus Crater using the DEM-based detector

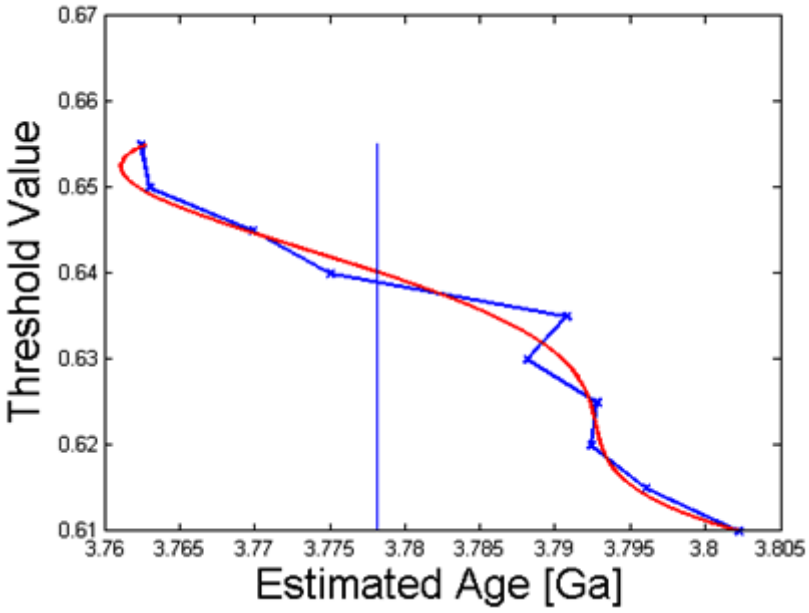

Figure 5.10: The Polynomial Fitting process for Alphonsus Crater using the image-based detector

The estimated ages obtained for Ptolemaeus and Alphonsus regions after the fifth-degree polynomial fitting optimization process are shown down in Table 5.3, which react a very encouraging impression, as they are very close values to the reference values.

Table 5.3: The Re-Fine Estimated Age Values after Implementing Polynomial Fitting Process

Table 3	Alphonsus	Ptolemaeus
LU78287GT catalogue (Reference value)	3.78 +0.011 -0.013 Ga	3.75 +0.015 -0.022 Ga
DEM-based detector	3.778 Ga	3.756 Ga
Image-based detector	3.802 Ga	3.756 Ga

Chapter 6

Validation with Small Craters: Lunar Crater Hell Q

The determination of the age of planetary surfaces basically depends on the areal density of detected craters. The analysis of the impact (CSFD) is a classical approach that supports the age estimation process for planetary surfaces. Usually, manual CSFD measurements and size evaluation is leading to an estimate of the CSFD, which is consequently considered as a time-consuming process especially for large surface areas provided with a high image resolution. The availability of global image mosaics at high resolution implies a need for automated crater detection algorithms. In this chapter, a template-based CDA is applied to analyze image data under known illumination conditions. The results are used to produce the CSFD for a region around the young lunar crater Hell Q, where the threshold value of the applied automatic CDA is calibrated based on a 16 km^2 region with known manual crater count data. As an advanced step, the accordingly configured CDA is then applied to a much larger surface region of about 70 km^2 surrounding the selected calibration area, and a spatially resolved map of the surface age is calculated for overlapping rectangular areas, each covering 2 x 1.5 km^2. The obtained age values range from 1-2 Ma for the immediate vicinity of Hell Q to about 60 Ma at about 10 km distance from Hell Q.

This chapter has been adapted and/or adopted from: (Salih et al., 2016b).

6.1 Hell Q Crater Area Introduction

Estimation of the geologic age of planetary surfaces is of high interest in planetary research. The surface age estimation relies basically on counting impact craters and measuring their diameters. The availability of large amounts of high-resolution planetary images that cover different solar system objects provides the possibility to study them deeply and construct crater catalogues that contain large numbers of manually detected small craters (Stepinski et al., 2012; Robbins, 2016).

Apparently, impact craters are the results of previous impacts that happened at different intervals of time on planetary surfaces (Hörz et al., 1991). Impact craters exist in large

abundances and are widespread on the Moon, Mars, and Mercury due to the lack of an atmosphere and conditions suitable for life (Grieve et al., 2007). The age of a planetary surface increases with increasing impact crater density, i.e. surfaces with a low number of impact craters are usually younger than densely cratered surface parts. Estimations of the (CSFD) are a basic tool for assessing the ages of surface regions. The derivation of the absolute model age (AMA) of a surface requires obtaining the number of craters and their diameters (Hartmann, 1999; Hartmann and Neukum, 2001; Michael and Neukum, 2010; Michael et al., 2012; Michael; 2013; 2015; Hiesinger et al., 2011).

In this context, manual counting and measuring of craters is a time-consuming process, while automatic crater detection may lead to increased false positive detections. A comparison between automatic CDAs and manual crater counts has been implemented before (e.g. (Stepinski et al., 2012)); the results of the automatic detection algorithm differed, especially for craters of small size.

In this chapter, an automatic CDA is applied to a high-resolution image of the lunar crater Hell Q of about 4 km diameter and its ejecta blanket. Except for Hell Q, the image exhibits only craters of small sizes, less than a few tens of meters in diameter (Fisher, 2014). An absolute model age (AMA) is obtained based on the resulting automated crater counts. By examining the whole surface area of the available high-resolution image a map of the surface age is created based on the automatically obtained crater counts.

In this chapter, the CDA described in chapter three is applied to the Lunar Reconnaissance Orbiter Narrow Angle Camera (LRO NAC) image M126961088LE (http://wms.lroc.asu.edu/lroc/view_lroc/LRO-L-LROC-2-EDR-V1.0/M126961088LE) showing the small crater Hell Q and its surroundings. This CDA is a template matching based system, which is able to detect craters of less than about 10 pixels diameter in lunar images without the need for DEM data. The image-based algorithm will be applied to a part of the image, which will be divided into three equally sized areas for the purpose of evaluation and calibration of the optimal detection threshold. Consequently, the statistical analysis of the automatically estimated CSFD is the main element for the AMA estimation. Furthermore, a spatially resolved AMA map of Hell Q and the neighboring surface will be constructed.

6.2 The Region of Interest: Hell Q

The roughly 4 km small sized crater Hell Q is located at 33.0° S and 4.4° W in the eastern part of the large walled plain Deslandres (Fisher, 2014), roughly 300 km northwest of the well-known large crater Tycho. The lunar crater Hell Q is provided in a Narrow Angle Camera (NAC image M126961088LE) with a high-resolution photograph (0.49m) of the 2.2 km by 7.5 km, which cover around (16.3 km^2) as a study region in Hell Q's northern continuous ejecta blanket that consider as a rich area of small size craters (Figure 6.1). In Fisher (2014), the Hell Q region is regarded for an AMA estimation based on very small craters with diameters between (5 m and 41 m), where potential secondary craters are excluded by detecting non-uniform spatial distributions using a statistical test.

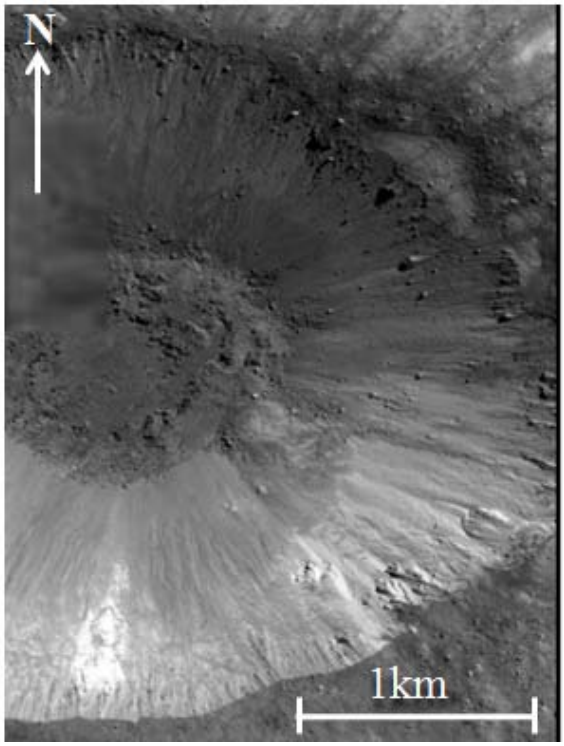

Figure 6.1: The M126961088LE Hell Q Crater (LROC Observation M126961088L. 2010)

According to Fisher (2014), the ejecta blanket of Hell Q exhibits a lower density of small impact craters than an impact melt pond of Tycho. Consequently, the age of Hell Q is lower than the age of Tycho (McEwen et al., 1992).

In the study in McEwen et al. (1992), which regards among others the craters Hell Q and Tycho, an age of 110-110 Ma is estimated for the crater Tycho and a value below

this range for Hell Q. The young age of Hell Q is inferred from the fact that this crater is superposed on one of the rays formed by ejecta material of Tycho (McEwen et al., 1992). In Stopar et al. (2014), the structure of a small impact melt deposit on the floor of Hell Q is described. In the morphological and spectral study in Chauhan et al. (2012) about the central peak region of Tycho, this crater is considered as a young impact crater of an approximate age of 110 Ma. In the works in Neukum and König (1976) and König et al. (1977) age values of Tycho of 100 Ma and 96 Ma, respectively, are given. Similarly, an age of about 100 Ma is estimated for Tycho in Arvidson et al. (1976). A slightly higher age of 138^{+24}_{-20} Ma has been determined for Tycho in Baldwin (1985). The image data used in this study is LRO NAC image M126961088LE. It has a resolution of about 0.49 m/pixel. The solar angle of incidence amounts to 43.47° (http://wms.lroc.asu.edu/lroc/view_lroc/LRO-L-LROC-2-EDR-V1.0/M126961088LE).

The AMA estimation process relies on the resulting CSFD, which represents the number of craters per diameter interval per area. As a reference for crater detection, an area of 16.3 km^2 size from the surface near Hell Q has been chosen, which is the same as the region analyzed in (Fisher, 2014). All craters in the test region with diameters between 3 m and 41 m were counted manually in Fisher (2014), where very small craters with diameters between (3 m and 7 m) were neglected in the crater counts for the AMA estimation due to the occurrence of the rollover point in the CSFD. Furthermore, craters with diameters between (13 m and 21 m) are neglected in Fisher (2014) due to the non-randomness of the craters in this diameter range, which indicates their origin as secondary craters. As a result, a set of 678 craters is considered suitable in Fisher (2014) for estimating the AMA.

While in the study in Fisher (2014) the software Craterstats2 (http://www.geo.fu-berlin.de/en/geol/fachrichtungen/planet/software/index.html) is used, in this study the Matlab implementation of the CSFD-based AMA estimation method described in Hartmann and Neukum (2001); Michael and Neukum (2010); Michael et al. (2012); Michael (2013, 2015) has been used in order to be able to apply the AMA estimation to a large number of small overlapping sub-areas of the test region. The AMA value obtained based on the applied implementation, regarding the same set of 678 craters as in Fisher (2014), corresponds to $1.50^{+0.069}_{-0.076}$ Ma (See Figure 6.2), which is close to the

value of 1.37±0.052 Ma obtained in Fisher (2014). The small difference is probably due to undocumented features in the software Craterstats2 (Michael, 2015).

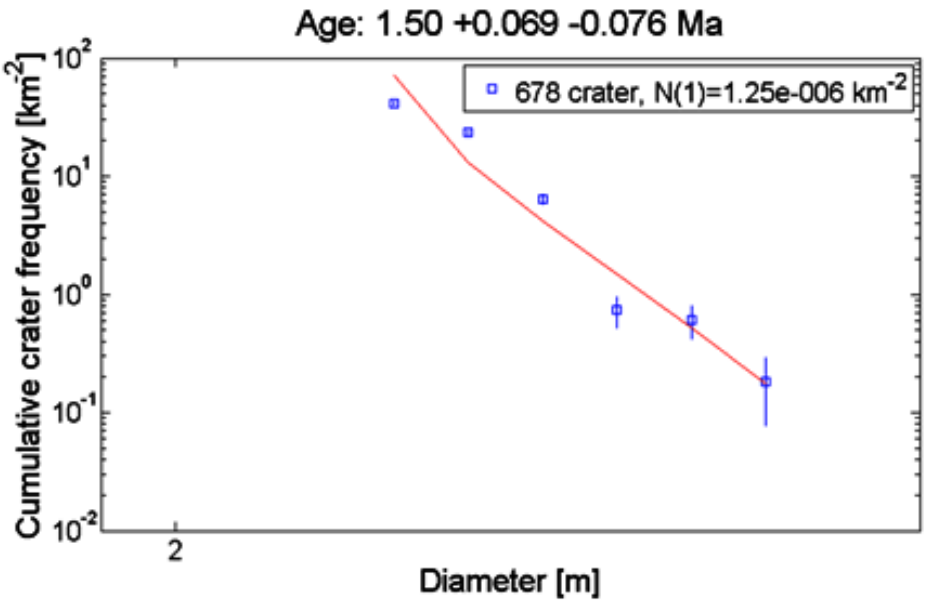

Figure 6.2: The Absolute Model Age (AMA total) for the Hell Q under the new MATLAB

The 678 considered manually counted craters area has been divided into three regions equally for the purpose of calibration and evaluation. Then, an age estimation process has implemented with the new MATLAB function for each of these three groups separately. In this case, for such high-resolution data, only the image (template)-based detector has been applied to it that include different sizes of craters and it is not reasonable to apply the DEM-based detector. The obtained age values from the new MATLAB function for these three referenced ground truth groups are very logical, where the values ranged around the total sum age (1.50 Ma) as shown down in Table 6.1.

Table 6.1: The Reference Data Age obtained with the new MATLAB Function

Reference Data	First Group Data	Second Group Data	Third Group Data	Total craters Data
Number of Craters	**247**	**228**	**203**	**678**
The Estimated Age	**2.42 +0.157 Ma -0.174 Ma**	**1.58 +0.102 Ma -0.113 Ma**	**1.38 +0.111 Ma -0.145 Ma**	**1.50 +0.069 Ma -0.076 Ma**

The template matching based CDA applied in this study strongly depends on a detection threshold that controls the CDA sensitivity and efficiency (See Chapter 4). This threshold value is adjusted such that the automatically determined AMA corresponds as closely as possible to the value obtained by manual CSFD measurements.

For validation purposes, the 16.3 km^2 reference region is divided into three adjacent areas of equal size, and the minimum absolute difference between the CDA-based and the manually determined AMA has been calculated for each of the three sub-areas. The detection threshold obtained for each area is then applied to the other two areas.

Table 6.2 summarizes the resulting number of craters in each sub-area detected by the CDA and by manual counting respectively.

Table 6.2: Results of the Threshold Adaptation: Number of Craters.

Tested on	**Trained on**			
	Area 1	**Area 2**	**Area 3**	**Manual Count**
Optimal Threshold	**0.668**	**0.677**	**0.686**	**-**
Area 1	**92 craters**	**79 craters**	**72 craters**	**247**
Area 2	**127 craters**	**108 craters**	**95 craters**	**228**
Area 3	**97craters**	**84craters**	**74 craters**	**203**

Table 6.3 presents the AMA values derived from the CDA-based algorithm, which range from 1.25 Ma to 2.39 Ma. The arithmetic mean of the three obtained threshold values, corresponding to 0.677, can be considered as the “optimal” threshold. Applying this threshold value to the total 16.3 km² reference area results in an AMA of $1.65^{+0.023}_{-0.024}$ Ma.

Table 6.3: Results of the Threshold Adaptation: Estimated AMAs.

Tested on	Trained on			
	Area 1	Area 2	Area 3	Manual Count
Optimal Threshold	0.668	0.677	0.686	-
Area 1	2.39 Ma +0.064 Ma - 0.066 Ma	1.68 Ma +0.092 Ma -0.100Ma	1.25 Ma +0.194 Ma -0.194Ma	2.42 Ma +0.157 Ma -0.174 Ma
Area 2	1.97 Ma +0.144 Ma -0.177 Ma	1.60 Ma +0.236 Ma -0.236 Ma	1.32 Ma +0.205 Ma -0.205 Ma	1.58 Ma +0.102 Ma -0.113 Ma
Area 3	1.68 Ma +0.086 Ma -0.095Ma	1.53 Ma +0.101 Ma -0.109Ma	1.40 Ma +0.103 Ma -0.110Ma	1.38 Ma +0.111 Ma -0.145Ma

6.3 Age Map of the Hell Q Region

The automatic construction of a surface age map is a new interesting task. To create such map, the template-based CDA has been applied to an orthorectified (1 m/pixel) version of LRO NAC image M126961088LE with a wide sliding window of (2000 × 1500) pixels (2 × 1.5 km^2) moving over the whole image at a step width of 10 pixels (10 m). Given the very small size of the craters and their limited number in this case study, the template-based CDA is able to identify a large fraction of the manually determined craters (a more detailed performance analysis of the CDA is in chapter 3). Only a small fraction is missed due to neighboring or overlapping craters. In addition, there might occur a slight positional offset between template-based CDA and manually detected crater positions, but that does not affect the AMA estimation process as it only relies on the craters density per area and their diameters values.

The CSFDs were computed for the overlapping rectangular sub-areas of LRO NAC image M126961088LE using the “optimal” threshold value of 0.677. Using the Matlab implementation of the CSFD-based technique according to Michael and Neukum (2010); Michael et al. (2012); Michael (2013, 2015), the sub-area specific AMA values were computed and translated into an age map (Figure 6.3).

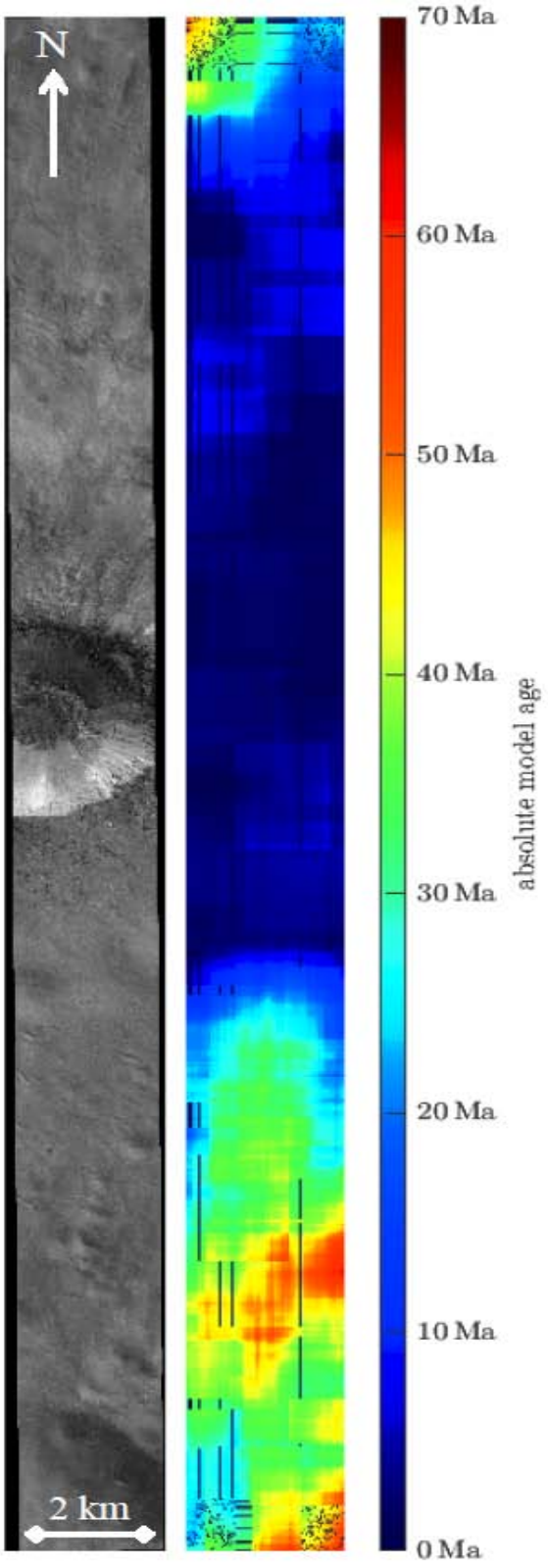

Figure 6.3: Left: Orthorectified 1 m/pixel version of LRO NAC image M126961088LE (provided by Fisher, 2014), showing the crater Hell Q and surroundings. Right: AMA map of the same region.

The AMA values of the map range from between 0.1 and 15 Ma in the center of the region to about 55-70 Ma in the southern, northwestern and southeastern parts of the region.

The CDA-derived AMA map indicates that the crater Hell Q and its immediate surroundings are younger than the surface to the north and south, due to the very young age of Hell Q. The AMA values are gradually increasing from the crater towards the north and more abruptly at about 4 km distance south of the crater (Figure 6.3). The region depicted in blue color in the age map of Figure 6.3 presumably corresponds to the ejecta blanket of Hell Q.

The more or less gradual increase of the surface age with increasing distance from Hell Q may be due to a gradual thinning of the ejecta blanket of Hell Q with increasing distance from the crater. In the thinner parts of the ejecta blanket, craters on the older underlying surface “shine through” the ejecta and thus indicate a higher surface age. The observation that the AMA of the outer parts of the ejecta blanket of Hell Q is younger than 100 Ma, the approximate age of the crater Tycho, can be attributed to the superposition of Hell Q on one of the ejecta rays of Tycho as noted in McEwen et al., 1992.

The study area is considered as being partially affected by secondary crater contamination (Fisher, 2014). Some of the detected craters are distributed as clusters that might influence the inferred AMAs according to Fisher (2014) (see e.g. (McEwen and Bierhaus, 2006) for a general description of the effect of secondary craters on CSFD-derived ages of planetary surfaces). In Fisher (2014), each diameter interval of the histogram representing the CSFD is analyzed with respect to the uniform distribution of the respective craters, where a diameter interval with non-uniform crater distribution is detected using statistical F and G tests and is excluded from the CSFD (Fisher, 2014). Since this approach might remove uniformly distributed craters together with the clustered craters from the same diameter interval, leading to a removal of too many craters from the CSFD, a useful feature of future versions of the system will be a refined statistical analysis of the spatial crater distribution to separate clustered craters from uniformly distributed craters without the need for removing all craters of one or several diameter intervals.

Chapter 7

Age Mapping of Planetary Surfaces and Secondary Crater Detection of the Lunar Crater Tsiolkovsky

The analysis of the impact (CSFD) is a well-established approach to the determination of the age of planetary surfaces. Classically, estimation of the CSFD is achieved by manual CSFD measurements and size determination in spacecraft images, which, however, becomes very time-consuming for large surface areas and/or high image resolution. With increasing availability of high-resolution (nearly) global image mosaics of planetary surfaces, a variety of automated methods for the detection of craters based on image data and/or topographic data have been developed. In this contribution, a template-based CDA is used which analyses image data acquired under known illumination conditions (See Chapter 3). Its results are used to establish the CSFD for the examined area, which is then used to estimate the absolute model age of the surface. The detection threshold of the automatic CDA is calibrated based on a region with available manually determined CSFD such that the age inferred from the manual crater counts corresponds to the age inferred from the automatic crater detection results. With this detection threshold, the automatic CDA can be applied to a much larger surface region around the calibration area.

The proposed age estimation method is demonstrated for a Kaguya Terrain Camera image mosaic of 7.4 m per pixel resolution of the floor region of the lunar crater Tsiolkovsky, which consists of dark and flat mare basalt and has an area of nearly 10,000 km^2. The region used for calibration, for which manual crater counts are available, has an area of 100 km^2. In order to obtain a spatially resolved age map, CSFDs and surface ages are computed for overlapping quadratic regions of about 4.4 x 4.4 km^2 size offset by a step width of 74 m. The constructed surface age map of the floor of Tsiolkovsky shows age values of typically 3.2-3.3 Ga, while for small regions lower (down to 2.9 Ga) and higher (up to 3.6 Ga) age values can be observed. It is known that CSFD-derived absolute model ages can exhibit variations although the surface has a constant age. However, for four 10-20 km sized regions in the eastern part of the crater floor, the created map shows age values differing by several hundred Ma

from the typical age of the crater floor, where the same regions are also discernible in Clementine UV/VIS color ratio image data probably due to compositional variations, such that the age differences of these four regions may be real.

In this chapter, a CDA is applied to dark and flat mare regions on the lunar nearside in order to obtain AMA values based on crater counts which have a similar accuracy to those inferred from manual crater counts.

After achieving the full construction of an age map of the complete crater floor, it is well known that the CSFD may be affected by secondary craters. Hence, the detection results are refined by applying a secondary candidate detection (SCD) algorithm relying on a Voronoi tessellation of the spatial crater distribution, which searches for clusters of craters. The detected clusters are assumed to result from the presence of secondary craters, which are then removed from the CSFD. It is favorable to apply the SCD algorithm separately to each diameter bin of the CSFD histogram. In comparison with the original age map, the refine age map obtained after removal of secondary candidates has a more homogeneous appearance and does not exhibit regions of spuriously high age resulting from contamination by secondary craters.

This chapter has been adapted and/or adopted from: (Salih et al., 2016a; Salih et al., 2017a; Salih et al., 2018).

7.1 Tsiolkovsky Crater Area Introduction

Impact crater counting is one of the most important tools for estimating the geologic age of a planetary surface, i.e. the period of time that has passed since the last resurfacing event. Recent planetary spacecraft missions have provided enormous amounts of high-resolution image data of global coverage for various solar system bodies, allowing for the construction of crater catalogs comprising large numbers of small craters (Stepinski et al., 2012; Robbins et al., 2009; Robbins et al., 2016).

Impacts of small bodies on planetary surfaces lead to the formation of craters (Hörz et al., 1991). Impact craters are especially abundant on Mercury, the Moon, and Mars (McFadden et al., 2007), where they persist over long periods of time due to the lack of plate tectonics, an atmosphere, and life. For planetary bodies without an atmosphere, the

areal impact crater density increases with increasing surface age, i.e. densely cratered surface parts are usually older than surface parts with a low abundance of craters. The impact (CSFD), denoting the diameter-dependent areal density of impact craters for a given surface part, allows for an estimation of the so-called absolute model age (AMA) of the surface (Hartmann, 1999; Hartmann and Neukum, 2001; Michael and Neukum, 2010; Michael et al., 2012; Michael, 2013, 2014, 2015; Hiesinger et al., 2011).

In this chapter, the instructed automatic CDA is applied to the mare-like floor region of the lunar farside crater Tsiolkovsky, in order to obtain crater counts of similar accuracy as manual crater counts. A surface age map is created based on the automatically obtained crater counts, resulting in a spatially resolved map of the AMA of the examined surface area.

An important aspect in CSFD-based AMA estimation is the influence of secondary cratering on the CSFD. The process of secondary cratering usually occurs on planetary bodies having a gravitational acceleration, which is high enough for the ejecta from an initial impact to fall back on the planet's surface. In the last decades, a number of researchers have focused on analyzing the role of secondary craters in the estimation of the AMA. They concluded that secondary craters "contaminate" the crater statistics, which results in inaccurate age estimation especially when craters smaller than about 1 km are considered (e.g., McEwen and Bierhaus, 2006; Werner et al., 2009; Robbins and Hynek, 2014).

To speed up the CSFD measurements process, a number of automatic detection and counting methods have already been developed. Some of them are fully automated but dependent on the choice of a detection threshold. According to the previous literature, none of them has the capability of automated detection of secondary crater candidates (e.g., Salamunićcar and Lončarić, 2010).

The main goal of this advanced step is to develop an automated approach to elimination of secondary craters that would be combined with semi-automatic template matching based crater detection. This would reduce the time burden and complexity of crater counting as well as the amount of proficiency needed to achieve accurate age estimation results. The Tsiolkovsky crater area is a good testing ground for this method because of its size and the homogeneous lava-flooded floor.

In this chapter, a statistically-based automated approach to the discrimination between primary and secondary craters is described. The Tsiolkovsky crater area is used as a testing ground for this method because of its size and the presence of a homogeneous lava-flooded floor. As a final result, an AMA map of the floor of Tsiolkovsky corrected for secondary craters is presented. The results presented in this chapter are encouraging for further improvement of this automatic method via alternative clustering criteria and testing on other lunar surface parts.

In this context, the template matching based CDA introduced by Grumpe and Wöhler (2013) with the ability of automatic detection of small craters (<10 image pixels in diameter) in lunar images will be used for crater detection (See Chapter 3). This template-based algorithm which depends on a few parameters, such as a threshold of similarity between the impact crater template and the actual image is applied to orbital image data of the mare-like floor region of lunar crater Tsiolkovsky. The main step in the estimation of the absolute surface age is the statistical analysis of the CSFD constructed using the image-based CDA for determining the locations and diameter values for the derivation of the AMA. Accordingly, a spatially resolved AMA map of the whole floor of Tsiolkovsky will be constructed.

7.2 The Region of Interest: Tsiolkovsky

The surface area of crater Tsiolkovsky (See Figure 7.1) is one of a small number of lava-filled lunar farside craters, thus having a very dark and smooth crater floor. It is located at (20° S, 129° E) and has a diameter of approximately 180-200 km. The central peak located in the northern part of the mare-filled region has a “W” shape (Tyrie, 1988a). Previous studies regarding Tsiolkovsky crater suggest ages around 3.8 Ga (Walker and El-Baz, 1982) and 3.5 ± 0.1 Ga (Tyrie, 1988b) for the floor region. A recent age estimation has been performed by Pasckert et al. (2015), who obtained 3.19 Ga (+0.08 / −0.12) Ga. In this study, the images acquired by the Terrain Camera (TC) of the lunar spacecraft Kaguya (Haruyama et al., 2012) have been used. The resolution of the image is 7.4 m per pixel. The dark mare fill inside Tsiolkovsky crater is the area of interest, as it appears to be geologically homogeneous.

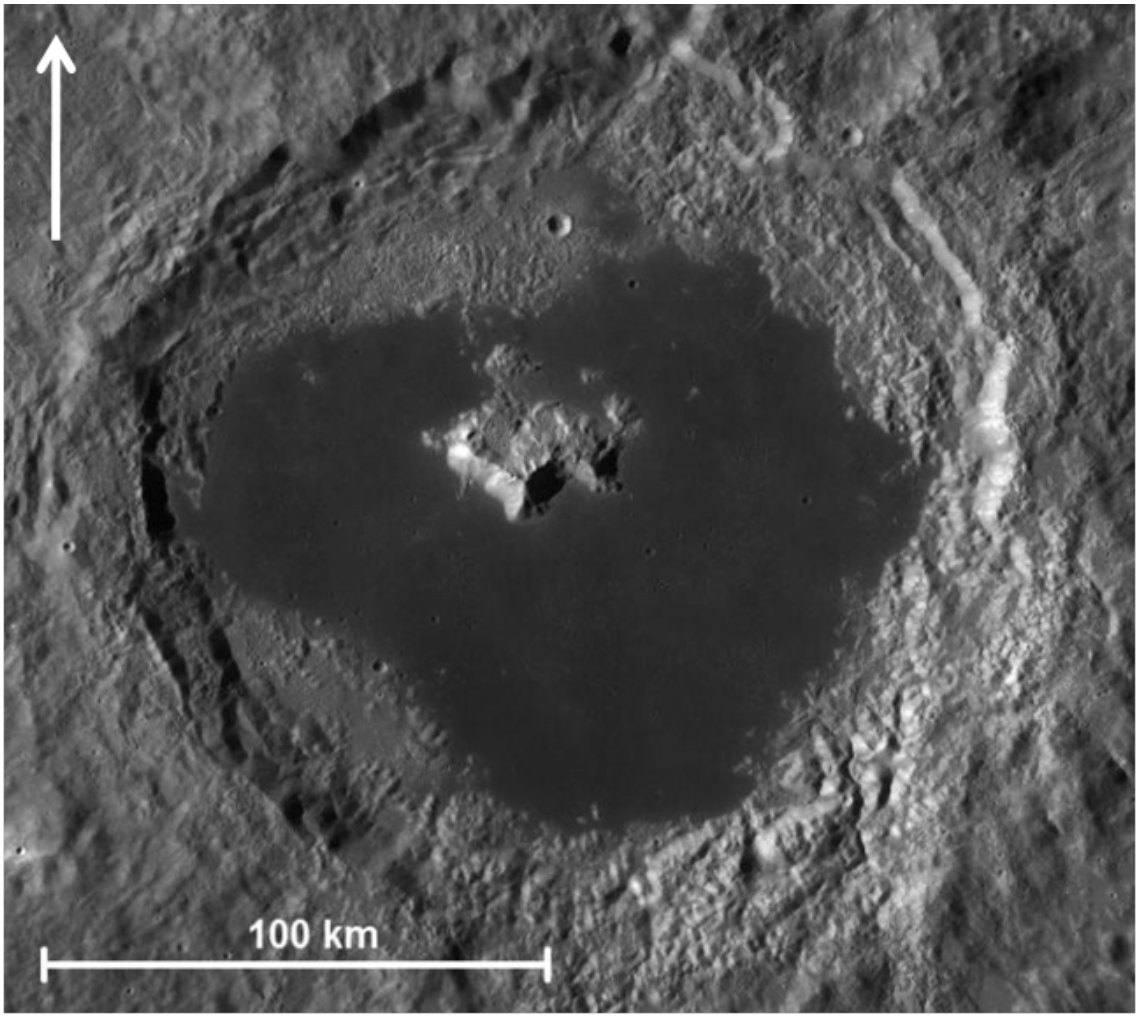

Figure 7.1: Tsiolkovsky Crater image, extracted from the Lunar Reconnaissance Orbiter Wide Angle Camera global mosaic (Speyerer et al., 2011).

7.3 Age Estimation, Mapping With Template Matching Algorithm

The estimation of the absolute model age (AMA) mainly depends on the number of craters per diameter interval and per area, the CSFD. A surface part of around 100 km^2 - size inside the crater Tsiolkovsky has been chosen as a reference dataset for the crater detection, which has been evaluated manually by Pasckert et al. (2015). The crater diameter interval considered for estimating the AMA ranges from 128 m to 1000 m. Smaller craters were not taken into account because the detection rate of the CDA decreases with decreasing diameter for diameters less than about 100 m, leading to an artificial “roll-off” of the CSFD.

Like virtually all other object detection algorithms, the applied template matching based CDA relies on a threshold value, which controls the sensitivity of the detector. The

threshold value has been adjusted such that for a given reference area with available manual crater counts, it yields an AMA that comes as close as possible to the manually determined AMA.

One reliable way to calibrate this threshold is to use an area with manually counted craters. The area is split into three equal sub-regions in size. A threshold for each area is estimated so as to closely match the corresponding manual count. The result consists of three slightly different thresholds, whose mean value can be chosen as an "optimal" threshold value for this area. For each area, the absolute difference between CDA-based and manually determined AMA was minimized by a quasi-Newton method. The resulting threshold is then tested on the remaining two areas. The number of craters in each sub-area detected by the CDA and by manual counting, respectively, is summarized in Table 7.1.

Table 7.1: Results of the Threshold Adaptation: Number of Craters.

Tested on	**Trained on**			
	Area 1	**Area 2**	**Area 3**	**Manual Count**
Optimal Threshold	**0.6562**	**0.6562**	**0.6579**	**-**
Area 1	**231 craters**	**231 craters**	**229 craters**	**157 craters**
Area 2	**238 craters**	**238 craters**	**234 craters**	**145 craters**
Area 3	**244 craters**	**244 craters**	**238 craters**	**146 craters**

The derived CDA-based AMA values between 3.00 Ga and 3.44 Ga are always consistent with the manually determined AMA values (Table 7.2).

The "optimal" threshold value was chosen to be the arithmetic mean of the three obtained thresholds. Consequently, the CDA was applied to the total 100 km² reference area with a cross-correlation threshold value of 0.6568, resulting in an AMA of 3.21 ± 0.13 Ga, being very similar to the AMA of $3.37^{+0.068}_{-0.068}$ Ga obtained based on manual counting by Pasckert et al. (2015).

Table 7.2: Results of the Threshold Adaptation: Estimated AMA.

Tested on	Trained on			
	Area 1	Area 2	Area 3	Manual Count
Optimal Threshold	0.6562	0.6562	0.6579	-
Area 1	3.44 Ga +0.066 Ga -0.066 Ga	3.44 Ga +0.066 Ga -0.066 Ga	3.43 Ga +0.067 Ga -0.067 Ga	3.44 Ga +0.066 Ga -0.066 Ga
Area 2	3.36 Ga +0.045 Ga -0.079 Ga	3.36 Ga +0.045 Ga -0.079 Ga	3.35 Ga +0.047 Ga -0.084 Ga	3.36 Ga +0.045 Ga -0.080 Ga
Area 3	3.02 Ga +0.251 Ga -0.251 Ga	3.02 Ga +0.251 Ga -0.251 Ga	3.00 Ga +0.262 Ga -0.262 Ga	2.99 Ga +0.144 Ga -0.272 Ga

7.4 Tsiolkovsky Age Map

To create a spatially resolved AMA map, the template matching technique has been applied to the 7.4 m/pixel resolution Kaguya image data with a 600x600 pixel (4.4x4.4 km²) wide sliding window moving over the whole image of the crater Tsiolkovsky with a step width of 10 pixels (74 m). The CDA successfully identifies a high fraction of the manually determined craters and determines reasonable diameter values, as apparent from Figure 7.2. Slight offsets by a few pixels between the CDA-based and manual crater positions tend to occur, which do not affect the AMA estimation as it only depends on the estimated diameters and areal density of the craters.

Based on the optimal threshold value of 0.6568, CSFDs were computed for overlapping quadratic sub-regions covering the completely mare-like crater floor in order to estimate an AMA value for each sub-region, leading to a spatially resolved AMA map (Figure 7.3). The AMA values were obtained using the created Matlab implementation (See Chapter 3) of the CSFD-based method for AMA estimation (Michael and Neukum, 2010; Michael et al., 2012; Michael; 2013; 2015). Most AMA values of the map lie between 2.9 and 3.6 Ga, with the majority of AMAs, centered around 3.3 Ga. In the AMA map, the central peak, the crater walls and the parts of the crater floor not covered by mare basalt were excluded. According to stratigraphic considerations, the age of these steeply sloped regions exceeds that of the dark mare floor.

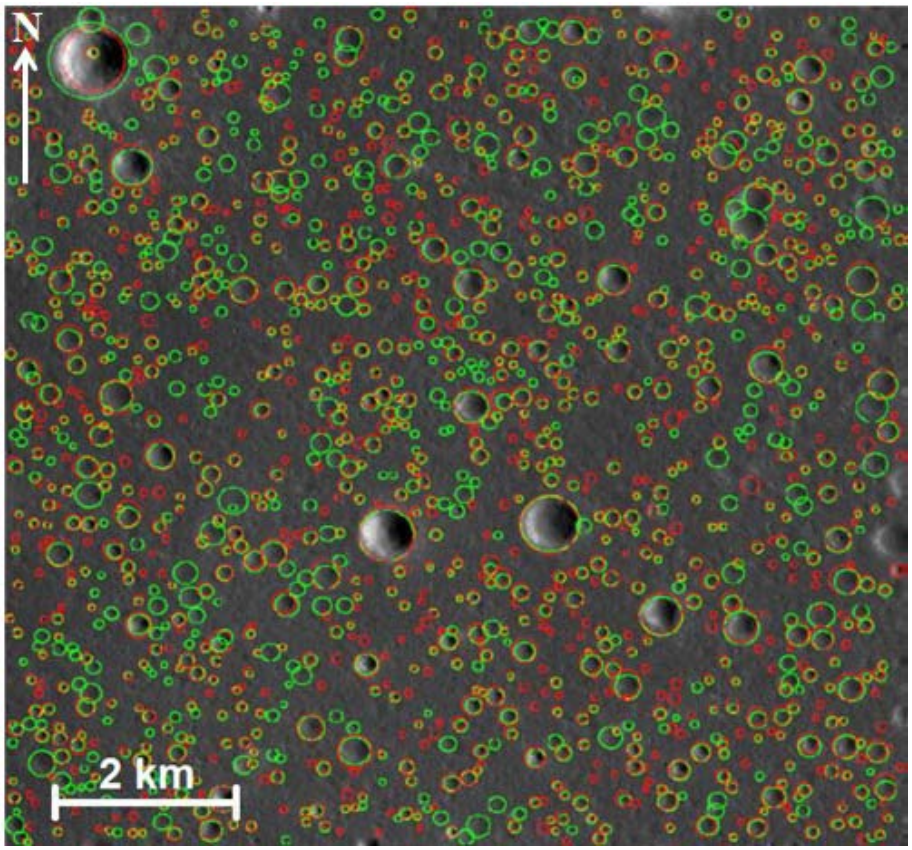

Figure 7.2: Part of the calibration area. Manually counted craters are indicated by green circles, CDA detection results by red circles. Image data: Kaguya TC (Haruyama et al., 2014).

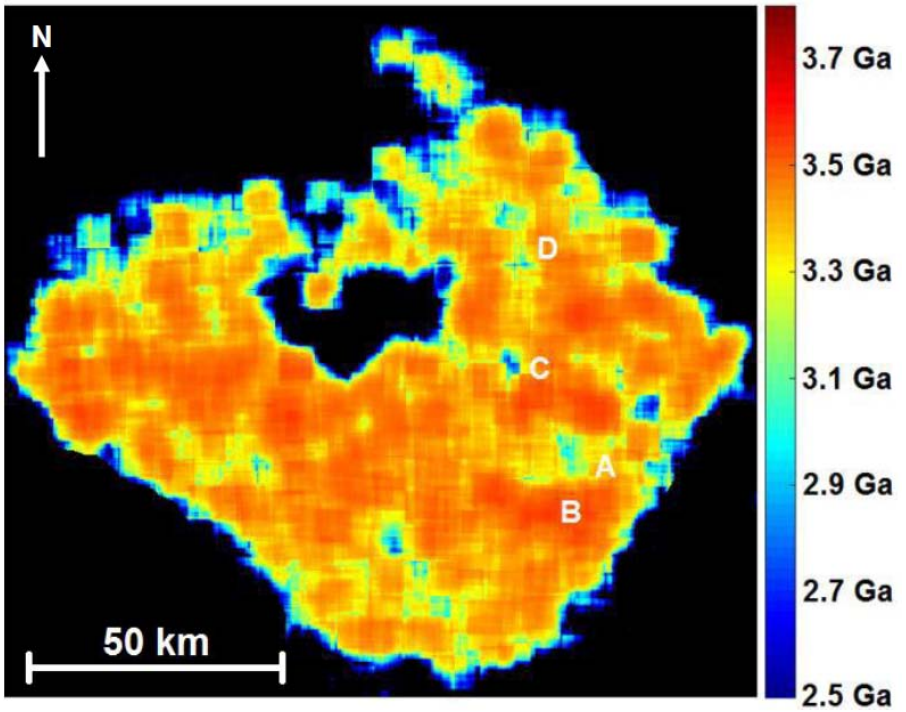

Figure 7.3: AMA map of the floor of the crater Tsiolkovsky. The mare-like floor region has been extracted manually. Black: no data.

The color ratio map of the crater Tsiolkovsky (Figure 7.4) was derived from Clementine UV/VIS multispectral data (red channel: 750 nm/415 nm reflectance; green channel: 750 nm/950 nm reflectance; blue channel: 415 nm/750 nm reflectance, according to Pieters et al. (1994) and http://www.mapaplanet.org/explorer/help/data_set.html#moon_clementine_ratio) (Pasckert et al, 2015). It can be used to identify compositionally distinct geological units on the mare-like crater floor. If the mapping of the CDA-derived AMA yields reliable results, similar units should be found within the age map. Although frame-specific calibration artifacts make it hard to unambiguously divide the color ratio image into geological units, some similarities between structures visible in Figures 7.3 and 7.4 are clearly apparent through visual comparison. Specifically, four localized AMA anomalies can be found in the eastern part of the crater floor. They are represented by the letters A, B, C and D in Figures 7.3 and 7.4, where each letter denotes a small spectrally distinct region in the color ratio image. Regions A, C, and D have lower AMAs than the surrounding surface area, respectively (about 2.9-3.2 Ga), while for region B a higher AMA of about 3.5 Ga has been estimated. According to Figure 7.4, these small regions can all be distinguished spectrally from the surrounding surface, indicating compositional variations of the mare basalts (Salih et al., 2016a).

Van der Bogert et al. (2015) showed for a cratered surface area of 100 km² for which the CSFD has been synthetically generated under the assumption of a uniform AMA of 4.0 Ga that estimates of the AMA for sub-regions of 4 km² size deviate by several hundred Ma from the true AMA, while accurate and reliable estimated AMA values are obtained for 10 km² sub-regions. Given the comparably large size of about 20 km² of the overlapping sub-regions analyzed in this study, the AMA fluctuations apparent in Figure 7.3 are likely to be real, which is confirmed by their correlation with spectral variations in the Clementine color ratio image.

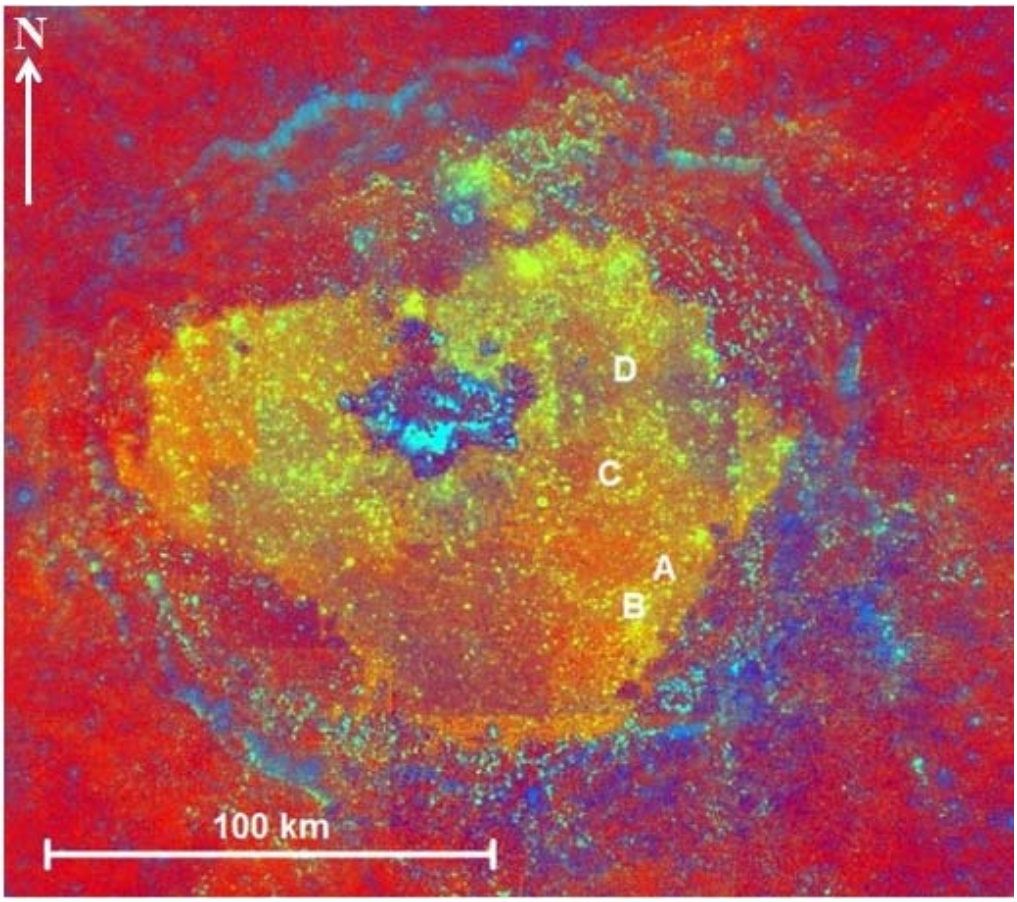

Figure 7.4: Clementine UV/VIS color ratio image of the crater Tsiolkovsky (downloaded from http://www.mapaplanet.org/explorer/moon.html, the definition of color channels according to Pieters et al., 1994).

A more detailed view of the eastern and southeastern part of crater Tsiolkovsky is shown in Figure 7.5. It reveals that the two small low-AMA anomalies marked in Figures 7.3 and 7.4 by letter D are located at the same locations as two bright details in Figure 7.1, corresponding to small mountains of the original crater floor that penetrate through the dark mare basalt layer. Hence, the lower estimated AMA is probably due to the small craters being destroyed more easily on the steep slopes on the flanks of these mountains. The low-AMA anomalies marked by letters A and C cannot be linked to any conspicuous surface details but correspond to dark surface parts with a visually apparent low abundance of small impact craters. In contrast, the high-AMA anomaly marked by letter B corresponds to an area of slightly increased albedo characterized by a visually apparent exceptionally high abundance of small craters.

The distribution of these craters as a cluster, however, suggests that they are secondary craters (McEwen and Bierhaus, 2006). Thus, the seemingly increased AMA of region B probably does not reflect a real surface age but is due to the presence of these secondary

craters (a more detailed analysis of the effect of secondary craters on the estimated surface age is provided later in this chapter).

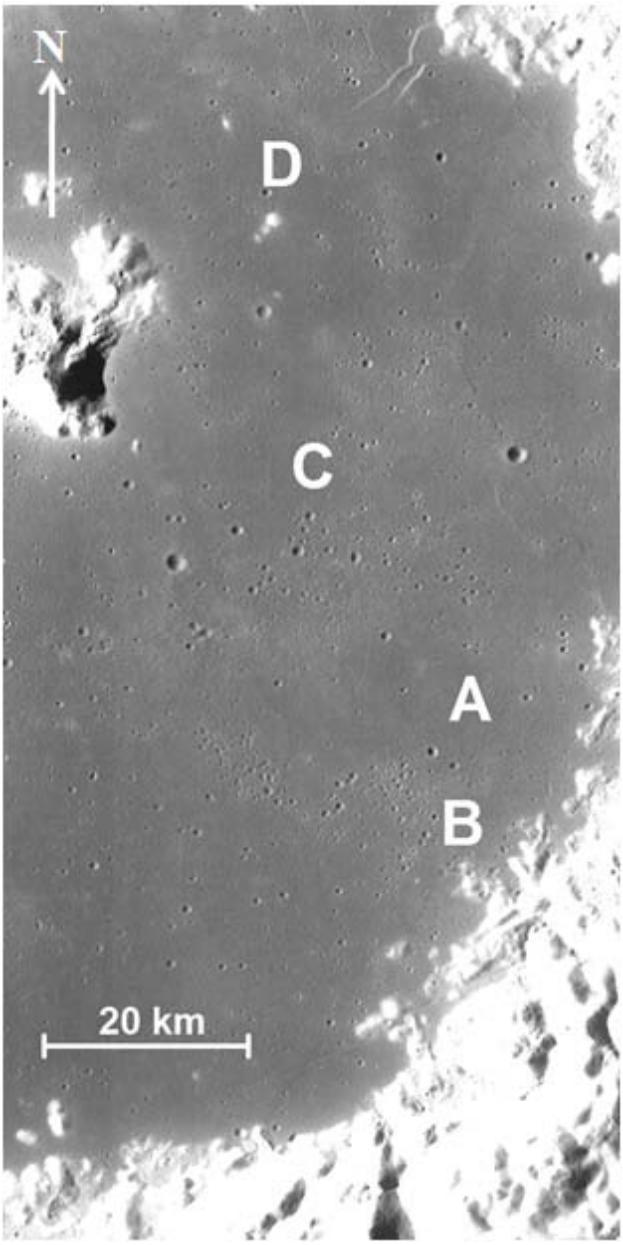

Figure 7.5: Detailed view of the eastern and southeastern part of Tsiolkovsky. The regions A-D marked in Figures 7.3 and 7.4 are indicated. Contrast-enhanced excerpt from the global LROC WAC mosaic (Speyerer et al., 2011).

Hence, the AMA anomalies B and D are not due to lava flows having an age differing from the mean age of the crater floor. The negative AMA anomalies A and C might be interpreted as lava flows of a composition and age different from the rest of the crater floor, which would imply the occurrence of small eruptions on the floor of Tsiolkovsky several hundred (Ma)s after the emplacement of the majority of the mare basalts. An

alternative (and probably more realistic) interpretation for regions A and C is that the distribution of small craters on the floor of Tsiolkovsky may be affected in a spatially variable manner by secondary craters, which would then cause the observed AMA variations across the crater floor (Salih et al., 2016a).

7.5 Statistical Method Used for Secondary Candidate Detection

Age dating by CSFD measurements is based upon the assumption that a new surface forms without impact craters. Over time, it is bombarded by asteroids and comets, which results in an increase of the impact crater population. The age of a surface can be estimated by assessing the distribution of craters and fitting estimated (CSFD) to the production function (See Chapter 3), which depends on the absolute age of the surface (Neukum, 1983).

In this study, at least partially account for the effect of secondary craters on the CSFD by following a direct statistical approach and proposing a technique to remove secondary craters from the CSFD based on the assumption that they do not exhibit a uniform spatial distribution but tend to appear in chains and clusters. Hence, secondary craters are distinguished from the surrounding primary population of similar diameter based on their distinctly non-uniform spatial distribution. Of course, this approach will not recognize a possible uniformly distributed population of secondary craters. Furthermore, clustered craters may also be of primary origin when old and thus strongly cratered surface areas are surrounded by younger surfaces. A well-known example is the Kipuka Darney, a strongly cratered and relatively bright area in Mare Cognitum surrounded by presumably younger mare lava exhibiting a much lower crater density and a significantly lower albedo (Nichols et al., 1974). Hence, an automatic detection of clusters of putative secondary craters always has to be accompanied by a geological analysis of the region under study in terms of, e.g., surface texture and spectral behavior. For this reason, the method described in this section to the mare-flooded floor of the lunar farside crater Tsiolkovsky will be applied, which shows a high degree of homogeneity with respect to its surface texture and spectral appearance.

In most previous studies, secondary craters were removed from the CSFD manually. An attempt to develop a method for estimation of the secondary crater population was made

by Bierhaus et al. (2005), who utilized the single-linkage clustering algorithm together with Monte Carlo simulations in order to distinguish clusters of secondary craters from the spatially uniform distribution of primary craters. A more recent approach by Michael et al. (2012) is based on the distribution of distances between the craters, in particular, the mean 2nd-closest neighbor distance. Michael et al. (2012) concluded that the crater density obtained from an ideal random distribution is related to this statistical distance value.

The main idea of the Secondary Candidate Detection (SCD) algorithm is to detect secondary craters based on deviations of their spatial distribution from the uniform distribution of the surrounding primary craters (which is similar to Michael et al. (2012)) but using a different criterion for detecting crater clusters. Hence, the SCD algorithm determines whether the crater population is uniformly distributed or clustered, which allows for removing the secondary crater candidates from a crater population that is used to estimate the age of a surface part.

The first step is to obtain crater locations using the template matching results of the given region. Primary craters are created from a random distribution of bodies hitting the surface. Their distribution should appear uniform and homogeneous. In contrast, secondary craters usually appear as high-density regions. To separate the secondary crater population from the background population, an algorithm that removes secondary crater candidates from any spatial distribution is developed. This method combines a Voronoi tessellation, Monte Carlo simulations of a uniform distribution, and a one-tailed test of clustering, which divides the detected craters into two groups based on the probability that they exhibit a non-uniform spatial distribution. The technique of Voronoi tessellation has also been used in the work of Honda et al. (2014) to detect non-uniformly distributed craters.

The SCD algorithm recognizes distal secondary craters from the surrounding primary population based on their clustering with respect to an ideal random distribution. Similar to Bierhaus et al. (2005), this algorithm generates a new uniformly distributed population, which has the same average density as the detected craters. Then the Voronoi tessellation is applied to each population, and distribution parameters are calculated for each iteration of the simulation process (See Chapter 3).

The Voronoi diagram (Voronoi tessellation) is a method of subdivision of a plane into regions that comprise the part of the plane around each point within a distance that is shorter than the distances to the neighboring points (Aurenhammer, 1991). Clustering can be inferred based on deviations of the local spatial density from the mean spatial density indicated by variations of the Voronoi cell area. Unfortunately, the statistical distribution of the Voronoi cell area for a uniform distribution cannot be derived from the observed spatial crater distribution due to its possible contamination by clustered secondary craters, such that the Voronoi cell area distribution should be inferred from simulations (Chiu, 2003). The fact that the distribution of points is usually computed for a bounded observation area introduces edge effects to the polygons close to the boundary of the observation area. To avoid these undesirable effects, polygons at the boundary have to be ignored.

In each iteration of the algorithm, craters are uniformly redistributed on the surface. A new Voronoi tessellation is computed along with the areas of Voronoi polygons. After simulation of n iterations, a distribution model of Voronoi cell areas is obtained and the median and standard derivation are computed. The clustering values, i.e., areas of Voronoi polygons, of the original crater distribution are compared to the threshold value obtained from Monte Carlo simulations of random impacts. The proposed algorithm detects a crater as a secondary crater candidate if its Voronoi cell area is below a threshold value, which resembles a one-tailed test of clustering.

The SCD algorithm has been applied many times such that the statistical analysis is applied to several diameter intervals separately. This is expected to provide a better detection performance as the statistical spatial distribution of craters strongly depends on their size. In this study, eight (8) intervals with limiting diameters of 80, 170, 260, 350, 440, 530, 620, 710, and 800 m that relied on same difference intervals between the bins have been used.

7.6 Results and Conclusions for Crater Tsiolkovsky Referenced Area

The SCD algorithm has been applied to different regions of crater Tsiolkovsky in order to analyze the impact of the secondary craters on the crater density, as well as the difference of the estimated ages obtained for the CSFDs with and without secondary

craters. As a first step, the template-based CDA has been applied to a small area in the middle of crater Tsiolkovsky for which manual crater counts are available as reference data (Pasckert et al, 2015). This reference area has a size of 99.867 km^2 with a total number of 1967 craters, ranging from 23 m to 905 m in diameter. Figure 7.6 presents the resulting CSFD of this test area, based on a range of 128-1000 m, thus excluding the rollover apparent at small diameters. This results in an age of 3.21±0.132 Ga, this is very similar to Pasckert et al., (2015).

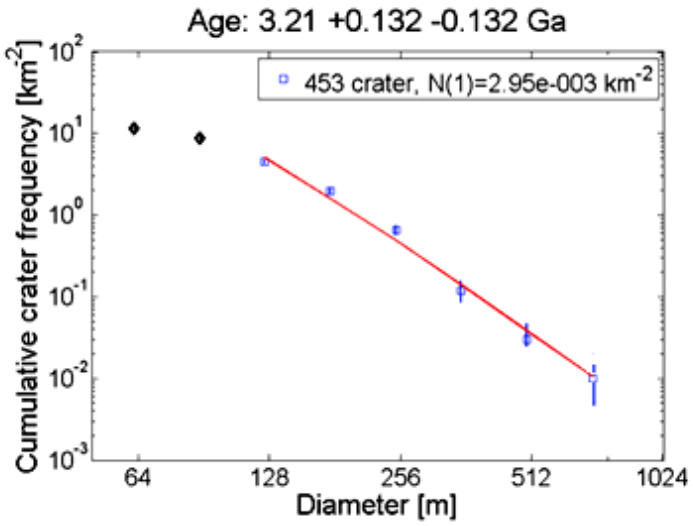

Figure 7.6: AMA obtained based on the craters in the reference region in the diameter range 128–1000m.

Crater detection has been performed using the previously described template matching algorithm to the given region. The diameter range of (128–1000) m is used for the template matching algorithm; as craters with smaller diameters would result in a large number of false positive detections. Previously, an optimal cross-correlation threshold of 0.6568 (See Section 7.3) had been determined for this area by Salih et al. (2016a). Applying Template Matching to the reference area with this threshold resulted in an age estimate of 3.35 Ga. This previous threshold was determined based on automatic crater detection results without any consideration of changes due to automatic removal of secondary crater candidates.

A new template matching threshold value of 0.6525 has been computed based on the application of the template-based automatic detection by minimizing the age difference between the age obtained from the reference data and the age resulting from template

matching combined with secondary crater removal. The resulting threshold is not far away from the original threshold.

To obtain the optimal clustering threshold, the detected craters are distributed 1000 times by Monte Carlo modeling. The Voronoi tessellation and Voronoi areas for every crater were computed for each iteration. The results of the application of the algorithm to the test area are shown in Figure 7.7.

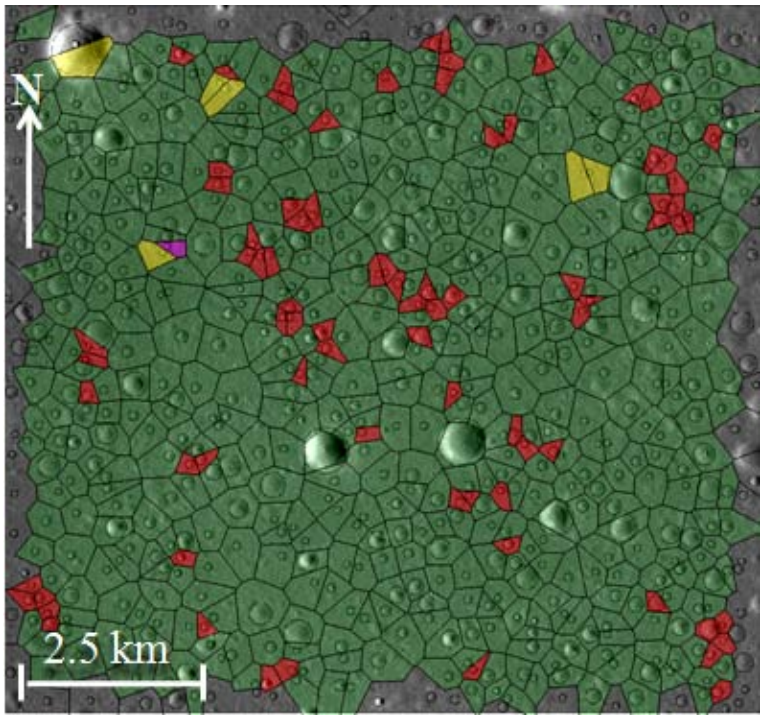

Figure 7.7: Visualized results of applying SCD algorithm to Kaguya TC image data of the floor of lunar crater Tsiolkovsky. Red areas correspond to detected secondary crater candidates, green areas to detected primary crater candidates.

To illustrate the effect of the clustering threshold value, the algorithm with different threshold values to the detected craters has been applied. Lower threshold values can detect only a very small number of secondary crater candidates, and its impact on the age estimate is insignificant.

Both SCD algorithms (with and without application in bins) correspond well on the number of detected craters with diameters less than 150 m, while in the range of (150 – 80 m) the number of automatically detected craters is significantly lower without application of bins (Werner et al., 2009). The binned SCD algorithm detects more craters in the larger diameter range, which would probably be considered primary craters by a human expert (Figure 7.8). Separating craters into diameter bins shows an

increase in the detection of secondary craters although most craters with diameters exceeding 500 m are falsely denoted as secondary craters due to their more irregular distribution resulting from their relatively small number. Hence, the diameter intervals exceeding 500 m were excluded from the AMA estimation when applying the binned SCD algorithm. The final AMA results are displayed in Figure 7.9. The binned SCD algorithm shows an age estimate, which is closer to the reference value than the SCD algorithm applied to all craters.

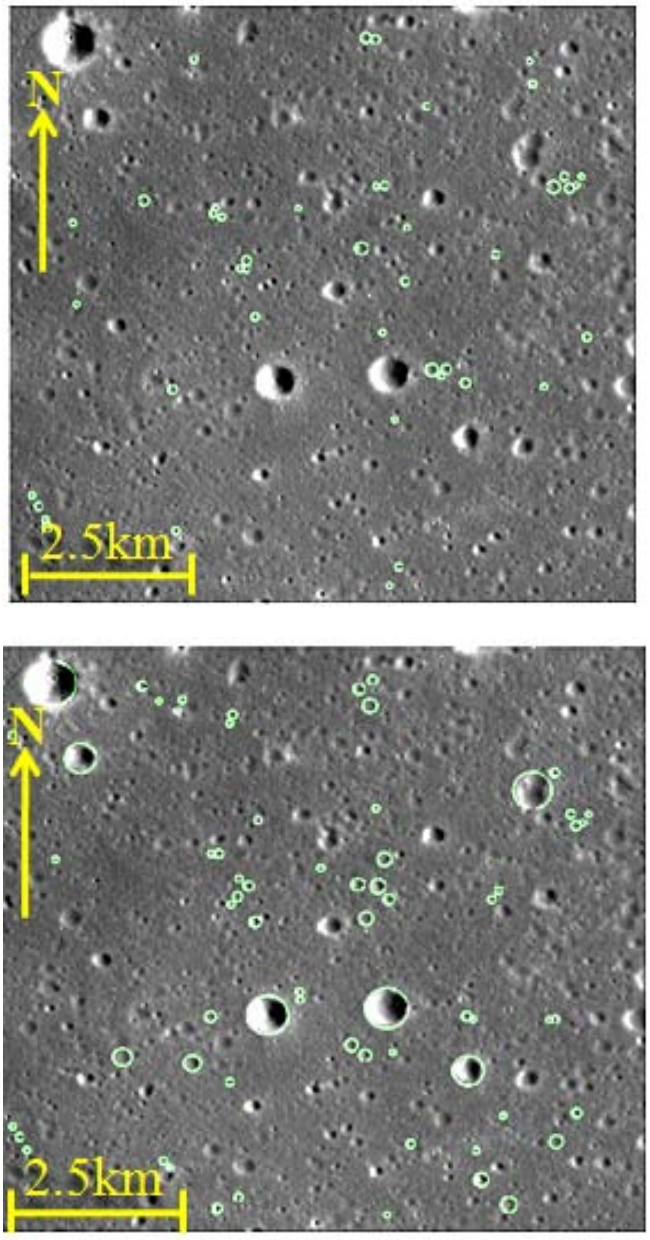

Figure 7.8: Craters detected in Kaguya TC image data by the SCD algorithm (top) and the binned SCD algorithm (bottom).

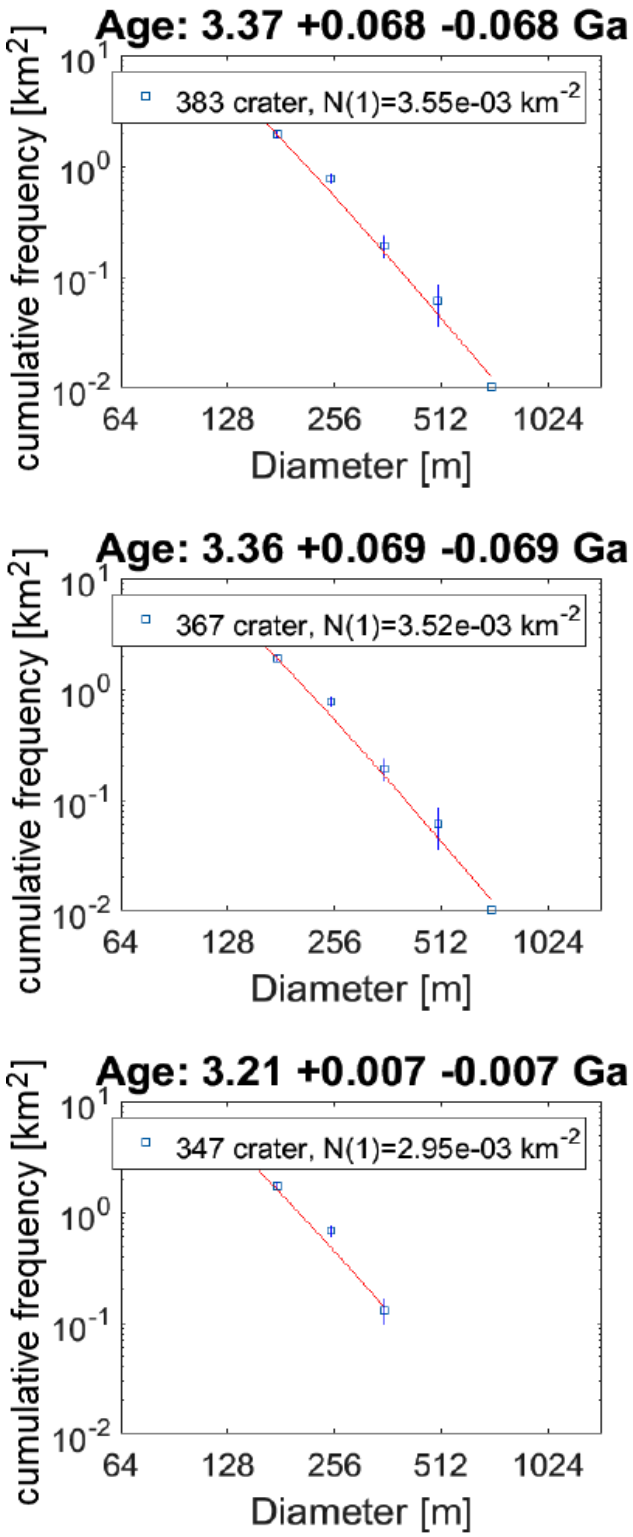

Figure 7.9: AMAs for the reference area, obtained using the template matching algorithm without SCD (top), with unbinned SCD algorithm (middle) and with binned SCD algorithm (bottom).

7.7 Results for Non-Reference Areas in Crater Tsiolkovsky

For further evaluation of the method, three larger areas on the crater floor of Tsiolkovsky denoted as E, F, and G in Figure 7.10, have been analyzed with the algorithm. Each selected region has an area of about 2700 km^2 (52 km by 52 km). Unfortunately, there are no reference data for these regions except the small part manually counted by Pasckert et al. (2015). This count area belongs to region F in Figure 7.10 and, consequently, age estimates have to be similar. Because these regions represent parts of the mare-flooded crater floor of Tsiolkovsky, the previously determined optimal threshold value was applied. A 600 by 600 pixels window for constructing crater density and age maps with a step width of 10 pixels has been applied. Central peak material was excluded from the counting area.

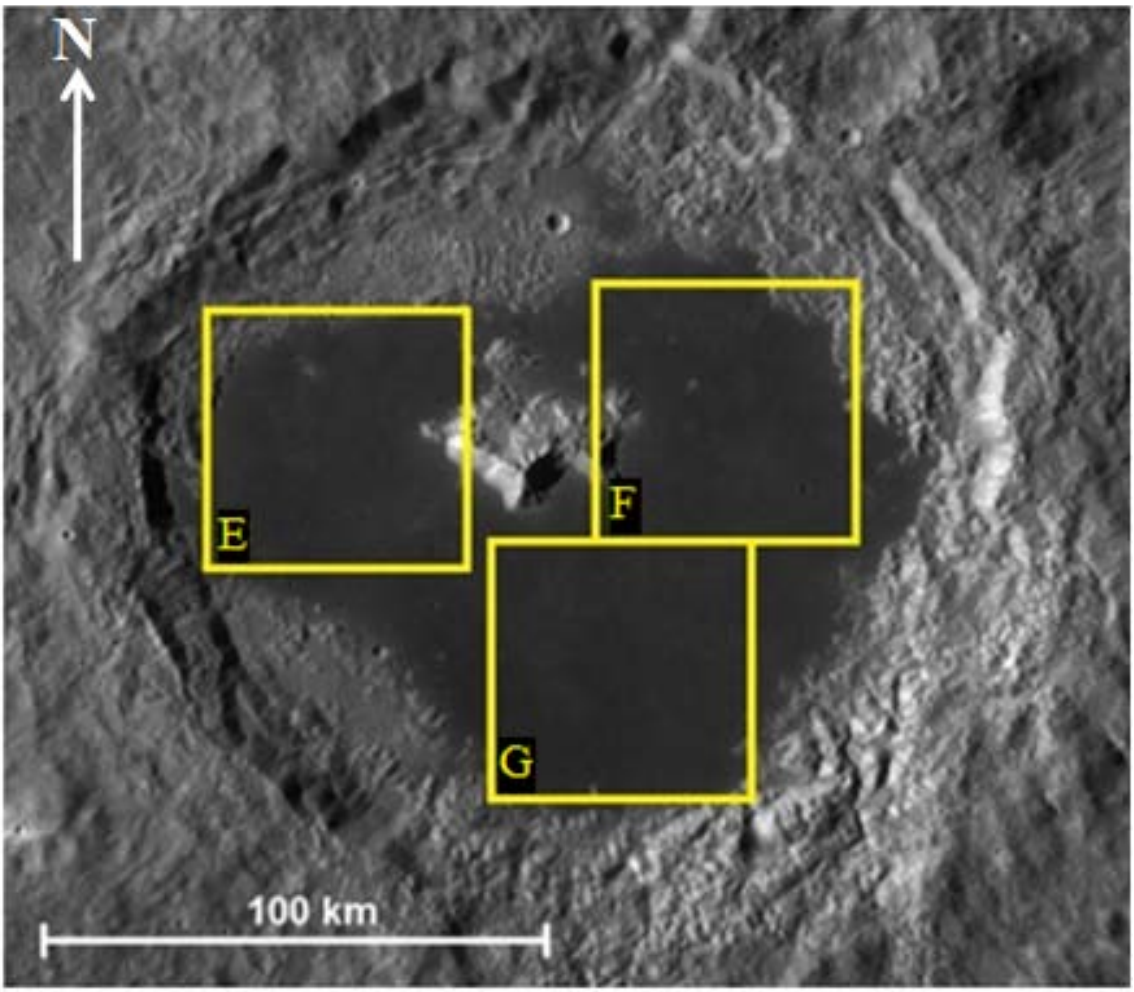

Figure 7.10: Test regions E, F, and G in crater Tsiolkovsky superposed on the LROC WAC mosaic image (Speyerer et al., 2011).

Three maps were plotted in Figure 7.11, representing the densities of detected craters before and after removal of secondary candidates. There are visible fluctuations of the crater density in the maps obtained without SCD algorithm. Applying the SCD algorithm reduces the crater density fluctuations especially for the binned version.

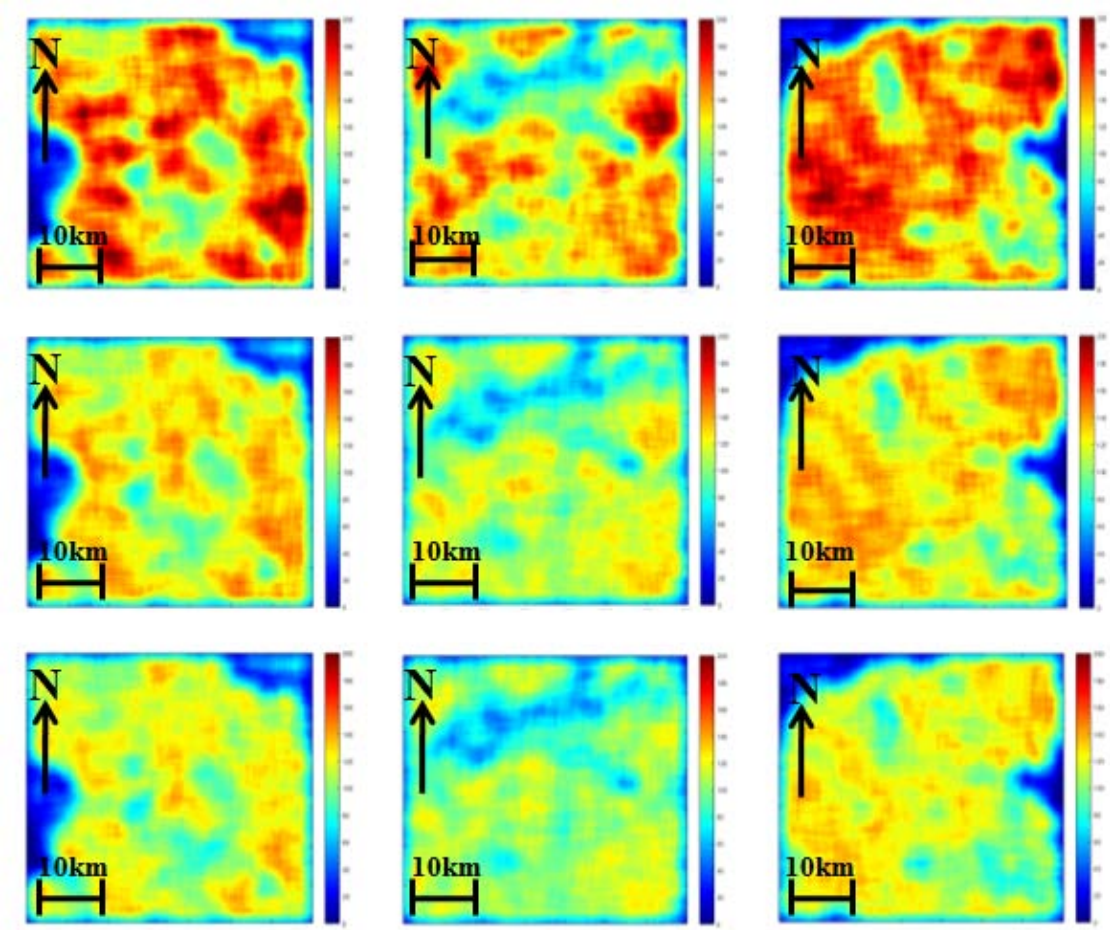

Figure 7.11: Effect of removal of secondary candidates on the crater densities of test regions E, F, and G. First row: Craters detected by template matching. Second row: Crater density after applying the SCD algorithm. Third row: Crater density after applying the binned SCD algorithm. From Salih et al. (2017a).

The estimated AMAs of the regions before removing secondary candidates range from 3.29 to 3.44 Ga without SCD and from 3.14 to 3.37 Ga with binned SCD (Table 7.3). Although the SCD algorithm has a relatively strong effect on the crater density, the unbinned SCD algorithm only has a weak effect on the AMA (around 0.2 Ga), while removing more than 10% of the craters.

Table 7.3: AMAs in Ga for test regions E, F, and G.

Method	E	F	G
template matching	**3.297 ± 0.002**	**3.446 ± 0.003**	**3.371 ± 0.001**
with SCD	**3.271 ± 0.002**	**3.435 ± 0.0004**	**3.353 ± 0.001**
with binned SCD	**3.149 ± 0.004**	**3.37 ± 0.0002**	**3.249 ± 0.001**

The SCD and binned SCD remove 12% and 18% percent of all craters, respectively (Table 7.4), but the binned SCD has a much stronger effect on the AMA (Table 7.3). The obtained age estimates are closer to the 3.21 Ga value than those obtained using plain template matching.

Table 7.4: Number of detected craters in test regions E, F, and G.

	E	F	G
craters detected without SCD	**17571**	**16292**	**17938**
with SCD	**15349 (87%)**	**14341 (88%)**	**15633 (87%)**
with binned SCD	**14441 (82%)**	**13430 (82%)**	**14651 (81%)**

7.8 Refine Age Map of the Floor of Tsiolkovsky

By using the template matching algorithm and the threshold value of 0.6568, the following age map was obtained for the floor of Tsiolkovsky as shown in Figure 7.12. A (900 by 900) pixel window was used for constructing all age maps with a step width of 10 pixels. The area surrounding crater Tsiolkovsky consists of rough highland surfaces that cannot be taken into account because the template matching threshold has been optimized for the flat basaltic lava surface of Tsiolkovsky's floor. Although the Tsiolkovsky floor region looks homogeneous, AMA anomalies are clearly visible in Figure 7.12, having estimated AMAs of up to 3.7 Ga. This value is significantly higher than the AMA estimated based on manually counted craters by Pasckert et al. (2015). These age fluctuations may occur because of clusters of secondary craters.

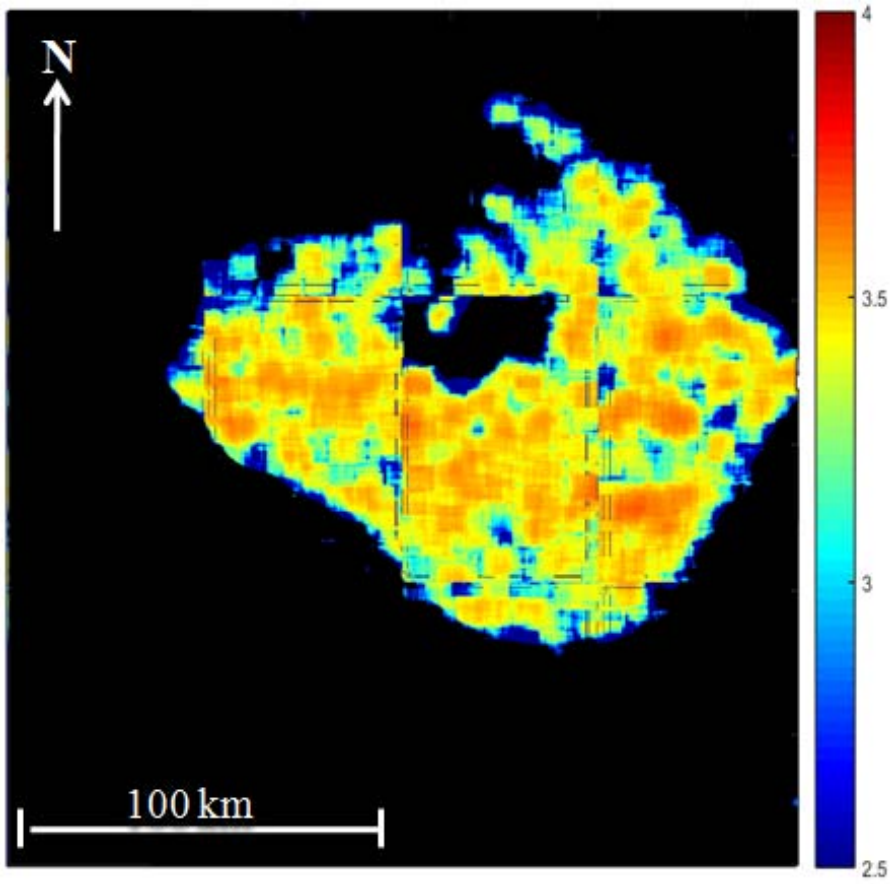

Figure 7.12: Age map of the floor of crater Tsiolkovsky using the CSFD obtained by the template matching method with an optimal threshold value, without the SCD algorithm. Black: No data

The template matching algorithm had been applied again to be combined with the SCD algorithm using a local threshold derived for each image patch and using a global threshold value as a mean of the threshold values of regions E, F, and G. The global threshold produced results that are more consistent. After applying the SCD algorithm, two new age maps as shown in Figure 7.13 and Figure 7.14 have been obtained. The first age map (Figure 7.13) slightly differs from the original age map of Figure 7.12. There is some reduction in age within high-age regions but the overall effect on the age map is almost invisible.

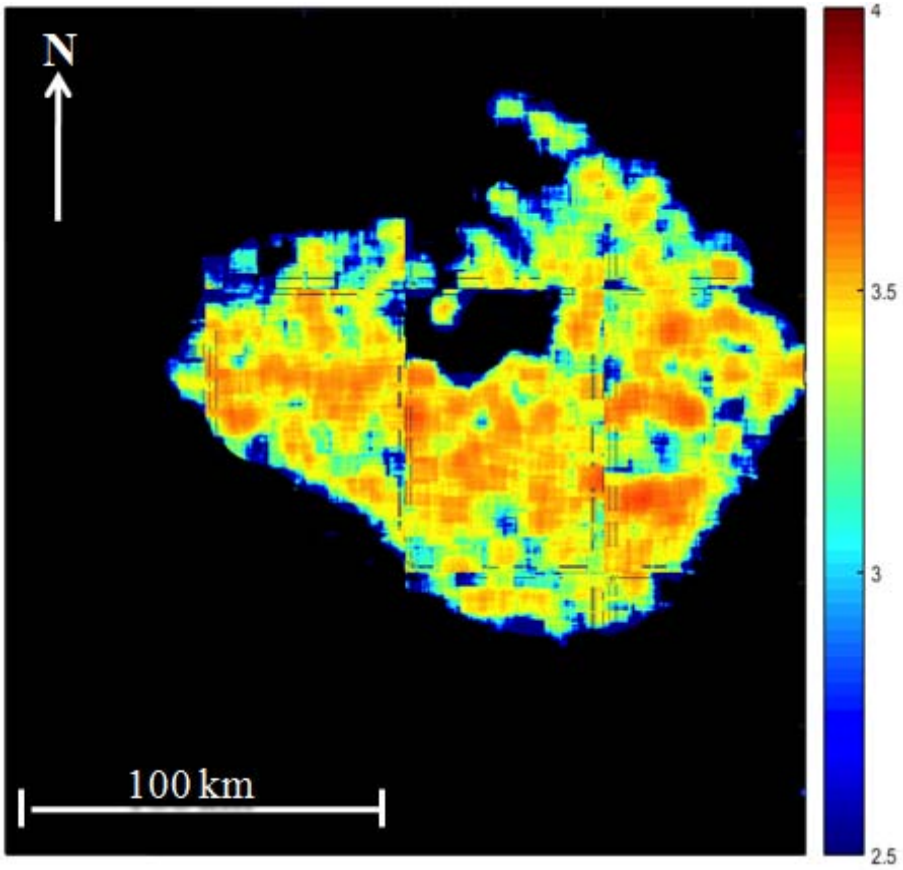

Figure 7.13: Age map of the floor of crater Tsiolkovsky using the CSFD obtained by the template matching method with an optimal threshold value in combination with the SCD algorithm without bins.

To construct the age map of Figure 7.14, the binned SCD algorithm has been applied based on the same detection threshold. In comparison to Figure 7.12, this map shows visible changes in the estimated AMA. Especially, the ages of the localized regions of high age in Figure 7.12 are reduced to the value of the surrounding surface, and the application of the binned SCD algorithm results in an age map that strongly reduces the fluctuations in the age of the geologically homogeneous surface of the floor of crater Tsiolkovsky. Indeed, the apparent morphological homogeneity of the floor of Tsiolkovsky points at a low probability of significant surface age variations on large spatial scales (small-scale age variations may occur, e.g., due to the burial of old small craters by the ejecta of fresh craters). The large positive AMA anomalies on the eastern floor of Tsiolkovsky obtained without applying the SCD algorithm (Figure 7.12) can thus be considered as being due to clusters of secondary craters, and the successful removal of these anomalies by the binned SCD algorithm (but not the unbinned SCD algorithm) indicates that the binned version of the algorithm yields plausible results. A more quantitative evaluation of the SCD algorithm is difficult because for this purpose a

classification of all craters according to their primary or secondary origin would be required.

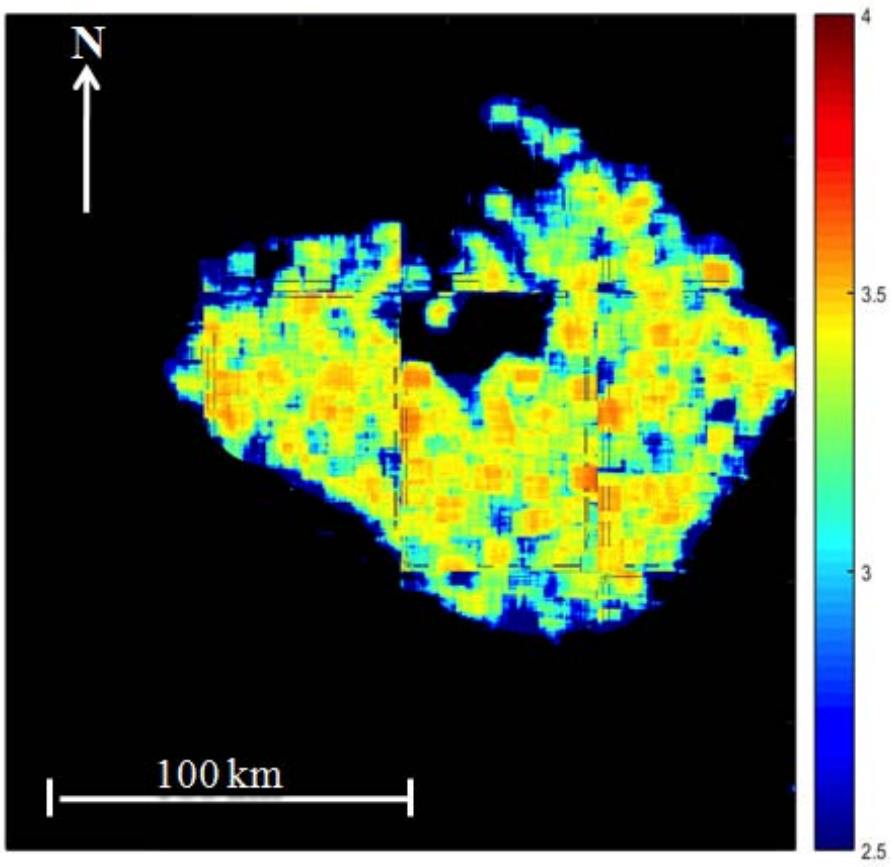

Figure 7.14: Age map of the floor of crater Tsiolkovsky using the CSFD obtained by the template matching method with an optimal threshold value in combination with the binned SCD algorithm.

7.9 Chapter Summary

In this chapter, an image template matching based CDA has been applied to a Kaguya spacecraft image of the mare-like floor of the lunar crater Tsiolkovsky. The AMA of the surface has been estimated based on the CSFD inferred from the detection results of the CDA. The obtained detection threshold was calibrated based on manual crater counts applied for a small sub-region of the crater floor. The average AMA of the crater floor is consistent with previous surface age estimates. Age maps in different stages have been created for calibration, evaluation, and comparison. The constructed SCD algorithm has been applied also to study and clarify the effect of secondary craters in relation to age estimates.

Chapter 8

Conclusions and Future Enhancement

8.1 Conclusions

An automatic template matching based CDA followed by the constructed automatic age estimation has been applied to study areas in Mare Cognitum on the Moon. The AMA has been computed for each of the ten study areas based on the obtained CDA-based CSFD. The calibrated CDA has then been applied to another five study areas in Oceanus Procellarum with well-known AMAs. All in all, the applied template matching method yields similar results between CDA-based AMAs and AMAs manually derived by Hiesinger et al. (2003) with minor deviations. In most areas, the difference was within the one standard deviation error interval. The CDA-based AMAs are especially reliable for surfaces older than 3.0 Ga or younger than 2.0 Ga, encouraging the application of CDAs as a valuable tool for planetary AMA estimation. In the range of 2-3 Ga, the error bars of the AMAs are large due to an almost flat chronology function in logarithmic-linear space. Thus, the researchers should be more in caution to be careful when using automatic CDAs on lunar surface areas with ages in this range.

A comparison of different crater detectors and their effect were studied and analyzed to the LU78287GT catalogue in the context of surface age determination. The obtained results show that the automatic crater detection may result in realistic results in the estimation of surface ages if the appropriate calibration procedure is applied.

The next step was to apply the created image-based template matching CDA to the high-resolution LRO NAC image M126961088LE showing the region around the small lunar crater Hell Q. The applied CDA has yielded a reliable CSFD based on the detected craters and their estimated diameters, and the AMA of the surface has been derived automatically. A calibration process based on reference manual crater counts for a sub-region of the total image was applied to obtain an appropriate detection threshold value. The resulting average AMA of the crater floor is consistent with the reference age obtained by manual CSFD measurements in Fisher (2014).

A construction of a spatially resolved map of the AMA has been obtained by applying the template-based CDA to overlapping sub-regions of the study area. The age map shows that the crater Hell Q is only 1-2 Ma old and thus clearly much younger than the neighboring surface. The estimated AMA increases continuously with increasing distance from Hell Q, which may be due to a gradual decrease in the thickness of its ejecta blanket. The described automatic age map construction technique allows for a comparison between surface parts or geological units in terms of their AMAs. It can be easily applied to any other surface areas once manual crater count data are available as a reference for a small sub-region.

The next step has been to apply the CDA to Kaguya TC image data of the mare-like floor of the lunar farside crater Tsiolkovsky. The detection threshold has been calibrated based on manual crater counts performed for a small sub-region of the crater floor. The average CDA-AMA of the crater floor is consistent with previous surface age estimates. Furthermore, a spatially resolved AMA map has been constructed by applying the CDA to overlapping sub-regions of the crater floor. Correlations between structures in the AMA map and local variations of spectral properties in Clementine UV/VIS color ratio data could be established. Two small local negative anomalies in the AMA map could be identified as steep-sloped highland-like remnants of the original crater floor penetrating the mare fill, while positive anomalies are probably due to the presence of clusters of secondary craters. Independent of these interpretations, the proposed surface age estimation, and mapping technique allow for a distinction between different geological units in terms of their AMAs. It can be applied in a straightforward manner to different surface regions, as long as manually determined AMA estimates are available for small sub-regions. To validate the results of this method in a more rigorous way, it should be tested on large mare areas on the lunar nearside whose surface ages are accurately known.

A disadvantage of the applied template matching method is that the illumination direction of the examined area needs to be known for each analyzed position in the image. If the regions do not show a uniform illumination, crater templates need to be generated for all occurring illumination conditions. This can be counteracted by (manually or automatically) detecting such variations and applying the CDA with the appropriate setting to each sub-region of homogeneous illumination.

In order to account for secondary craters that might affect the CSFD, the SCD algorithm for removing secondary crater candidates from the CSFD has been presented and applied to the floor region of crater Tsiolkovsky. This algorithm is based on the statistical analysis of the Voronoi diagram of the detected crater centers. In its binned version, the SCD algorithm results in an increased homogeneity of the constructed age map and eliminates local areas of significantly increased apparent ages, which are characterized by clusters of presumable secondary craters. The SCD method does not guarantee the detection of all secondary craters because secondary craters may also be distributed in a more or less uniform way (Bierhaus et al., 2001; McEwen and Bierhaus, 2006). This means that any algorithm that depends on the detection of unusual spatial crater distributions as a criterion for secondary craters will not be able to detect them completely. Because of the ambiguous nature of secondary craters, there is no definitive way to validate the actual origin of those craters. Due to the lack of reference data for the whole crater floor region, the algorithm could not be tested in a strictly quantitative and rigorous way. Nevertheless, the secondary crater fraction estimated with the binned SCD algorithm varies between (12 and 18%), and thus, is consistent with the estimated range between (5 and 25%) of Werner et al. (2009) for surfaces of similar age and craters of similar diameter on Mars.

Furthermore, the result of the binned SCD algorithm bears a high plausibility because it eliminates the spurious high-age anomalies in geologically homogeneous regions, which are apparent without secondary crater removal.

8.2 Future Improvement and Enhancement

As the first step of future work, it might be useful to increase the detection rate for more uncommon crater types by providing the CDA with a larger number of templates representing a larger variety of crater shapes, especially degraded craters.

The choice of a constant detection threshold for all crater sizes as suggested in the applied CDA work is the simplest possible one. Hence, since we found the sensitivity of the proposed CDA to be higher for larger than for smaller craters, an improvement of the detection results will be achieved by defining a diameter-dependent detection threshold can be expected for future extensions of the CDA.

All in all, however, it could be shown in this thesis that automatic crater detection allows, within the limits demonstrated, for a fully automated mapping of the surface age of large areas. An extension of the developed framework to further planetary bodies, such as Mars, Mercury, satellites of the giant planets, and Pluto appears favorable.

Bibliography

Allen, C. C. "Central peaks in lunar craters." The moon 12, no. 4: 463-474, (1975).

Arthur D. and Vassilvitskii S., "k-means++: The advantages of careful seeding." In Proceedings of the eighteenth annual ACM-SIAM symposium on Discrete Algorithms, pp. 1027-1035. Society for Industrial and Applied Mathematics, 2007.

Arvidson, R., Drozd, R., Guinness, E., Hohenberg, C., Morgan, C., Morrison, R., and Oberbeck, V., "Cosmic ray exposure ages of Apollo 17 samples and the age of Tycho." In Lunar and Planetary Science Conference Proceedings, vol. 7, pp. 2817-2832. 1976.

Aurenhammer, F., 'Voronoi Diagrams – A Survey of a Fundamental Geometric Data Structure'. ACM Computing Surveys 23(3), pp. 345-404. 1991.

Austin, D., 'Voronoi Diagrams and a Day at the Beach'. URL: http://www. ams. org/samplings/feature-column/fcarc-Voronoi. (2006).

Baldwin, R. B., "Lunar crater counts." The Astronomical Journal 69: 377, (1964).

Baldwin, R. B., "Relative and absolute ages of individual craters and the rate of infalls on the Moon in the post-Imbrium period." Icarus 61, no. 1: 63-91, (1985).

Bandeira, L., Saraiva, J. and Pina, P., "Impact crater recognition on Mars based on a probability volume created by template matching." IEEE Transactions on Geoscience and Remote Sensing 45, no. 12: 4008-4015, (2007).

Basilevsky, A. T., Neukum, G., Ivanov, B. A., Werner, S. K., van Gesselt, S., Head, J. W., Denk, T., Jaumann, R., Hoffmann, H., Hauber, E. and McCord, T., 'Morphology and geological structure of the western part of the Olympus Mons volcano on Mars from the analysis of the Mars Express HRSC imagery'. Solar System Research, 39(2), pp. 85-101, 2005.

Bierhaus, E. B., Chapman, C. R. and Merline, W. J., 'Secondary craters on Europa and implications for cratered surfaces'. Nature, 437(7062), pp. 1125-1127, 2005.

Bierhaus, E. B., Chapman, C. R., Merline, W. J., Brooks, S. M. and Asphaug, E., 'Pwyll secondaries and other small craters on Europa'. Icarus, 153(2), pp. 264-276, 2001.

Bishop, C. M., 'Pattern recognition and machine learning (information science and statistics)'. Springer-Verlag new york. Inc. Secaucus, NJ, USA, (2006).

Boukercha, A., Al-Tameemi, A., Grumpe, A., and Wöhler, C., "Automatic Crater Recognition Using Machine Learning with Different Features and Their Combination." In Lunar and Planetary Science Conference, vol. 45, p. 2842. 2014.

Bue, B. D., and Stepinski, T. F., "Machine detection of Martian impact craters from digital topography data." IEEE Transactions on Geoscience and Remote Sensing 45, no. 1: 265-274, (2007).

Chauhan, P., Kaur, P., Srivastava, N., Bhattacharya, S., Ajai, Kumar, A. K., and Goswami, J. N. "Compositional and morphological analysis of high resolution remote sensing data over central peak of Tycho crater on the Moon: implications for understanding lunar interior." Current Science: 1041-1046, (2012).

Cheng, Y., Johnson, A. E., Matthies, L. H. and Olson, C. F., "Optical landmark detection for spacecraft navigation." Advances in the Astronautical Sciences 114, no. 3: 1785-1803, (2003).

Chin, G., Brylow, S., Foote, M., Garvin, J., Kasper, J., Keller, J., Litvak, M., Mitrofanov, I., Paige, D., Raney, K. and Robinson, M., 'Lunar reconnaissance orbiter overview: Theáinstrument suite and mission'. Space Science Reviews, 129(4), pp.391-419, 2007.

Chire. 'Cluster analysis with k-means', URL https://commons.wikimedia.org/wiki/File: KMeansGaussiandata.svg;https://en.wikipedia.org/wiki/File:DBSCAN-Gaussian-data. svg;https://en.wikipedia.org/wiki/File:EM-Gaussian-data.svg;https://en.wikipedia.org /wiki/File:SLINK-Gaussian-data.svg. 2011.

Chiu, S. N., 'Spatial point pattern analysis by using Voronoi diagrams and Delaunay tessellations–a comparative study'. Biometrical Journal, 45(3), pp. 367-376, 2003.

Christoff, N., Manolova, A., Jorda, L., & Mari, J. L., 'Feature extraction and automatic detection of martian impact craters from 3D meshes'. In Advanced Technologies, Systems and Services in Telecommunications (TELSIKS), 2017 13th International Conference on (pp. 211-214). IEEE. 2017.

Chung, C. P., Chung, C. O., Yam, C. H., 'Lunar Crater Identification from Machine Learning Perspective'. Acta Futura 9, 41-47. 2014.

Cohen, J. P., Lo, H. Z., Lu, T. and Ding, W., 'Crater detection via convolutional neural networks'. arXiv preprint arXiv:1601.00978. 2016.

De Berg, M., Van Kreveld, M., Overmars, M. and Schwarzkopf, O.C., 'Computational geometry'. In Computational geometry (pp. 1-17). Springer, Berlin, Heidelberg. (2000).

Degirmenci, M. and Ashyralyyev, S., "Impact crater detection on mars digital elevation and image model." Middle East Technical University (2010).

Di Stadio, F., Costantini, M., and Di Martino, M., 'Craters-executive summary: Survey of algorithms for automatic recognition of impact craters'. Telespazio-EO Doc. No. 190.193-SPA-ES-001, (1.0). (2002).

Di, K., Li, W., Yue, Z., Sun, Y., and Liu, Y., 'A machine learning approach to crater detection from topographic data'. Advances in Space Research, 54(11), 2419-2429. (2014).

Ding, W., Stepinski, T.F., Mu, Y., Bandeira, L., Ricardo, R., Wu, Y., Lu, Z., Cao, T. and Wu, X., "Subkilometer crater discovery with boosting and transfer learning." ACM Transactions on Intelligent Systems and Technology (TIST) 2, no. 4: 39. (2011)

Dundas, C. M., and McEwen, A. S., 'Rays and secondary craters of Tycho'. Icarus, 186(1), 31-40. (2007).

Enzweiler, M. and Gavrila, D.M., "Monocular pedestrian detection: Survey and experiments." IEEE transactions on pattern analysis and machine intelligence 31, no. 12: 2179-2195. (2009).

Fisher, K. A. "An Age for Hell Q from Small Diameter Craters." In Lunar and Planetary Science Conference, vol. 45, p. 1421. 2014.

Galloway, M. J., Benedix, G. K., Bland, P. A., Paxman, J., Towner, M. C., and Tan, T. 'Automated crater detection and counting using the Hough transform'. In Image Processing (ICIP), 2014 IEEE International Conference on (pp. 1579-1583). IEEE. 2014.

Gonzalez, R. C., and Woods, R. E. 'Digital image processing'. 2012.

Grieve R. A. F., Cintala M. J. und Tagle R. 'Planetary impacts,' in: McFadden, A., Weissmann, P. R., Johnson, T. V. (eds.), Encyclopedia of the Solar System, 2nd ed., pp. 813-828, Academic Press, 2007.

Grigorescu, S.E., Petkov, N. and Kruizinga, P., "Comparison of texture features based on Gabor filters." IEEE Transactions on Image processing 11, no. 10: 1160-1167. (2002).

Grumpe, A., and Wöhler C., "Generative template-based approach to the automated detection of small craters." In European Planetary Science Congress, vol. 8. 2013.

Grumpe, A., Belkhir, F., and Wöhler, C., ‘Construction of lunar DEMs based on reflectance modelling’. Advances in Space Research, 53(12), 1735-1767, (2014).

Hapke, B., "Bidirectional reflectance spectroscopy: 5. The coherent backscatter opposition effect and anisotropic scattering." Icarus 157, no. 2: 523-534, (2002).

Hapke, B., ‘Bidirectional reflectance spectroscopy: 3. Correction for macroscopic roughness’. Icarus 59(1), 41-59. 1984.

Hapke, B., ‘Theory of reflectance and emittance spectroscopy’. Cambridge University Press, 2012.

Hart, P. E., ‘How the Hough Transform Was Invented’. IEEE Signal Processing Magazine 26(6), 18-22. 2009.

Hartmann, W. K. "On the distribution of lunar crater diameters." Communications of the Lunar and Planetary Laboratory 2: 197-204. (1964).

Hartmann, W. K. and Neukum, G., “Cratering chronology and the evolution of Mars”. In Chronology and evolution of Mars (pp. 165-194). Springer Netherlands. , 2001.

Hartmann, W. K., "Martian cratering, 4, Mariner 9 initial analysis of cratering chronology." Journal of Geophysical Research 78, no. 20: 4096-4116. (1973).

Hartmann, W. K., "Martian cratering." Icarus 5, no. 1-6: 565-576. (1966).

Hartmann, W. K., "Terrestrial and lunar flux of large meteorites in the last two billion years." Icarus 4, no. 2: 157-165. (1965).

Hartmann, W. K., ‘Martian cratering VI. Crater count isochrons and evidence for recent volcanism from Mars Global Surveyor’. Meteoritics and Planetary Science 34, 167-177. 1999.

Haruyama, J., Hara, S., Hioki, K., Iwasaki, A., Morota, T., Ohtake, M., Matsunaga, T., Araki, H., Matsu-moto, K., Ishihara, Y. and Noda, H., ‘March. Lunar global digital terrain model dataset produced from SELENE (Kaguya) terrain camera stereo observations’. In Lunar and Planetary Science Conference XXXXIII, abstract #1200. 2012.

Haruyama, J., Ohtake, M., Matsunaga, T., Otake, H., Ishihara, Y., Masuda, K., Yokota, Y., Yamamoto, S., 'Data products of SELENE (Kaguya) Terrain Camera for Future Lunar Missions'. LPSC XXXXV, abstract #1304. 2014.

Hiesinger, H., Head, J.W., Wolf, U., Jaumann, R. and Neukum, G., "Ages and stratigraphy of mare basalts in oceanus procellarum, mare nubium, mare cognitum, and mare insularum." Journal of Geophysical Research: Planets 108, no. E7 (2003).

Hiesinger, H., van der Bogert, C. H., Reiss, D. and Robinson, M.S., 'Crater size-frequency distribution measurements of Mare Crisium'. LPSC XXXXII, abstract #2179. 2011.

Honda, C., Kinoshita, T., Hirata, N. and Morota, T., 'Detection abilities of secondary craters based on the clustering analysis and Voronoi diagram'. In European Planetary Science Congress 2014, EPSC Abstracts, Vol. 9, id. EPSC2014-119 (Vol. 9). 2014.

Honda, R., Iijima, Y., and Konishi, O., 'Mining of topographic feature from heterogeneous imagery and its application to lunar craters'. In Progress in Discovery Science (pp. 395-407). Springer, Berlin, Heidelberg. (2002).

Hörz, F., Grieve, R., Heiken, G., Spudis, P. and Binder, A., "Lunar surface processes." Lunar Sourcebook: 61-120. (1991).

Hough, P. V., 'Method and means for recognizing complex patterns'. U.S. Patent 3,069,654, issued December 1962.

Ivanov, B.A., "Mars/Moon cratering rate ratio estimates." Space Science Reviews 96, no. 1: 87-104. (2001).

Kim, J.R. and Muller, J.P., "Impact crater detection on optical images and DEMs." (2003).

Kim, J.R., Muller, J.P., van Gasselt, S., Morley, J.G. and Neukum, G., "Automated crater detection, a new tool for Mars cartography and chronology." Photogrammetric Engineering and Remote Sensing 71, no. 10: 1205-1217. (2005).

Kneissl, T., van Gasselt, S. and Neukum, G., 'Map-projection-independent crater size-frequency determination in GIS environments—New software tool for ArcGIS'. Planetary and Space Science, 59(11), pp. 1243-1254. 2011.

König, B., Neukum, G. and Fechtig, H., "Recent lunar cratering: absolute ages of Kepler, Aristarchus, Tycho." In Lunar and Planetary Science Conference, vol. 8. 1977.

Leroy, B., Medioni, G., Johnson, E. and Matthies, L., "Crater detection for autonomous landing on asteroids." Image and Vision Computing 19, no. 11: 787-792. (2001).

Liu, S., Ding, W. and Stepinski, T.F., "Semi-supervised based active class selection for automatic identification of sub-kilometer craters." In Image and Signal Processing and Analysis (ISPA), 2011 7th International Symposium on, pp. 615-620. IEEE, 2011.

Liu, S., Ding, W., Gao, F. and Stepinski, T.F., "Adaptive Selective Learning for automatic identification of sub-kilometer craters." Neurocomputing 92: 78-87. (2012).

Lloyd, S., "Least squares quantization in PCM." IEEE transactions on information theory 28, no. 2: 129-137. (1982).

Lompart, A., 'Automatic detection of secondary craters in lunar orbital images'. Master Degree Thesis in Technical University of Dortmund, 2017.

LROC Observation M126961088L, http://wms.lroc.asu.edu/lroc/view_lroc/LRO-L-LROC-2-EDR-V1.0/M126961088LE. 2010.

MacQueen, J., 'Some methods for classification and analysis of multivariate observations'. In Proceedings of the fifth Berkeley symposium on mathematical statistics and probability (Vol. 1, No. 14, pp. 281-297). 1967.

Malin, M. C., Edgett, K. S., Posiolova, L. V., McColley, S. M., Noe Dobrea, E. Z., 'Present-Day Impact CrateringRate and Contemporary GullyActivity on Mars'. Science 314, 1573-1577. 2006.

Marchuk, A.G. and Simonov, K.V., "Detecting possible impact craters on the Earth's surface using the DEM data processing." Bull. Nov. Comp. Center, Math. Model in Geoph 10: 59-66. (2005).

Marsland, S., 'Machine learning: an algorithmic introduction'. (2009).

Maune, D. F. (Ed.), 'Digital elevation model technologies and applications: the DEM user's manual'. Asprs Publications. (2007).

McEwen, A. S., and Bierhaus, E. B., 'The importance of secondary cratering to age constraints on planetary surfaces'. Annu. Rev. Earth Planet. Sci., 34, pp. 535-567. 2006.

McEwen, A. S., Gaddis, L. R., Neukum, G., Hoffmann, H., Pieters, C. M. and Head III, J. W., "Lunar craters and soils: Ages, colors, and regolith thicknesses." In Lunar and Planetary Science Conference, vol. 23. 1992.

McEwen, A. S., Preblich, B. S., Turtle, E. P., Artemieva, N. A., Golombek, M. P., Hurst, M., Kirk, R. L., Burr, D. M. and Christensen, P. R., "The rayed crater Zunil and interpretations of small impact craters on Mars." Icarus 176, no. 2: 351-381. (2005).

McFadden, L. A., Johnson, T., and Weissman, P. eds., 'Encyclopedia of the solar system'. Academic Press, 2006.

Michael, G. G., "Planetary surface dating from crater size–frequency distribution measurements: Multiple resurfacing episodes and differential isochron fitting." Icarus 226, no. 1: 885-890. (2013).

Michael, G. G., 'Craterstats'. http://hrscview.fu-berlin.de/craterstats.html. Accessed: 2014/05/02. (2014).

Michael, G. G., and Neukum, G., "Planetary surface dating from crater size–frequency distribution measurements: Partial resurfacing events and statistical age uncertainty." Earth and Planetary Science Letters 294, no. 3: 223-229. (2010).

Michael, G. G., Personal communication. 2015.

Michael, G. G., Platz, T., Kneissl, T., and Schmedemann, N., "Planetary surface dating from crater size–frequency distribution measurements: Spatial randomness and clustering." Icarus 218, no. 1: 169-177. (2012).

Mühlbauer, M., 'Determination of Lunar Surface Ages using Automatic Crater Detection'. Bachelor Degree Thesis in Technical University of Dortmund, 2015.

Neukum, G. and König, B., "Dating of individual lunar craters." In Lunar and Planetary Science Conference Proceedings, vol. 7, pp. 2867-2881. 1976.

Neukum, G., 'Meteoritenbombardement und datierung planetarer oberflachen'. Habilitation Dissertation for Faculty Membership, Ludwig Maximilianis Univ.-Munich. 1983.

Neukum, G., and Wise, D. U., 'Mars- A standard crater curve and possible new time scale'. Science, 194(4272), 1381-1387. (1976).

Neukum, G., Ivanov, B. A. and Hartmann, W. K., "Cratering records in the inner solar system in relation to the lunar reference system." Space Science Reviews 96, no. 1-4: 55-86. (2001).

Nichols, D. J., Young, R. A., Brennan, W. J., 'Lunar kipukas as evidence for an extended tectonic and volcanic history of the maria'. Lunar and Planetary Science Conference V, pp. 550-552. 1974.

Ohtake, M., Haruyama, J., Matsunaga, T., Yokota, Y., Morota, T. and Honda, C., 'Performance and scientific objectives of the SELENE (KAGUYA) Multiband Imager'. Earth, planets and space, 60(4), pp. 257-264. 2008.

Oliva, A., and Torralba, A., 'Modeling the shape of the scene: A holistic representation of the spatial envelope'. International journal of computer vision 42, no. 3: 145-175. 2001.

Pasckert, J. H., Hiesinger, H., van der Bogert, C. H., 'Small-scale lunar farside volcanism'. Icarus 257, 336-354. 2015.

Pieters, C. M., Boardman, J., Buratti, B., Chatterjee, A., Clark, R., Glavich, T., Green, R., Head III, J., Isaacson, P., Malaret, E. and McCord, T., "The Moon Mineralogy Mapper (M^3) on Chandrayaan-1." Current Science: 500-505. (2009).

Pieters, C. M., Staid, M. I., Fischer, E. M., Tompkins, S. and He, G., 'A Sharper View of Impact Craters from Clementine Data'. Science 266, 1844-1848. 1994.

Pike, R. J., "Crater dimensions from Apollo data and supplemental sources." The Moon 15, no. 3-4: 463-477. (1976).

Ravikumar A. J, and Sreedharan D., "A Survey on Crater Detection Algorithms", BEST: International Journal of Humanities, Arts, Medicine and Sciences (BEST: IJHAMS) ISSN (P): 2348-0521, ISSN (E): 2454-4728 Vol. 4, Issue 1, Jan 2016, p. 107-112. 2016.

Ravine, M. A., and Grieve, R. A. F., "An analysis of morphologic variation in simple lunar craters." In Lunar and Planetary Science Conference Proceedings, vol. 17. 1986.

Robbins, S. J., 'Developing a global lunar crater database, complete for craters for craters≥1 km'. LPSC XXXXVII, abstract #1525. 2016.

Robbins, S. J., 'Mars Crater Catalog'. http://astrogeology. usgs.gov/search/map/Mars/Research/Craters/RobbinsCraterDatabase_20120821. 2009.

Robbins, S. J., and Hynek, B. M., ‘The secondary crater population of Mars’. Earth and Planetary Science Letters, 400, pp. 66-76. 2014.

Robbins, S. J., Antonenko, I., Kirchoff, M. R., Chapman, C.R., Fassett, C.I., Herrick, R.R., Singer, K., Zanetti, M., Lehan, C., Huang, D. and Gay, P.L., "The variability of crater identification among expert and community crater analysts." Icarus 234: 109-131. (2014).

Robinson, M. S., Brylow, S. M., Tschimmel, M., Humm, D., Lawrence, S. J., Thomas, P. C., Denevi, B. W., Bowman-Cisneros, E., Zerr, J., Ravine, M. A. and Caplinger, M. A., ‘Lunar reconnaissance orbiter camera (LROC) instrument overview’. Space science reviews, 150(1-4), pp.81-124. 2010.

Salamunićcar, G. and Lončarić, S., "Crater detection algorithms: a survey of the first decade of intensive research." In Horizons in Earth Science Research. Volume 8. Nova Science Publishers, 2012.

Salamunićcar, G. and Lončarić, S., "GT-57633 catalogue of Martian impact craters developed for evaluation of crater detection algorithms." Planetary and Space Science 56, no. 15: 1992-2008. (2008).

Salamunićcar, G. and Lončarić, S., "Method for crater detection from Martian digital topography data using gradient value/orientation, morphometry, vote analysis, slip tuning, and calibration." IEEE Transactions on Geoscience and Remote Sensing 48, no. 5: 2317-2329. (2010).

Salamunićcar, G., Lončarić, S., Grumpe, A., and Wöhler, C.,’ Hybrid method for crater detection based on topography reconstruction from optical images and the new LU78287GT catalogue of Lunar impact craters’. Advances in Space Research, 53(12), 1783-1797. (2014).

Salamunićcar, G., Lončarić, S., Pina, P., Bandeira, L. and Saraiva, J., "MA130301GT catalogue of Martian impact craters and advanced evaluation of crater detection algorithms using diverse topography and image datasets." Planetary and Space Science 59, no. 1: 111-131. (2011).

Salih, A. L., Boukercha, A., Grumpe, A., Wöhler, C. and Hiesinger, H., "Automatic Crater Detection and Implications for Surface Age Estimation." In European Planetary Science Congress 2014, EPSC Abstracts, Vol. 9, id. EPSC2014-602, vol. 9. 2014.

Salih, A. L., Grumpe, A., Wöhler, C. and Hiesinger, H., "Construction of an Age Map of the Region Around the Young Lunar Crater Hell Q." International Journal of Simulation Systems, Science, and Technology, 17(33), 2016b.

Salih, A. L., Lompart, A., Grumpe, A., Wöhler, C. and Hiesinger, H., "Automatic Detection Of Secondary Craters And Mapping Of Planetary Surface Age Based On Lunar Orbital Images." International Archives of the Photogrammetry, Remote Sensing and Spatial Information Sciences 42 (2017a).

Salih, A. L., Lompart, A., Schulte P., Mühlbauer, M., Grumpe, A., Wöhler, C. and Hiesinger, H., 'Automatic Mapping of Planetary Surface Age', Book chapter in "Planetary Remote Sensing and Mapping", a publication by Taylor & Francis/CRC Press in late 2018, ISPRS Book Series.

Salih, A. L., Mühlbauer, M., Grumpe, A., Pasckert, J.H., Wöhler, C. and Hiesinger, H., "Mapping of Planetary Surface Age Based on Crater Statistics Obtained by an Automatic Detection Algorithm." ISPRS International Archives of the Photogrammetry, Remote Sensing and Spatial Information Sciences: 479-486. (2016a).

Salih, A. L., Schulte, P., Grumpe, A., Wöhler, C. and Hiesinger, H., "Automatic crater detection and age estimation for mare regions on the lunar surface." In Signal Processing Conference (EUSIPCO), 2017 25th European, pp. 518-522. IEEE, (2017b).

Sawabe, Y., Matsunaga, T. and Rokugawa, S., "Automated detection and classification of lunar craters using multiple approaches." Advances in Space Research 37, no. 1: 21-27. (2006).

Schowengertdt, R. A. "Remote Sensing: Models and Methods for Image Processing", 3rd edition. Academic Press, 2007.

Schürmann, J., 'Pattern classification: a unified view of statistical and neural approaches'. New York: Wiley, 1996.

Scott, H.S., Tanaka, K.L., Greeley, R., and Guest, J.E., "Geologic maps of the western equatorial. eastern equatorial and polar regions of Mars, scale 1: 15,000,000." US Geol. Surv. Map, I-1802-A, B and C (1986).

Shang, C., Barnes, D., and Shen, Q., 'Facilitating efficient mars terrain image classification with fuzzy-rough feature selection'. International Journal of Hybrid Intelligent Systems, 8(1), 3-13. 2011.

Shoemaker, E. M. and Hackman, R. J., "Stratigraphic basis for a lunar time scale." In Symposium-International Astronomical Union, vol. 14, pp. 289-300. Cambridge University Press, 1962.

Shoemaker, E. M., ‘2. Preliminary analysis of the fine structure of the lunar surface in mare cognitum’. In International Astronomical Union Colloquium (Vol. 5, pp. 23-77). Cambridge University Press. 1965.

Shuang, L., and Pingyuan, C., ‘Landmark tracking based autonomous navigation schemes for landing spacecraft on asteroids’. Acta Astronautica, 62(6), 391-403. (2008).

Simard, P. Y., Steinkraus, D., Platt, J., ‘Best practices for convolutional neural networks applied to visual document analysis’. Proc. 12th International Conference on Document Analysis and Recognition. 2003.

Smith, D .E., Zuber, M. T., Neumann, G. A., Lemoine, F.G., Mazarico, E., Torrence, M.H., McGarry, J.F., Rowlands, D.D., Head, J.W., Duxbury, T.H. and Aharonson, O., "Initial observations from the lunar orbiter laser altimeter (LOLA)." Geophysical Research Letters 37, no. 18. (2010).

Soderblom, L. A., Condit, C. D., West, R. A., Herman, B.M. and Kreidler, T.J., "Martian planetwide crater distributions: Implications for geologic history and surface processes." Icarus 22, no. 3: 239-263. (1974).

Solomon, C. and Breckon, T., ‘Fundamentals of Digital Image Processing: A practical approach with examples in Matlab’. John Wiley & Sons, 2011.

Speyerer, E. J., Poviliatis, R. Z., Robinson, M. S., Thomas, P. C., Wagner, R. V., ‘Quantifying crater production and regolith overturnon the Moon with temporal imaging’. Nature 538, 215-218. 2016.

Speyerer, E. J., Robinson, M. S. and Denevi, B. W., ‘Lunar Reconnaissance Orbiter camera global morphological map of the Moon’. In Lunar and Planetary Science Conference, vol. 42, p. 2387. 2011.

Stepinski, T. F., Ding, W., and Vilalta, R. "Detecting impact craters in planetary images using machine learning." Intelligent Data Analysis for Real-Life Applications: Theory and Practice. IGI Global, Hershey, PA: 146-159. (2012).

Stepinski, T. F., Mendenhall, M. P., and Bue, B. D., "Machine cataloging of impact craters on Mars." Icarus 203, no. 1: 77-87. (2009).

Stopar, J. D., Hawke, B. R., Robinson, M. S., Denevi, B. W., Giguere, T. A., and Koeber, S. D., "Occurrence and mechanisms of impact melt emplacement at small lunar craters." Icarus 243: 337-357. (2014).

Tanaka, K. L., "The stratigraphy of Mars." Journal of Geophysical Research: Solid Earth 91, no. B13. (1986).

Taud, H., and Parrot, J. F., "Detection of circular structures on satellite images." International Journal of Remote Sensing 13, no. 2: 319-335. (1992).

Theodoridis, S., and Koutroumbas, K., "Pattern recognition–Fourth edition". 2009.

Troglio, G., Benediktsson, J. A., Moser, G., and Serpico, S. B. 'Crater detection based on marked point processes'. In Geoscience and Remote Sensing Symposium (IGARSS), 2010 IEEE International (pp. 1378-1381). IEEE. 2010.

Tyrie, A., 'A description of the crater Tsiolkovsky on the lunar far side. Earth, Moon, and Planets', 42, 265-275. 1988a.

Tyrie, A., 'Age dating of mare in the lunar crater Tsiolkovsky by crater-counting method. Earth, Moon, and Planets' 42, 245-264. 1988b.

Urbach, E. R., and Stepinski, T. F., "Automatic detection of sub-km craters in high resolution planetary images." Planetary and Space Science 57, no. 7: 880-887. (2009).

Van der Bogert, C. H., Michael, G., Kneissl, T., Hiesinger, H., & Pasckert, J. H., 'Development of Guidelines for Recommended Lunar CSFD Count Area Sizes via Analysis of Random CSFDs'. Proc. Workshop on Issues in Crater Studies and the Dating of Planetary Surfaces, LPI Contributions 1841, abstract #9023. 2015.

Venkatasubramanian, S., 'Voronoi diagrams'. URL http://www.cs.utah.edu/~suresh/compgeom/voronoi.pdf. 2013.

Vijayan, S., Vani, K., & Sanjeevi, S., 'Topographical analysis of lunar impact craters using SELENE images'. Advances in Space Research, 52(7), 1221-1236. 2013.

Vijayan, S., Vani, K., and Sanjeev, S., "Crater detection, classification and contextual information extraction in lunar images using a novel algorithm." Icarus 226, no. 1: 798-815. (2013).

Vinogradova, T., Burl, M. and Mjolsness, E., "Training of a crater detection algorithm for Mars crater imagery." In Aerospace Conference Proceedings, 2002. IEEE, vol. 7, pp. 7-3201. IEEE, 2002.

Wagner, R. V., Speyerer, E. J., Robinson, M. S., and LROC Team., 'New Mosaicked Data Products from the LROC Team'. In Lunar and Planetary Science Conference (Vol. 46, p. 1473). 2015.

Walker, A. S., and El-Baz, F., 'Analysis of Crater Distributions in Mare Units on the Lunar Far Side'. The Moon and the Planets 27, 91-106. 1982.

Werner, S. C., Ivanov, B. A. and Neukum, G., 'Theoretical analysis of secondary cratering on Mars and an image-based study on the Cerberus Plains'. Icarus, 200(2), pp. 406-417. 2009.

Wetzler, P. G., Honda, R., Enke, B., Merline, W. J., Chapman, C. R., Burl, M. C., 'Learning to detect small impact craters'. Proc. Seventh IEEE Workshops on Application of Computer Vision, vol. 1, pp. 178-184. 2005.

Wong, K. W., Kwok, B. S. H., and Law, W. S., "A fast image encryption scheme based on chaotic standard map." Physics Letters A 372, no. 15: 2645-2652. (2008).

Yin, J., Xu, Y., Li, H. and Liu, Y., "A novel method of crater detection on digital elevation models." In 2013 IEEE International Geoscience and Remote Sensing Symposium-IGARSS, pp. 2509-2512. IEEE, 2013.

List of Figures

List of Tables

List of Abbreviations

AMA	:	Absolute model age
CDA	:	Crater detection algorithms
CSFD	:	Crater frequency size distribution
SCD	:	Secondary Candidate Detection
EM	:	Expectation–maximization
SLINK	:	Single-Linkage
DBSCAN	:	Density-based spatial clustering of applications with noise
MOC	:	Mars Orbiter Camera
MOLA	:	Mars Orbiter Laser Altimeter
HRSC	:	High-Resolution Stereo Camera
N_{cum}	:	Cumulative crater frequency
M	:	The number of rows in the Image
N	:	The number of columns in the Image